Investigating the Relationship between Structure and Magnetic Ground States of 5d Double Perovskites

Dissertation

Presented in Partial Fulfillment of the Requirements for the Degree Doctor of Philosophy

in the Graduate School of The Ohio State University

By

Phuong Minh Tran

Graduate Program in Chemistry

The Ohio State University

2020

Dissertation Committee

Dr. Patrick M. Woodward, Advisor

Dr. Joshua Goldberger

Dr. Sherwin Singer

Dr. Christopher Grimsley

Copyrighted by

Phuong Minh Tran

2020

Abstract

The focus of this dissertation is to investigate the relationship between structure and magnetic properties of 5d double perovskites and double perovskite derivative structures through different chemical substitution. Because of high spin-orbit coupling, high interorbital repulsion, and the extended nature of the 5d orbitals, how the spin, orbital, and lattice degree of freedom couple in order to stabilize the magnetic ground state is not well understood. The aim of this dissertation is to perturb the crystal lattice with chemical pressure or charge defects and determine the sensitivity of the magnetic properties to these changes.

Chapter 2 discusses the effect of distortions of the magnetic cation environment on the magnetic ground state of $5d^1$ double perovskites Sr_2ZnReO_6, Sr_2LiOsO_6, and Sr_2NaOsO_6. Crystallography analysis from synchrotron X-ray diffraction data shows that the Sr_2ZnReO_6 and Sr_2NaOsO_6 both crystallized in the monoclinic $P2_1/n$ space group where the Os–O bonds are different in all three crystallographic direction. Meanwhile, the Sr_2LiOsO_6 is tetragonal $I4/m$ with elongated Os–O bonds along the c crystallographic direction, even though the perovskite tolerance factor for the Sr_2ZnReO_6 is similar to the Sr_2LiOsO_6. Differences in structure results in different magnetic ground states. While the two monoclinic compounds are ferromagnetic similar to the cubic analogs, the tetragonal

compound is antiferromagnetic. This indicates that the magnetic ground state is highly sensitive to the bonding environment of the $5d^1$ cation.

Chapter 3 discusses the effect of charge doping on the $5d^1$ magnetic ground state in the solid solution system $Ba_2Na_xCa_{1-x}OsO_6$. The Ba_2NaOsO_6 compound has the cubic $Fm\bar{3}m$ structure and a ferromagnetic ground state. The Ba_2CaOsO_6 compound has the cubic $Fm\bar{3}m$ structure and an antiferromagnetic ground state. Crystallography analysis from powder X-ray diffraction shows that all the samples in the $Ba_2Na_xCa_{1-x}OsO_6$ series are also cubic $Fm\bar{3}m$. Magnetometry shows an increase in the magnetic transition temperature with increasing Ca^{2+} substitution. Interestingly, the ferromagnetic ground state is destabilized by a small ~12.5 % Ca^{2+} substitution.

Chapter 4 is the exploration of the $Ba_2Sr_{2-x}NiOsO_6$ in order to investigate the unusual magnetic ground states observed in double perovskites containing Ni^{2+} and Os^{6+}. The 180° superexchange between Ni^{2+} and Os^{6+} is ferromagnetic, however, the previously reported cubic Ba_2NiOsO_6 has a modulated antiferromagnetic structure.[1] From variable temperature X-ray and neutron diffraction, the $Ba_2Sr_{2-x}NiOsO_6$ phase space consists of four structural regions: $I4/m$, $Fm\bar{3}m$, mixed phase $Fm\bar{3}m$ and $P\bar{3}m1$, and $P\bar{3}m1$. The $I4/m$ and $Fm\bar{3}m$ regions have a magnetic transition at 40 K. All regions containing the $P\bar{3}m1$ phase have a ferromagnetic-like transition at 100 K. While variable neutron diffraction on $Ba_{1.2}Sr_{0.8}NiOsO_6$ shows that the structure is cubic $Fm\bar{3}m$ like the high pressure Ba_2NiOsO_6 compound from literature,[1] specific heat measurement on $Ba_{1.2}Sr_{0.8}NiOsO_6$ shows that the ground state is spin glass as opposed to the modulated antiferromagnetic structure of high pressure Ba_2NiOsO_6. Meanwhile, variable neutron diffraction on Ba_2NiOsO_6 shows that

the magnetic transition at 100 K is a ferrimagnetic, which suggests Ni^{2+} and Os^{6+} follows Goodenough-Kanamori rules in the absence of long range Ni–O–Os–O–Ni and Os–O–Ni–O–Os interactions.

Dedication

To my wonderful parents, Vịnh Trần and Vang Vũ. Cảm ơn bố mẹ. Con vượt qua nhiều khó khăn bởi vì con có sự hỗ trợ của bố mẹ.

Acknowledgments

Every single day in graduate school has been an adventure, and I was very lucky to be able to learn something new every day from my work and from the wonderful people around me. I want to thank everyone who has been a part of my Ph.D. journey.

First, I want to thank my advisor, Dr. Patrick Woodward, for his guidance and support in my professional development. I started graduate school knowing nothing about magnetism or crystallography, and I was very fortunate to learn much so more about these topics from his teaching and advice. I am also grateful for the amazing opportunities to travel to conferences to present my work and to national facilities to collect data.

Second, I want to thank everyone in the Woodward research lab. I would like to thank Ryan Morrow, Spencer Porter, Andrew Sharits, Matt Linaburg, Drew Adkins, and David Merz for passing on their knowledge and instrument training when I first joined the group. I would also like to thank Jie Xiong and Eric McClure, who had the most overlap with my time in graduate school, for their support and patience with my numerous questions. I would like to thank Matt Gray, Jackson Mahjer, Noah Holzapfel, and Victor da Cruz Pinha Barbosa for their help in both research and in making sure the office environment is never boring.

Third, I want to thank the wonderful collaborators and staff scientists that I had the pleasure of working with. I would like to thank all the professor in IRG-1 of the Center for Emergent Materials, Dr. Nandini Trivedi, Dr. David McComb, Dr. Mohit Randeria, Dr.

Wolfgang Windl, Dr. Fengyuan Yang, Dr. Rolando Valdes Aguilar, and Dr. Jiaqiang Yan, for their direct and indirect collaborations with some of my projects. I want to give special thanks to Wenjuan Zhang, who arrived into the $5d^1$ effort at the same time with me, for her beautiful calculations and enthusiasm in the project. I would also like to thank Dr. John Evans for the variable temperature X-ray data and more importantly, for the fantastic Topas Academic tutorials that revitalized my will to work through magnetic refinements. I was fortunate to be able to have support from talented staff scientists at many fantastic national laboratory facilities. I would like to thank Pamela Whitfield, Melanie Kirkham, and Qiang Zhang at the POWGEN beamline at Oak Ridge National Laboratory. I would also like to thank Ivan da Silva at the GEM instrument at the ISIS neutron source in the UK. In addition, I would also like to thank Saul Lapidus at the 11-BM beamline at Argonne National Laboratory, as well as Graham King at the Canadian Light Source for the synchrotron data collection. For the ongoing $Ba_2Na_xCa_{1-x}OsO_6$ work, I would like to thank Samuele Sanna, Vesna Mitrovic, Arumugam Sonachalam, Erick Garcia, and Rong Cong.

Fourth, I want to thank my committee members, Dr. Josh Goldberger and Dr. Sherwin Singer. I have had the great pleasure of learning from your classes, teaching for your class, and having your support in both candidacy and this defense.

Finally, I want to thank my family and friends for being a pillar of strength all these years. I would like to thank my parents, Vinh Tran and Vang Vu, for their love, encouragement, and great sense of humor through all the challenging times. I would also like to thank my two brothers, Ninh Tran and Khang Tran, as well as their wonderful families. You all inspired me to be the best person I can be.

Vita

2010–2014.....B.S. Chemistry, University of California, Berkeley

2014–present.....Graduate Research and Teaching Associate, Department of Chemistry and Biochemistry, The Ohio State University

Field of Study

Major Field: Chemistry

Table of Contents

Abstract ii

Dedication v

Acknowledgments vi

Vita viii

Table of Contents ix

List of Tables xii

List of Figures xiv

Chapter 1 Introduction 1

1.1 The Unique Magnetism of 5d Materials 1

1.2 Perovskite Structure 2

1.3 Double Perovskite Structure with 1:1 ordering 3

1.4 Tolerance Factor and Octahedral Tilting 4

1.5 Hexagonal Perovskite Derivatives 7

1.6 Types of Magnetic Ground States 8

1.7 Superexchange 13

1.8 180° Cation-Anion-Cation interactions 13

1.9 90° Cation-Anion-Cation interactions 15

1.10 Magnetic ordering in simple perovskites 17

1.11 Magnetic ordering in double perovskites 18

Chapter 2 The Effect of Structural Distortion on the $5d^1$ Magnetic Ground State 21

2.1 Introduction 21

2.2 Experimental 23
2.3 Results 25
2.3.1 Structural analysis 25
2.3.2 Investigating the magnetic properties 41
2.4 Discussion 48
2.5 Conclusion 51
Chapter 3 Structure and Magnetic Properties of Solid Solution $Ba_2Na_xCa_{1-x}OsO_6$ 53
3.1 Introduction 53
3.2 Experimental 54
3.3 Results 55
3.3.1 The structure of the $Ba_2Na_xCa_{1-x}OsO_6$ solid solution 55
3.3.2 Magnetic susceptibility measurements on the $Ba_2Na_xCa_{1-x}OsO_6$ solid solution 61
3.4 Discussion 70
3.5 Conclusion 72
Chapter 4 Structural and Magnetic Phase Diagram of $Ba_xSr_{2-x}NiOsO_6$ 73
4.1 Introduction 73
4.2 Experimental 75
4.3 Results 77
4.3.1 Structural studies on $Ba_xSr_{2-x}NiOsO_6$ 77
4.3.2 DC and AC magnetic susceptibility 94
4.3.3 Neutron diffraction 99
4.4 Discussion 106

4.5 Conclusion 109

Appendix A 115

Supplementary Information for *Structure and Magnetic Properties of Solid Solution* $Ba_2Na_xCa_{1-x}OsO_6$ 115

List of Tables

Page

Table 1.1: Double perovskites tilt systems and space groups.[20] 6

Table 2.1: Structural information for Sr_2ZnReO_6. For the *I*4/*m* structure, the Zn^{2+} ions occupy the special position 2a (0 0 0) and Re^{6+} ions occupy the special position 2b (1/2 1/2 0). For the $P2_1/n$ structure, the Zn^{2+} occupy the special position 2c (0 1/2 0) and Re^{2+} occupy the special position 2d (1/2 0 0). Starting point for atomic positions were generated from SPuDS. 32

Table 2.2: Structural information for Sr_2LiOsO_6. For the *I*4/*m* structure, the Li^+ occupy the special position 2a (0 0 0) and Os^{7+} occupy the special position 2b (1/2 1/2 0). The Sr^{2+} occupy the 4d (0, 1/2, 1/4) position. Starting point for atomic positions were generated from SPuDS. Distances are in angstrom, and volume is in cubic angstrom. ... 36

Table 2.3: Structural information for Sr_2NaOsO_6 at room temperature taken from the refinement of room temperature laboratory X-ray diffraction data. For the $P2_1/n$ structure, the Na^+ occupy the special position 2c (0 1/2 0) and Os^{7+} occupy the special position 2d (1/2 0 0). 40

Table 2.4: Calculated tolerance factor of Sr_2ZnReO_6, Sr_2LiOsO_6, and Sr_2NaOsO_6. 48

Table 2.5: List of $5d^1$ double perovskites. 51

Table 3.1: Phase composition of the $Ba_2Na_xCa_{1-x}OsO_6$ system from PXRD analysis. 57

Table 3.2: Magnetic transition temperatures for the x = 0–1 samples. 66

Table 3.3: Effective moments and Weiss constants from Curie-Weiss fit on zero-field cooled data with and without a temperature independent correction. 68

Table 4.1: Structural information for I/4m samples (x = 0.2–0.6) taken from refinement of the laboratory X-ray data. The Ba/Sr occupy the 4d (0 0 1/4) site. The Ni occupy the 2a

(0 0 0) site, and the Os occupy the (0 0 1/2) site. B_{iso} was fixed to the same value for Ni and Os. 85

Table 4.2: Structural information for *Fm*3*m* structures (x = 0.8–1.4) taken from refinement of the laboratory X-ray data. The Ba/Sr occupy the 8c (1/4 1/4 1/4) site. The Ni occupy the 2a (1/2 1/2 1/2) site, and the Os occupy the 4a (0 0 0) site. Phase percent is by weight. B_{iso} was fixed to the same value for Ni and Os..... 86

Table 4.3: Structural information for *P*3*m*1 structures (x = 1.4–2.0) taken from refinement of the laboratory X-ray data. The Ba/Sr occupy the 2c and 2d Wyckoff site. The Ni occupy the 1a and 2d site. The Os occupy the 1b and 2d site. 87

Table 4.4: Tetragonal to cubic phase transition temperatures taken from variable temperature PXRD data used for the linear fit..... 90

Table 4.5: Selected structural information for the $Ba_xSr_{2-x}NiOsO_6$ series. The ∠Ni–O–Os bond angles are for the corner-connected ∠Ni–O–Os bonds. Data for x = 1.2 and 2.0 were taken from neutron diffraction data which has more precise oxygen positions. 94

Table 4.6: Weiss temperature and effective moment extracted from linear Curie-Weiss fit from 150 K to 400 K for the $Ba_xSr_{2-x}NiOsO_6$ series. Weiss constant and effective moment from linear Curie-Weiss fitting of the inverse susceptibility data from 150 K to 400 K. Some of the mixed phase samples have an amount of NiO impurity so the phase percent listed here do not add up to 100 %..... 96

List of Figures

Page

Figure 1.1: 5d transition metals have higher spin-orbit coupling than 4d and 3d transition metals. Octahedral crystal field splits the degenerate d orbitals into the e_g and t_{2g}. Spin-orbital coupling further splits the t_2g into j = 1/2 and j = 3/2 states..... 2

Figure 1.2: Simple cubic perovskite structure with the chemical formula ABO_3. 3

Figure 1.3: Double perovskite structure with the chemical formula $A_2BB'O_6$..... 4

Figure 1.4: a) Tetragonal $I4/m$ double perovskite, b) monoclinic $P2_1/n$ double perovskite. 7

Figure 1.5: Different types of hexagonal perovskite derivatives. The number indicate number of layers, and the letter indicates the type of unit cell (hexagonal or rhombohedral). Figures made from cif files of reference 23–25. 8

Figure 1.6: Antiferromagnetic, ferromagnetic, and ferrimagnetic ground states and their features in the magnetic measurements. 12

Figure 1.7: For 180° superexchange mediated by a diamagnetic anion (gray), antiferromagnetic coupling occurs between a) empty e_g orbitals or b) half-filled e_g orbitals, while ferromagnetic coupling occurs between c) half-filled e_g and empty e_g orbitals. The black spins are the intrinsic spin of the electron that occupies the orbital, and red dashed spins are virtual electron transfers. Figures made from Wolfram Alpha orbital viewer plug in for Mathematica. 14

Figure 1.8: 90° superexchange through anion p orbitals (gray) between a) empty e_g orbitals, b) half-filled e_g orbitals, c) half-filled e_g orbitals and empty e_g orbitals. The black spins are the intrinsic spin of the electron that occupies the orbital, and red dashed spins are virtual electron transfers. Figures made from Wolfram Alpha orbital viewer plug in for Mathematica. 16

Figure 1.9: Different type of antiferromagnetic ordering for the simple perovskite structure. The magnetic moments are arranged on the crystallographic unit cell to highlight the spin arrangements. This is not representative of the magnetic unit cell. 18

Figure 1.10: a) Frustrated spins arranged on a triangular lattice, b) face center cubic lattice of magnetic cations is a frustrated system due to the tetrahedron arrangement magnetic moments. 19

Figure 1.11: Different type of magnetic ordering for double perovskites with one magnetic cation. 20

Figure 2.1: Different orbital occupation results in different magnetic ground states in isoelectronic Ba_2ZnReO_6 and Ba_2CdReO_6. 22

Figure 2.2: The barium site can be substituted with the smaller strontium, which causes octahedral tilting to compensate for its smaller size in the cavity. 23

Figure 2.3: Room temperature laboratory diffraction data for Sr_2ZnReO_6. 28

Figure 2.4: SXRD of Sr_2ZnReO_6 at a) 295 K and b) 90 K. 29

Figure 2.5: The Sr_2ZnReO_6 pattern at 295 K was fitted to one tetragonal phase (bottom, green) and two tetragonal phases (top, blue). The green tickmarks indicate the reflections allowed for one tetragonal phase. The blue and purple tickmarks indicate the reflections for two tetragonal phases. The dotted line represents the highest point of the reflection. 30

Figure 2.6: Differences in the peak splitting between the *I*4/*m* space group (295 K) and the $P2_1/n$ space group (90 K). The *I*4/*m* model fits the 295 K data well without the need to add a secondary monoclinic phase. Small asymmetry in some reflections such as the (0 0 4) and (2 0 4) were observed but the *I*4/*m* model still fits well. 31

Figure 2.7: a) Room temperature PXRD data of Sr_2LiOsO_6 fitted to the tetragonal *I*4/*m* space group, b) SXRD of Sr_2LiOsO_6 fitted to the tetragonal *I*4/*m* space group. 35

Figure 2.8: Room temperature PXRD of Sr_2NaOsO_6. 39

Figure 2.9: a) The magnetic susceptibility as a function of temperature for Sr_2ZnReO_6 at 1000 Oe, b) the inverse susceptibility, and c) isothermal magnetization at 2 K..... 44

Figure 2.10: a) The magnetic susceptibility as a function of temperature for Sr_2LiOsO_6 at 1000 Oe, b) the inverse susceptibility, and c) isothermal magnetization at 2 K..... 45

Figure 2.11: a) The magnetic susceptibility as a function of temperature for Sr_2NaOsO_6 at 1000 Oe, b) the inverse susceptibility, and c) isothermal magnetization at 2 K..... 46

Figure 2.12: Inverse magnetic susceptibility as a function of temperature with correction for the core electron (left) and with temperature independent correction (right). 47

Figure 3.1: Substituting the Na^+ site with Ca^{2+} to form the composition $Ba_2Na_xCa_{1-x}OsO_6$. 54

Figure 3.2: Cubic lattice parameter versus concentration of Ca^{2+} (bottom axis) and concentration of Na^+ (top axis). 58

Figure 3.3: Room temperature PXRD of the $Ba_2Na_xCa_{1-x}OsO_6$ solid solution. 59

Figure 3.4: Zoom-in region of the PXRD patterns for $Ba_2Na_xCa_{1-x}OsO_6$. 60

Figure 3.5: Magnetic susceptibility as a function of temperature for x = 0–1 samples. The switch from ferromagnetic to antiferromagnetic ground state occurs between x = 1 and x = 0.875. There is a ferromagnetic impurity in the x = 0–0.25 samples which makes the antiferromagnetic cusp difficult to observe. 64

Figure 3.6: Magnetization versus field for the x = 0–1 samples at 2 K. The transition at 45 K for the x = 0 sample is antiferromagnetic as confirmed by the linear magnetization versus field curve at 25 K. The presence of the ferromagnetic impurity is observed in the x = 0–0.25 samples. 65

Figure 3.7: Inverse magnetic susceptibility as a function of temperature for the x = 0–1 samples with the diamagnetic correction for the core electrons. 67

Figure 3.8: a) Effective moment as a function of Ca^{2+}concentration, b) Weiss constant as a function of Ca^{2+}concentration. 69

Figure 4.1: Different magnetic ground states of the nickel osmate double perovskites adapted from references [1,50,51]. The magnetic unit cell of high pressure Ba_2NiOsO_6 is cut in half to better visualize the spin arrangement. 74

Figure 4.2: The three main phases in the $Ba_xSr_{2-x}NiOsO_6$ series a) *I*4/*m*, b) *Fm*3*m*, and *P*3*m*1. 78

Figure 4.3: Powder neutron diffraction pattern at 300 K of the x = 0.6 sample which appears metrically cubic with laboratory X-ray diffraction. Rietveld refinements show that the *I*4/*m* structural model gives a better fit than the *Fm*3*m* and *I*4/*m* model. 80

Figure 4.4: The x = 2.0 sample was fitted with the *P*3*m*1, $P6_3mc$, and $P6_3/mmc$ space group. 82

Figure 4.5: The room temperature PXRD patterns of x = 0.2–1.2. 83

Figure 4.6: The room temperature PXRD patterns of x = 1.4–2.0. 84

Figure 4.7: Variable temperature PXRD of the x = 1.2 sample showing an increase in lattice parameter with increasing temperature. The structure remains cubic below the magnetic transition at 40 K. 88

Figure 4.8: Variable temperature PXRD of the x = 1.4 sample showing an increase in lattice parameter with increasing temperature for both the cubic and the trigonal phase. The phase composition is constant with temperature. 89

Figure 4.9: Cell parameters for the x = 0–0.4 samples as a function of temperature. The tetragonal to cubic transition is defined here as the temperature at which *a*2 and *c* converge. 92

Figure 4.10: a) PXRD patterns of the four structural regions for the $Ba_xSr_{2-x}NiOsO_6$ (x = 0.2–2) system, b) Volume/Z at room temperature as a function of barium amount, c) structural phase diagram where the solid lines separates structural regions and the dash lines separate the paramagnetic state from the magnetic ground state. 93

Figure 4.11: AC magnetic susceptibility for x = 0.6 and x = 1.2. 97

Figure 4.12: a) Temperature dependent magnetic susceptibility for x = 0.2–1.2 with a cusp at 40 K, b) temperature dependent magnetic susceptibility measured with field-cooled condition for x = 0.2–2.0, c) isothermal magnetization at 5 K for x = 0.2–1.2, d) isothermal magnetization at 5 K for x = 1.4–2.0. 99

Figure 4.13: a) Specific heat measurement for x = 1.2 sample. No feature is observed around 40 K which indicates the cusp in the magnetic susceptibility data is not a long range ordered state, b) difference between the 5 K pattern and 10 K, 25 K, 50 K, and 60 K for $Ba_{1.2}Sr_{0.8}NiOsO_6$..... 102

Figure 4.14: a) Magnetic reflections that appeared below 100 K, b) the refined magnetic structure of Ba_2NiOsO_6..... 105

Figure 4.15: At high barium concentration at the *A*-site, the solid solution $Ba_xSr_{2-x}NiOsO_6$ adopts the trigonal space group (right) to accommodate the large size of the barium. 106

Figure 4.16: a) 90° superexchange results in antiferromagnetic Ni–Os interaction, b) 180° superexchange results in ferromagnetic interaction between the half-filled Ni e_g and empty Os e_g orbitals, c) the perovskite structure houses both short range (J_1) and long range (J_2, J_3) magnetic interactions, while the trigonal structure is dominated by short range (J_1, J_4) magnetic interactions. 109

Chapter 1 Introduction

1.1 The Unique Magnetism of 5d Materials

Materials containing 5d transition metals have unique magnetism stabilized by an interplay between spin, orbital, charge, and lattice degree of freedom which has yet to be fully understood. Materials containing 3d transitions metals have the magnetic properties that can be accurately predicted by the Goodenough-Kanamori rules for superexchange. However, the magnetism involving 5d orbitals is not fully understood. The 5d transition metals have higher spin-orbit coupling compared to the 3d transition metals. The 5d orbitals also have stronger hybridization with oxygen that redistributes spin density and results in high sensitivity to lattice distortions. In addition, in many perovskites containing 5d, the e_g orbitals are highly antibonding and therefore always empty and quite far from the Fermi level. This results in magnetism driven mainly by the t_{2g} orbitals.[2–4] These unique properties result in a rich variety of magnetism.[5–11] In order to better understand the potential of these materials, the relationship between the spin, orbital, and lattice degree of freedom and the magnetic ground state of 5d double perovskite and double perovskite-related phase was investigated.

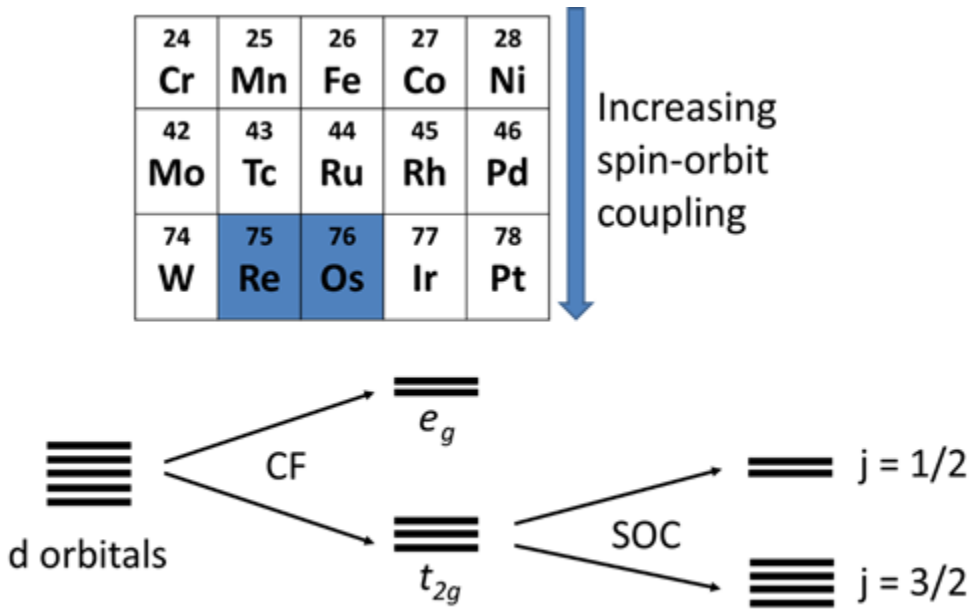

Figure 1.1: 5d transition metals have higher spin-orbit coupling than 4d and 3d transition metals. Octahedral crystal field splits the degenerate d orbitals into the e_g and t_{2g}. Spin-orbital coupling further splits the t_{2g} into j = 1/2 and j = 3/2 states.

1.2 Perovskite Structure

Compounds with the perovskite structure have a wide range of properties such as ferroelectricity, piezoelectricity, superconductivity, mixed electronic and ionic conductivity.[12–16] The simplest structural analog with the perovskite structure has the chemical formula ABX_3. The *A* cation is in a twelve-coordinated cuboctahedron environment and the *B* cation is in a six-coordinated octahedral environment. The *X* site can be occupied by an anion such as an oxide or halide ion. For the scope of this dissertation the *X* site will be limited to the oxide ion only. The structure is a network of corner-connected BX_6 octahedra stabilized by the A-site cation in the cuboctahedron cavity. This

corner connected octahedral framework which can expand, contract, or tilt to accommodate a variety of ion size ratios that are non-ideal. The Goldschmidt tolerance factor (t) is ratio of ionic radii of cations and anions that describes how well the ions that make up the perovskite structure fit together.[17] A tolerance factor equal to one is ideal to stabilize the ideal cubic perovskite with the space group $Pm\bar{3}m$.

$$t = \frac{r_A + r_O}{\sqrt{2}\,(r_B + r_O)}$$

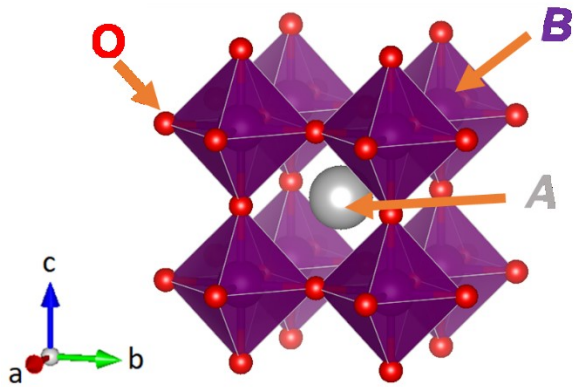

Figure 1.2: Simple cubic perovskite structure with the chemical formula ABO_3.

1.3 Double Perovskite Structure with 1:1 ordering

Different perovskite analogs can form by ordering of two different cations at the *A* site or the *B* site. The double perovskite structure is one where two kind of cations (*B* and *B′*) occupy the *B* site in an ordered fashion such that the structure consists of alternating corner-connected BO_6 and $B'O_6$ octahedra. An alternative way of visualizing the structure is to think of it as two interpenetrating face-centered cubic lattice of *B* and *B′* cations. The magnitude of the charge and ionic size difference between the *B* and *B′* cations plays a significant role in the ordering of these cations. A larger difference in either charge or size

results in high degree of ordering of the B and B' sites which can be observed by the appearance of the odd *hkl* reflections in the X-ray diffraction pattern such as the (111) peak.

The tolerance factor (t) is calculated using an average of the B and B' ionic radii. In the context of this dissertation, the A site is a diamagnetic alkali earth metal; the B site is an alkali metal, alkaline earth metal, or a 3d transition metal; the B' cation is a 5d transition metal. Double perovskites are a great playground for studies of magnetism due to the fact that one can place a wide variety of different cation combinations at the B and B' sites and investigate different magnetism as a function of different combination of d electron count.

$$t = \frac{r_A + r_O}{\sqrt{2}\,(\frac{r_B + r_{B'}}{2} + r_O)}$$

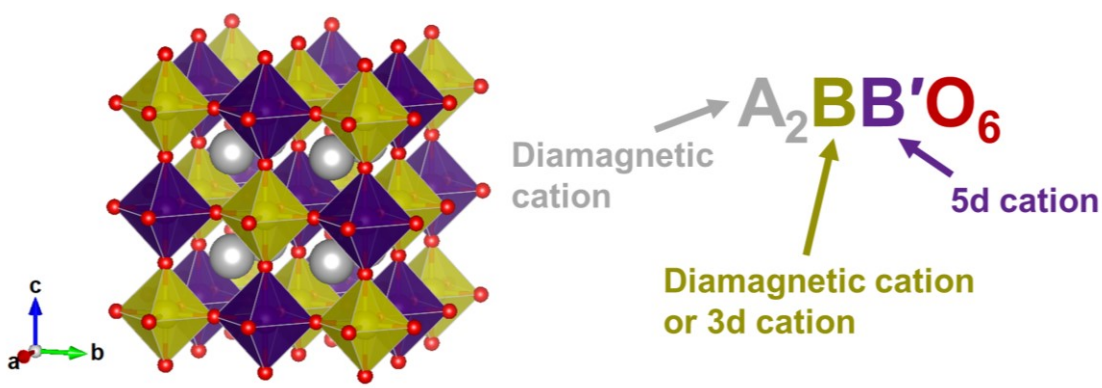

Figure 1.3: Double perovskite structure with the chemical formula $A_2BB'O_6$.

1.4 Tolerance Factor and Octahedral Tilting

In an ideal cubic perovskite, the A–O bond length is $\sqrt{2}$ times longer than the B–O bond length, and the tolerance factor is 1. The space group for the cubic double perovskite is $Fm\bar{3}m$. When the tolerance factor is less than 1, the perovskite framework compensates

for the size mismatch via tilting of the BO_6 octahedra. As the tolerance factor decreases, the amount of octahedral tilting increases, results in a lowering of symmetry from $Fm\bar{3}m$. The space group then is dependent on the direction and magnitude of the octahedral tilting (Table 1.1). Octahedral tilting is usually described by the Glazer notation which is composed of three letters with by a superscript for each letter.[18,19] The letters specify the magnitude of the tilt along the three crystallographic axes, and the superscripts designate the relative direction of tilts in successive layers along each axis. A superscript of "0" indicates no tilting, "+" indicates in-phase tilt, and "–" indicates out-of-phase tilt. For example, one of the common tetragonal ordered double perovskites is the $I4/m$ space group with the octahedral tilting scheme $a^0a^0c^-$. In this structure the octahedral tilting is out of phase in the c crystallographic direction. Lattice parameters of the tetragonal double perovskite in comparison to the cubic double perovskites are usually $a_t \approx a_c/\sqrt{2}$ and $c_t \approx a_c$ where a_t and c_t are tetragonal lattice parameters and a_c is the cubic lattice parameter. Monoclinic ordered double perovskites adopting the space group $P2_1/n$ $(a^-a^-c^+)$ have octahedral tilts that are out-of-phase about the a and b axes and in-phase about the c axis. Lattice parameters of the monoclinic double perovskite unit cell are $a_m \approx a_c/\sqrt{2}$, $b_m \approx a_c/\sqrt{2}$, and $c_m \approx a_c$ where a_m, b_m, c_m are monoclinic lattice parameters and a_c is the cubic lattice parameter.

Some of the most common space group for double perovskites distorted from cubic symmetry are $I4/m$ $(a^0a^0c^-)$, $R\bar{3}$ $(a^-a^-a^-)$, $I2/m$ $(a^0b^-b^-)$ and $P2_1/n$ $(a^-a^-c^+)$. Structural phase transitions from one tilt system to another can occur as a function of temperature, often to lower symmetries with decreasing temperature.

Table 1.1: Double perovskites tilt systems and space groups.[20]

Tilt system number	Tilt system symbol	Space group (no ordering)	Space group (1:1 ordering in double perovskite)
Three-tilt system			
1	$a^+ b^+ c^+$	*Immm*	*Pnnn*
2	$a^+ b^+ b^+$	*Immm*	*Pnnn*
3	$a^+ a^+ a^+$	$Im\bar{3}$	$Pn\bar{3}$
4	$a^+ b^+ c^-$	*Pmmn*	*P*2/*c*
5	$a^+ a^+ c^-$	$P4_2/nmc$	$P4_2/n$
6	$a^+ b^+ b^-$	*Pmmn*	*P*2/*c*
7	$a^+ a^+ a^-$	$P4_2/nmc$	$P4_2/n$
8	$a^+ b^- c^-$	$P2_1/m$	$P\bar{1}$
9	$a^+ a^- c^-$	$P2_1/m$	$P\bar{1}$
10	$a^+ b^- b^-$	*Pnma*	$P2_1/n$
11	$a^+ a^- a^-$	*Pnma*	$P2_1/n$
12	$a^- b^- c^-$	$F\bar{1}$	$F\bar{1}$
13	$a^- b^- b^-$	*I*2/*a*	$F\bar{1}$
14	$a^- a^- a^-$	$R\bar{3}c$	$R\bar{3}$
Two-tilt system			
15	$a^0 b^+ c^+$	*Immm*	*Pnnn*
16	$a^0 b^+ c^+$	*I*4/*mmm*	$P4_2/nnm$
17	$a^0 b^+ c^-$	*Cmcm*	*C*2/*c*
18	$a^0 b^+ b^-$	*Cmcm*	*C*2/*c*
19	$a^0 b^- c^-$	*I*2/*m*	$I\bar{1}$
20	$a^0 b^- b^-$	*Imma*	*I*2/*m*
One-tilt system			
21	$a^0 a^0 c^+$	*P*4/*mbm*	*P*4/*mnc*
22	$a^0 a^0 c$	*I*4/*mcm*	*I*4/*m*
Zero-tilt system			
23	$a^0 a^0 a^0$	$Pm\bar{3}m$	$Fm\bar{3}m$

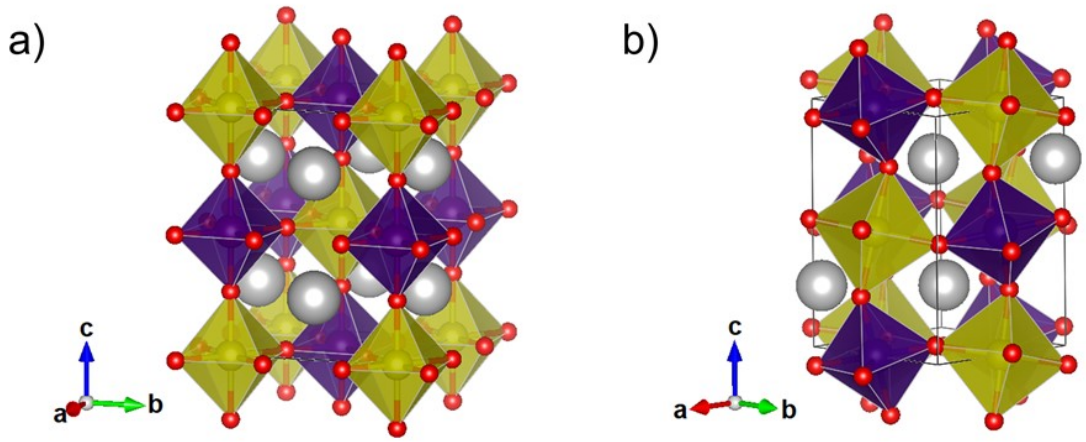

Figure 1.4: a) Tetragonal $I4/m$ double perovskite, b) monoclinic $P2_1/n$ double perovskite.

When the tolerance factor is greater than 1, the *A* site cation is too large to occupy the cuboctahedron cavity. Octahedral tilting cannot compensate for this size mismatch, and the formation of hexagonal perovskite derivatives are often observed.

1.5 Hexagonal Perovskite Derivatives

Hexagonal ABX_3 perovskite derivatives differ from the perovskite structure by the stacking of the BX_6 layers. The cubic perovskite structure can be visualized as a cubic close-packing of the AX_3 layers. When AX_3 layers adopt a hexagonal close packing along the *c* crystallographic direction with the *B* cation occupying the octahedral holes, each BO_6 octahedron shares two faces with neighboring octahedra and forms chains. This results in the 2H hexagonal structure with chains of face-sharing octahedra along the *c* crystallographic direction. AX_3 layers can also stack in a mixture of cubic close packing and hexagonal close packing, which result in a variety of polytypes of hexagonal perovskite structures with different connectivity of face-sharing units. Prototypes of hexagonal structures are

described by a number denoting the number of layers and a letter indicating the type of cell. Common types of hexagonal structures include 2H (a hexagonal unit cell with two layers), 6H (hexagonal cell with six layers), and 9R (rhombohedral cell with nine layers).[21–25]

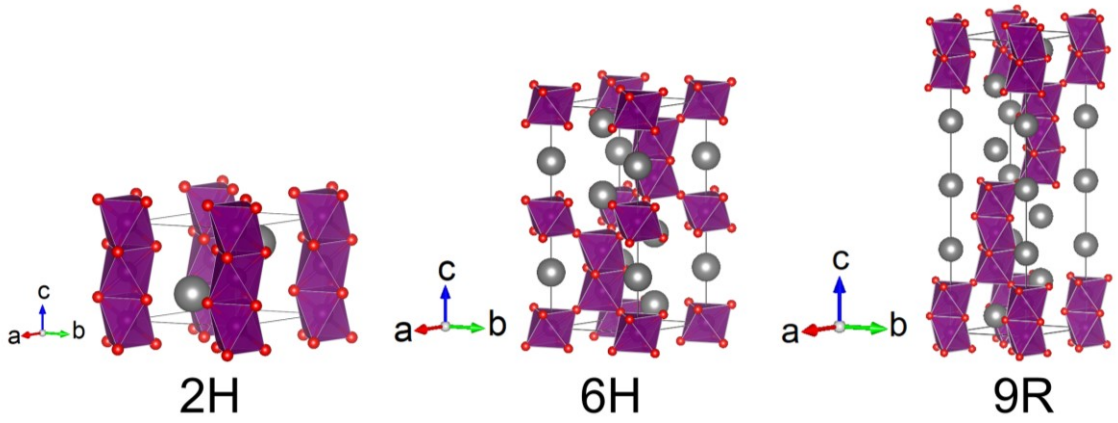

Figure 1.5: Different types of hexagonal perovskite derivatives. The number indicate number of layers, and the letter indicates the type of unit cell (hexagonal or rhombohedral). Figures made from cif files of reference 23–25.

1.6 Types of Magnetic Ground States

Materials containing cations with unpaired electrons can exhibit magnetic ordering depending on the size of the magnetic moment and the interactions between the magnetic cations. The magnetization of the sample is often described relative to the applied measuring field, in terms of magnetic susceptibility. Magnetic susceptibility is the magnetization divided by the applied field and normalized by volume, mass, or moles of sample. By measuring magnetic susceptibility as a function of temperature or

magnetization as a function of applied field, the type of magnetic ordering can be determined.

Materials can be categorized by their magnetism as diamagnets, paramagnets, antiferromagnets, ferromagnets, or ferrimagnets. A diamagnetic material is a material with atoms that have no permanent magnetic dipole moments and weakly repel magnetic fields. As a result, they have a very weak negative magnetic susceptibility. A paramagnetic material is a material with atoms that have magnetic dipole moments originating from unpaired electrons, but the orientations of the local magnetic moments are dynamic. The magnetic moments tend to align parallel to a magnetic field, the extent of which depends upon the temperature, and as a result the magnetic susceptibility for a paramagnet is positive. The temperature dependence of the magnetic susceptibility of a paramagnet as a function of temperature can be mathematically described by the Curie-Weiss law:

$$\chi = \frac{M}{H} = \frac{\mathrm{C}}{(\mathrm{T} - \theta)}$$

where χ is the magnetic susceptibility in unit of emu mol^{-1} Oe^{-1}, M is the magnetization in emu per mol, H is the applied field in Oe, C is the Curie constant, T is temperature, and θ is the Weiss constant. The sign of the Weiss constant signals the type of coupling between the magnetic moments. For a paramagnet, the Weiss constant is zero. A positive Weiss constant indicates ferromagnetic interactions or magnetic moments that have a tendency to align parallel to each other, while a negative Weiss constant indicates antiferromagnetic interactions or antiparallel arrangement of magnetic moments. The Curie constant is related to the effective moment by

$$\mu_{eff}\ (\mu_B) = \sqrt{\frac{3k_B C}{N_A {\mu_B}^2 \mu_0}} = 2.828\sqrt{C}\ (cgs)$$

where k_B is Boltzmann constant, N_A is Avogadro's number, μ_0 is vacuum permeability, and μ_B is Bohr magneton. When interactions between local moments become strong enough to overcome thermal fluctuations, they can form a long range ordered state. Ordered magnetic states of a material can be classified as antiferromagnetic, ferromagnetic, or ferrimagnetic. In an antiferromagnetic state, the magnetic moments align antiparallel to each other in a manner such that the overall magnetization of the material is zero. The temperature at which the magnetic moment ordered in an antiferromagnetic state is called the Néel temperature (T_N). If the magnetic susceptibility is plotted as a function of temperature a peak or cusp should be observed at the Néel temperature. By fitting the magnetic susceptibility data above the Néel temperature to the paramagnetic Curie-Weiss function, the Weiss constant should be negative, consistent with antiferromagnetic local interactions. The isothermal magnetization for an antiferromagnetic material is linear with applied field.

In a ferromagnetic state, the magnetic moments align parallel to each other such that the overall magnetization of the sample is not zero. There is a sharp rise in the magnetic susceptibility at the ordering Curie temperature (T_C) when the magnetic moments are aligned in the same direction. Fitting the magnetic susceptibility data above the Curie temperature to the paramagnetic Curie-Weiss function yields a positive Weiss constant, indicating ferromagnetic local interactions. The isothermal magnetization for a ferromagnetic material increases nonlinearly with applied field and shows hysteresis, such that when the field is removed the material retain a portion of the magnetization.

In a ferrimagnetic state, the magnetic moments align antiparallel to each other, however, because different magnetic moments have different size, the overall magnetization of the material is not zero because the magnetic moments do not cancel each other completely. Similar to the ferromagnetic state, the magnetic susceptibility exhibits a sharp rise in the magnetic susceptibility at the ordering Curie temperature (T_C). However, unlike the ferromagnetic state, due to the antiferromagnetic local interactions, the Weiss constant extracted from fitting the high temperature magnetic susceptibility data above T_C is negative. The isothermal magnetization for a ferrimagnetic material also increases nonlinearly with applied field and shows hysteresis.

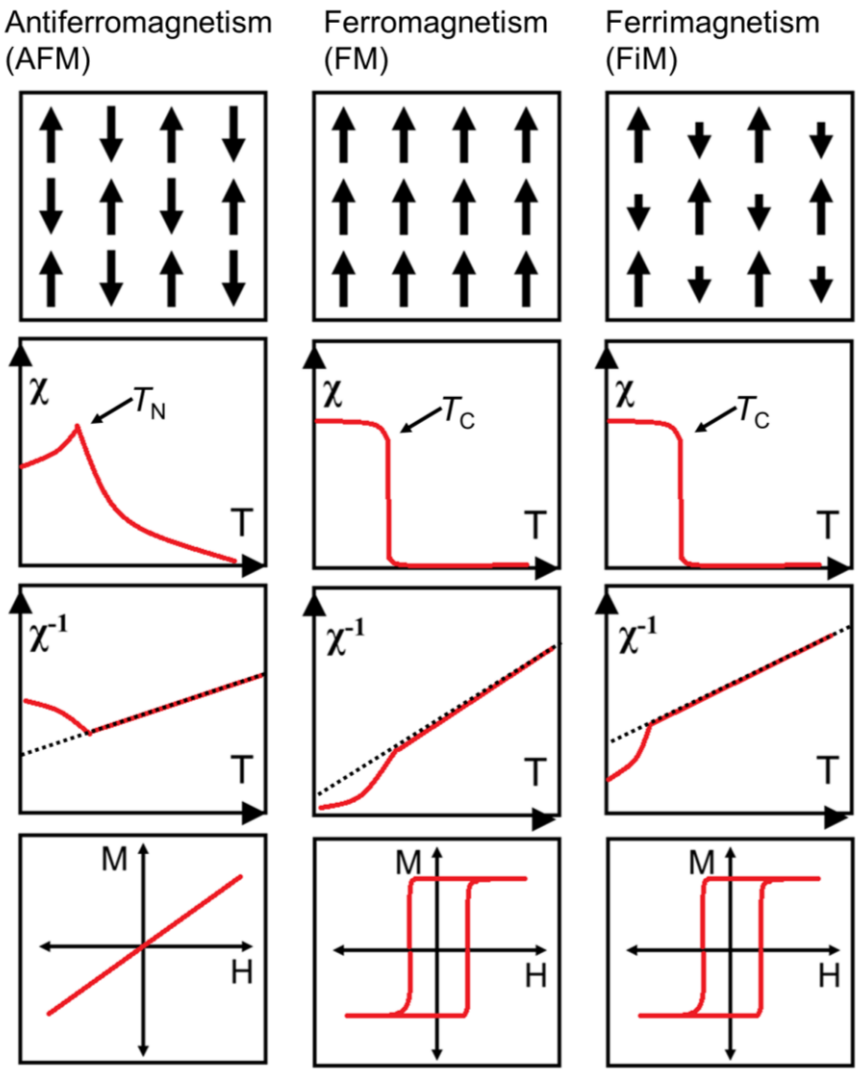

Figure 1.6: Antiferromagnetic, ferromagnetic, and ferrimagnetic ground states and their features in the magnetic measurements.

Neutron diffraction is an elastic scattering technique used to determine both crystal and magnetic structure. Incident neutrons are scattered by atomic nuclei giving rise to diffraction patterns, where the intensity is different for different isotopes. Since the neutron carries a spin, it can also interact with the magnetic moments in the material. Diffraction

peaks that appear when the neutron diffraction data is collected below the magnetic ordering temperature can be indexed to determine the spin arrangement in a magnetic unit cell.

1.7 Superexchange

Superexchange is the magnetic interactions between two magnetic cations through virtual electron transfer mediated by a nonmagnetic cation. A set of semi-empirical rules were developed by Goodenough and Kanamori called the Goodenough-Kanamori rules that successfully rationalized the sign of the magnetic exchange between 3d transition metal cations bridged by an anion.[26,27] In general, the rules state that superexchange interactions are antiferromagnetic if the virtual electron transfer occurs between two half-filled orbitals, and ferromagnetic if the virtual electron transfer occur between a half-filled and an empty orbital.

1.8 180° Cation-Anion-Cation interactions

Superexchange between e_g orbitals of cations that are in a linear bond through a ligand occurs via virtual electron transfer with electrons of opposite spin to the respective *d* orbitals. This typically means that 180° superexchange is antiferromagnetic between cations that both have empty e_g orbitals and ferromagnetic between a cation that has a half-filled e_g orbital and one with an empty e_g orbital. In addition, cation-anion-anion-cation long range superexchange can happen but typically the magnitude is significantly reduced as the number of orbitals involved in the superexchange pathway increases.[27] The sign of the interactions are similar to the short range interactions.

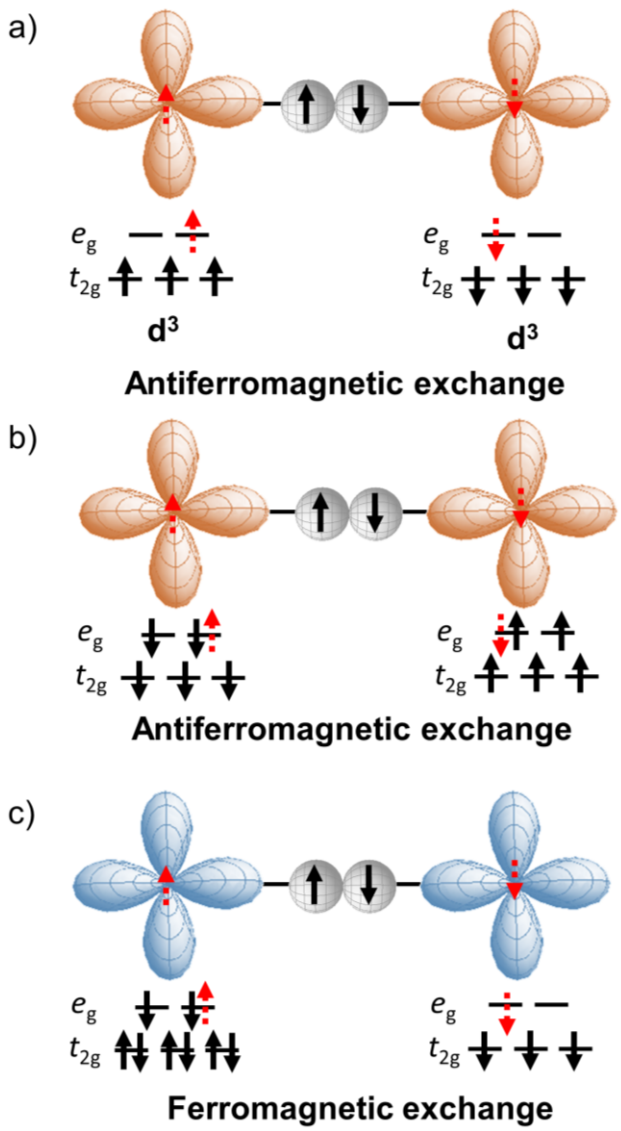

Figure 1.7: For 180° superexchange mediated by a diamagnetic anion (gray), antiferromagnetic coupling occurs between a) empty e_g orbitals or b) half-filled e_g orbitals, while ferromagnetic coupling occurs between c) half-filled e_g and empty e_g orbitals. The black spins are the intrinsic spin of the electron that occupies the orbital, and red dashed spins are virtual electron transfers. Figures made from Wolfram Alpha orbital viewer plug in for Mathematica.

1.9 90° Cation-Anion-Cation interactions

Superexchange between e_g orbitals of cations that are 90° from each other can occur with an intermediary anion where electrons of the same spin from different *p* orbitals are simultaneously excited into the e_g orbitals of the two interacting cations.[27] Unlike the 180° superexchange, the donating electrons have the same spin, so that the holes left behind on the diamagnetic linker follow Hund's rule. Depending on the electron filling, 90° superexchange can be ferromagnetic or antiferromagnetic. When the e_g orbitals of the two interacting cations are empty, the anion donates electron with spin of the same direction to the e_g orbital of both. By Hund's rule, the electrons in the t_{2g} orbital would have the same spin, which results in ferromagnetic exchange between the two cations (Figure 1.8a). When the e_g orbitals of the two interacting cations are both half-filled, the 90° superexchange through the e_g orbitals is ferromagnetic (Figure 1.8b). When the e_g orbital on one of the cations is half-filled and the e_g orbital on the other cation is empty, this results in antiferromagnetic exchange, given no t_{2g} interactions (Figure 1.8c).

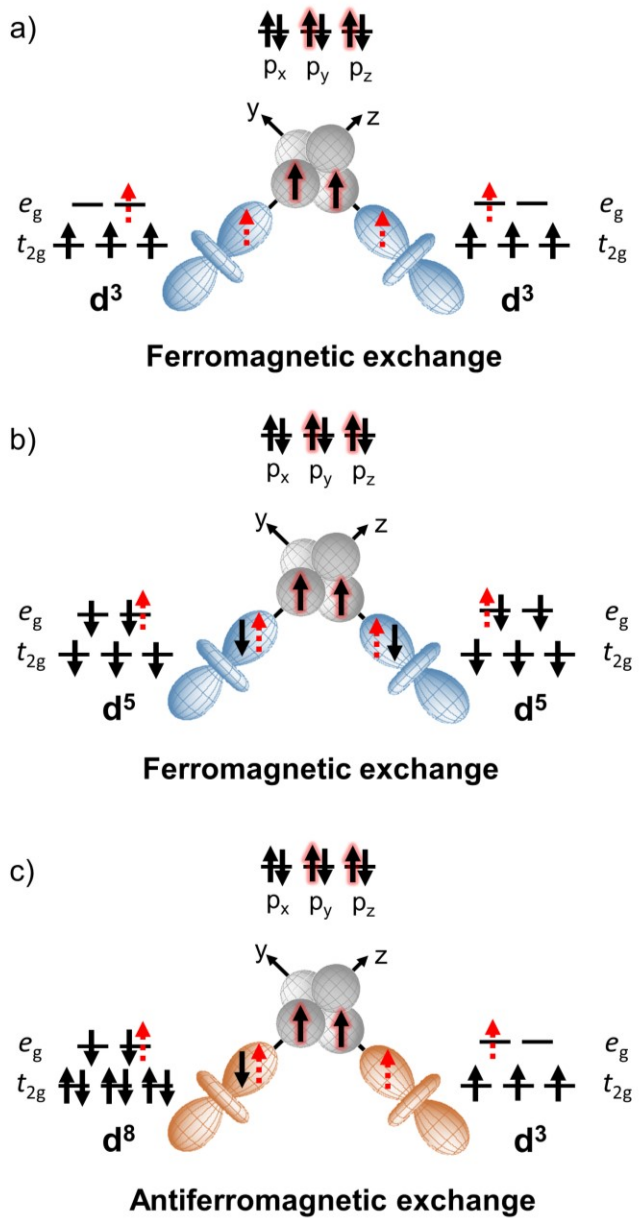

Figure 1.8: 90° superexchange through anion *p* orbitals (gray) between a) empty e_g orbitals, b) half-filled e_g orbitals, c) half-filled e_g orbitals and empty e_g orbitals. The black spins are the intrinsic spin of the electron that occupies the orbital, and red dashed spins are virtual electron transfers. Figures made from Wolfram Alpha orbital viewer plug in for Mathematica.

1.10 Magnetic ordering in simple perovskites

The magnetic structure can be solved from analysis of the neutron diffraction collected below the magnetic transition temperature, where the diffraction peaks contain contributions from both nuclear and the magnetic scattering. For a simple cubic perovskite, there are numerous ways to arrange the magnetic moments. The most common being type A, C, and G. Type A can be visualized as a spin arrangement of ferromagnetic layers with antiferromagnetic inter-plane coupling. The propagation vector that describes the magnetic unit cell is either (1/2, 0, 0), (0, 1/2, 0), or (0 0 1/2) for a cubic perovskite where all three directions are equivalent. The k vector indicates a doubling of the magnetic unit cell from the crystal unit cell in one of the crystallographic direction: *a*, *b*, or *c*. This results in a magnetic unit cell with double the volume of the crystal unit cell. Type C antiferromagnetic structure can be described as a spin arrangement of antiferromagnetic coupling intra-layer, and ferromagnetic coupling interlayer. The propagation vector that describes the magnetic unit cell is (1/2, 1/2, 0), (0, 1/2, 1/2), or (1/2 0 1/2) for a cubic perovskite. The k vector indicates that the magnetic unit cell is doubled in two crystallographic directions in comparison to the crystal unit cell, which results in the magnetic unit cell with quadruple the volume of the crystal unit cell. Type G antiferromagnetic structure consists of intra-layer and interlayer antiferromagnetic coupling, described by the k propagation vector (1/2 1/2 1/2). Here, the magnetic unit cell is doubled in all three directions relative to the crystallographic unit cell, resulting in the magnetic unit cell with 8 times the volume of the crystal unit cell.

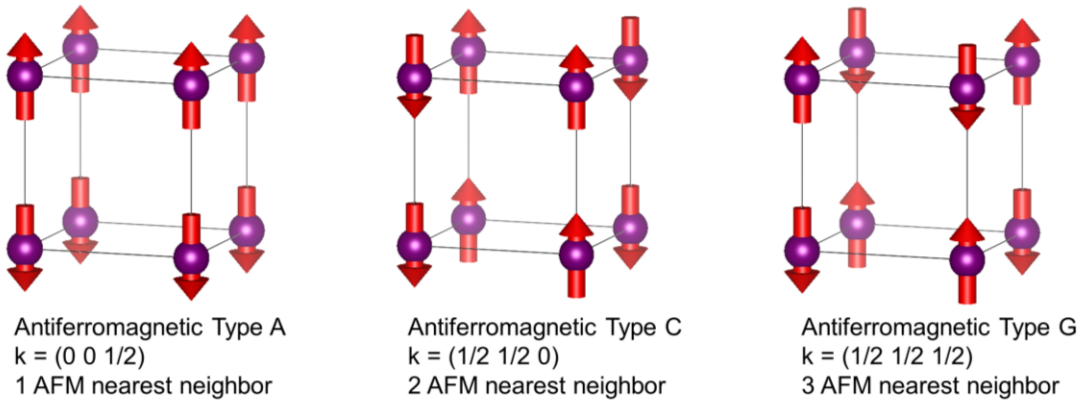

Figure 1.9: Different type of antiferromagnetic ordering for the simple perovskite structure. The magnetic moments are arranged on the crystallographic unit cell to highlight the spin arrangements. This is not representative of the magnetic unit cell.

1.11 Magnetic ordering in double perovskites

In the double perovskite $A_2BB'O_6$, the B and B' sublattices are face centered cubic, which is highly frustrated. Magnetic frustration occurs when not all magnetic interactions can be satisfied, often due to a geometric constraint. The simplest example of magnetic frustration is Ising spins arranged in a triangular lattice, where the spins are frustrated because there is no arrangement where all spins can be antiferromagentically coupled to each other. While one pair of spins on this triangular lattice can couple antiferromagnetically, the third spin is frustrated because it cannot simultaneously be antiferromagnetically coupled to both. In the double perovskite lattice, the face centered cubic lattice of magnetic cations is composed of tetrahedral units of that cations, resulting in a highly frustrated system. Interestingly, none of the magnetic structures predicted by

mean field theory exhibit purely antiferromagnetic nearest neighbor interactions, which highlight the frustrated nature of the double perovskite structure.[28]

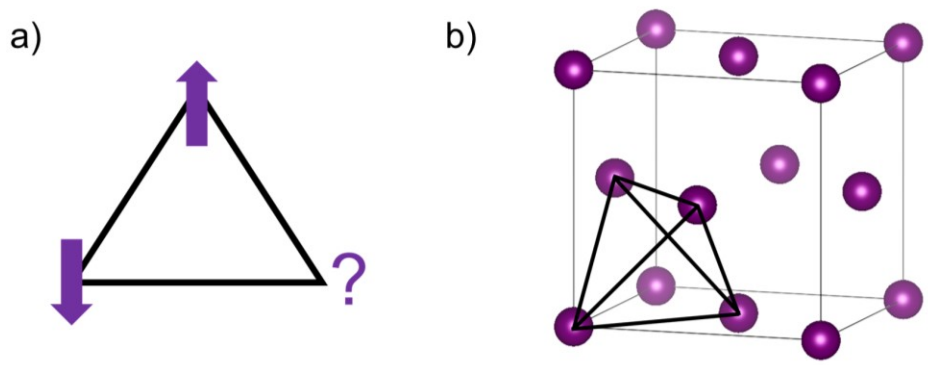

Figure 1.10: a) Frustrated spins arranged on a triangular lattice, b) face center cubic lattice of magnetic cations is a frustrated system due to the tetrahedron arrangement magnetic moments.

The two antiferromagnetic structures that are most commonly observed for double perovskites are shown in Figure 1.11. Type I antiferromagnetic structure with the k vector (0 0 1) can be described a ferromagnetic planes coupled antiferromagnetically along the (0 0 1) direction. Type II antiferromagnetic structure with the k vector (1/2 1/2 1/2) can be described as ferromagnetic planes stacked antiferromagnetically along the (1 1 1) direction.[28]

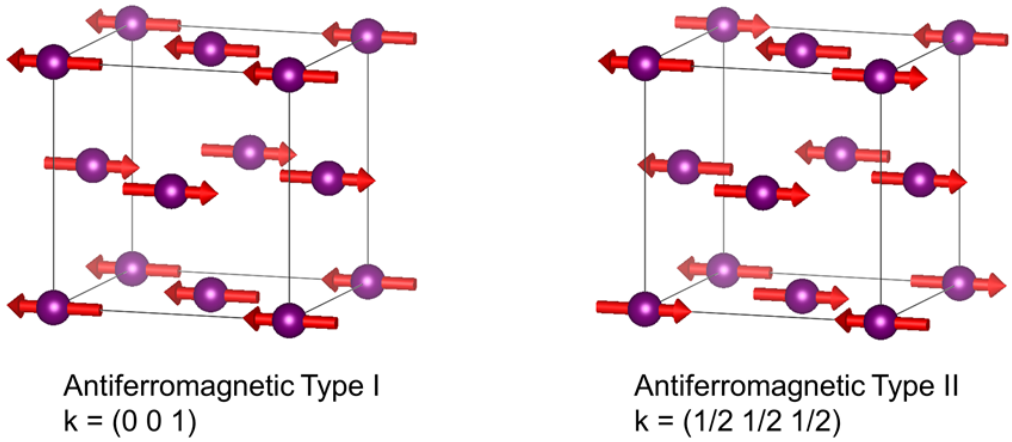

Figure 1.11: Different type of magnetic ordering for double perovskites with one magnetic cation.

Chapter 2 The Effect of Structural Distortion on the $5d^1$ Magnetic Ground State

2.1 Introduction

Materials with high spin-orbit coupling and large electron correlation are interesting due to their wide variety of exotic properties such as spin liquids, Weyl semimetals, topological Mott insulators, and half-metallicity to name a few. In 5d systems, the presence of strong spin orbit coupling is believed to significantly alter the interplay of spin, orbital, charge, and lattice degrees of freedom. In addition, the large size of the 5d orbitals impacts interorbital repulsion and superexchange. This results in a diverse variety of magnetic ground states among the different $5d^1$ compounds.

In general, most 5d double perovskites are antiferromagnetic. Cases of ferrimagnetic or ferromagnetic ordering for double perovskite containing 5d transition metals often involved both 3d and 5d magnetic cations. Without the presence of 3d transition metal, ferromagnetism is only observed in some $5d^1$ double perovskites with cubic structure.

Ferromagnetism has been observed in $5d^1$ cubic double perovskites Ba_2NaOsO_6, Ba_2MgReO_6, and Ba_2ZnReO_6. Unexpectedly, cubic Ba_2LiOsO_6 has an antiferromagnetic ground state. The reason why these isostructural and isoelectronic $5d^1$ double perovskites have different magnetic ground state remains unknown. Previous work on cubic Ba_2ZnReO_6 and isoelectronic tetragonal Ba_2CdReO_6 shows that electronic driven orbital ordering in the cubic compound stabilizes a ferromagnetic ground state, while lattice

distortion driven orbital ordering stabilizes an antiferromagnetic ground state. In cubic Ba_2ZnReO_6, preferential orbital occupation of the d_{xz} and d_{yz} orbitals due to strong interorbital repulsion results in a temperature dependent effective moment and a canted ferromagnetic ground state. Meanwhile, tetragonal distortion in Ba_2CdReO_6 where the 5d octahedra is compressed along the *c* crystallographic direction breaks the degeneracy of the three t_{2g} orbitals and results in preferential occupation of the d_{xy} that stabilizes the antiferromagnetic ground state. This suggests subtle octahedral distortion has a large impact on the overall magnetism of the material.

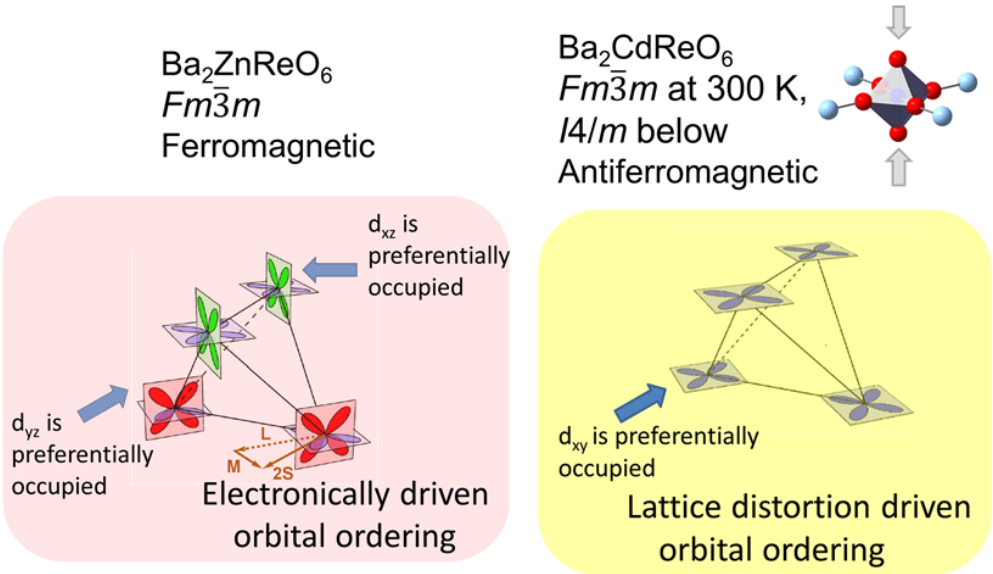

Figure 2.1: Different orbital occupation results in different magnetic ground states in isoelectronic Ba_2ZnReO_6 and Ba_2CdReO_6.

An intriguing puzzle is what happens when the $5d^1$ octahedral environment is distorted in a different ways. The work on the cubic compound suggests that the magnetic

ground state is very sensitive to local distortions. By partially replacing the barium in the *A* site with the smaller strontium, the 5d octahedra will tilt in order to compensate for the smaller cation. In this chapter, we discuss three different distorted $5d^1$ double perovskites Sr_2ZnReO_6, Sr_2LiOsO_6, and Sr_2NaOsO_6 and how changes in crystal structure lead to different magnetic ground state.

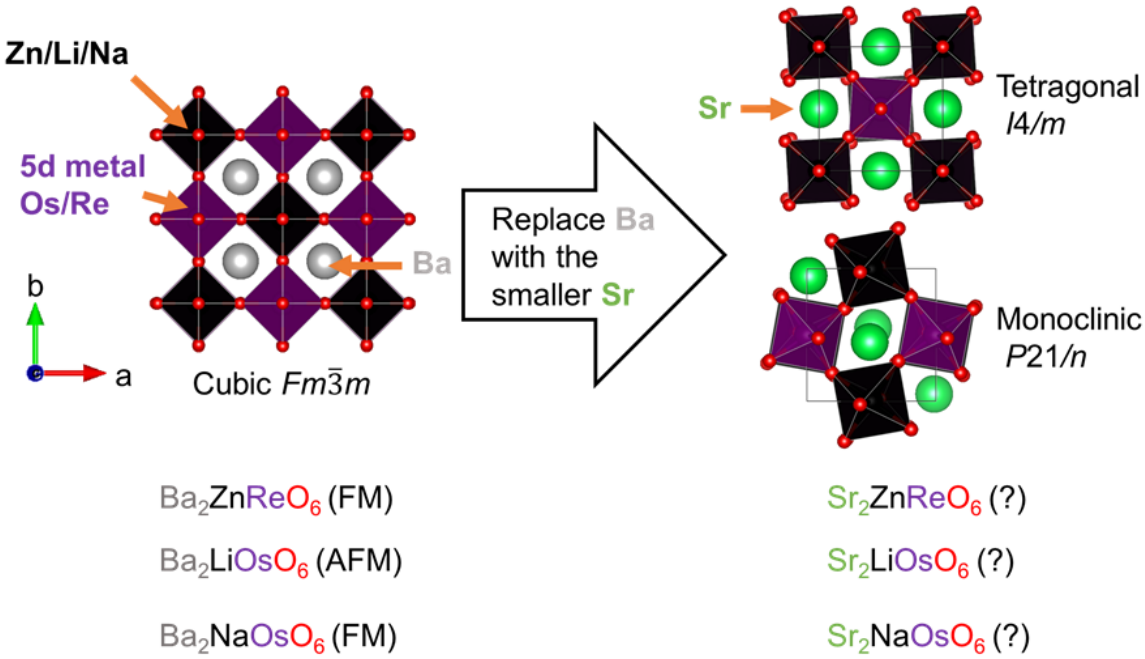

Figure 2.2: The barium site can be substituted with the smaller strontium, which causes octahedral tilting to compensate for its smaller size in the cavity.

2.2 Experimental

Polycrystalline Sr_2ZnReO_6 was synthesized by solid state method. Stoichiometric amounts of SrO (Sigma Alrich, 99.9% trace metals basis), ReO_3 (Alfa Aesar, 99.9% trace metals basis), and ZnO (Alfa Aesar, 99.99% metals basis) were ground together with a mortar and pestle inside an argon glove box due to the moisture sensitivity of the reagents.

The ground reagents were transferred to an alumina tube and covered with an alumina cap. This reaction vessel was sealed in an evacuated quartz tube and heated to 900 °C for 24 hours, and cooled room to room temperature at 1 °C/min. Approximately 1–1.5 gram of product was made per synthesis.

$$SrO\ (s) + ZnO\ (s) + ReO_3\ (s) \rightarrow Sr_2ZnReO_6\ (s)$$

Polycrystalline samples of the osmium double perovskites Sr_2LiOsO_6 and Sr_2NaOsO_6 were also synthesized in a similar manner. Stoichiometric amounts of SrO (Sigma Alrich, 99.9% trace metals basis), Li_2O (Alfa Aesar, 99.5 %), Na_2O_2 (Alfa Aesar, 95 %) and Os powder (Sigma-Alrich, 99.9 % trace metals basis) for a theoretical yield of 1 gram were ground in a mortar and pestle, transferred to an alumina tube, sealed in a quartz tube under vacuum. A separate alumina cap containing PbO_2 was also included in the sealed quartz tube as the decomposition of PbO_2 into PbO and O_2 at 600 °C provided the oxygen source needed to oxidize Os metal. Because a high pressure of gas may form during the synthesis that can cause the reaction tube to rupture, each reaction was synthesized with a theoretical yield of 1 gram. To ensure the full oxidation to Os^{7+}, the quantity of PbO_2 was chosen was sufficient to generate an excess of 1/4 mol of oxygen for every mol of product. The reaction vessel was heated at 1000 °C for 24 hours. However, samples that were larger than 1 gram were not entirely phase pure and required regrinding and reheating. Due to overpressure of oxygen, some of the reaction tubes were cracked which exposed the reaction to air, however, they still formed phase pure products.

$$2\ SrO\ (s) + 1/2\ Li_2O\ (s) + Os\ (s) + 4\ PbO_2\ (s) \rightarrow Sr_2LiOsO_6\ (s) + 4\ PbO\ (s) + 1/4\ O_2\ (g)$$

$$2\ SrO\ (s) + 1/2\ Na_2O_2\ (s) + Os\ (s) + (7/2)\ PbO_2\ (s) \rightarrow Sr_2NaOsO_6\ (s) + (7/2)\ PbO\ (s) + 1/4\ O_2\ (g)$$

Room temperature powder X-ray diffraction (PXRD) data was collected using the Bruker D8 Advance powder diffractometer (40 kV, 40 mA, sealed Cu X-ray tube) equipped with an incident beam monochromator (Johansson type SiO_2 crystal) and a Lynxeye XE-T position sensitive detector. Synchrotron X-ray diffraction data was collected for Sr_2ZnReO_6 at 300 K and 90 K with a wavelength of 0.412781 Å at the APS 11-BM beamline. Synchrotron X-ray diffraction data was collected for Sr_2LiOsO_6 and Sr_2NaOsO_6 at 300 K with a wavelength of 0.82015 Å at the Canadian Light Source Brockhouse X-ray Diffraction and Scattering Beamline (BXDS-WLE). Phase purity and cation ordering were determined by powder Rietveld refinement in TOPAS-Academic (v6).[29] Starting values of the atomic positions used in the refinements were generated with SPuDS.[30]

Magnetic susceptibility as a function of temperature (2 K–400 K) was collected for each sample with an applied field of 1000 Oe in zero field cooled (ZFC) and field cooled (FC) conditions using the Superconducting Quantum Interference Device (SQUID). Approximately 100 mg of sample was loaded in a gelatin capsule and mounted in a plastic straw. Magnetization versus applied field data were taken on the same instrument with an applied field of −70 kOe to 70 kOe at 2 K and 300 K for all samples.

2.3 Results

2.3.1 Structural analysis

Room temperature laboratory X-ray diffraction pattern and synchrotron X-ray diffraction pattern at 295 K of Sr_2ZnReO_6 was fitted to the tetragonal space group $I4/m$. The structure can be described with the octahedral tilting scheme $a^0a^0c^-$ where there is out-of-phase octahedral tilt viewing down the c axis. The refined lattice parameters from the

synchrotron data are a = 5.57572(1) Å and c = 8.00281(2) Å. This is comparable to the previous reported values in the literature of a = 5.5785(1) Å and c = 8.0053(2) Å by Retuerto et al. [31] Attempts to refine anti-site disorder for Zn^{2+} and Re^{6+} in synchrotron data at 295 K and 90 K did not suggest any mixing of the two ions, nor did it result in a significantly meaningful improvement in the goodness of fit. Thus, we conclude that no site disorder between Zn^{2+} and Re^{6+} can be detected within experiment error. The refinement also shows less than 1 % by weight of Re impurity, which is diamagnetic and will not affect magnetic measurement.

The $I4/m$ space group can account for all reflections in the 295 K pattern of Sr_2ZnReO_6, with a small amount of peak asymmetry at different reflections. Previous reports in the literature assigned the room temperature structure of Sr_2ZnReO_6 as a mixed phase of $I4/m$ and $P2_1/n$. [31,32] The two different reports refined the amount of monoclinic $P2_1/n$ phase to be 2.63 % or 15 % by weight. A secondary monoclinic $P2_1/n$ phase with similar lattice parameters was added along with the main phase in order to determine whether there is a small amount of monoclinic phase like the samples in literature. The R_{wp} of fit using only the $I4/m$ model is 17.28 %. Adding a secondary monoclinic phase does improve the fit, dropping the R_{wp} to 12.5 %. However, the pattern can be refined with a large variation in the weight percent of the monoclinic phase, from 6 % to as high as ~40 %, with R_{wp} ranging from 12.5 to 11.9 %. The lowest R_{wp} was achieved with a fit of 40.5(7) % by weight of the monoclinic phase with lattice parameters of a = 5.57980(9) Å, b = 5.5780(1) Å, c = 7.99418(6) Å, and β = 90.125(2) °. However, we assigned the 295 K structure of our Sr_2ZnReO_6 sample to the $I4/m$ space group for two reasons. First, no new reflections or peak splitting associated with the lower symmetry monoclinic structure was

observed. Second, a wide range of possible weight percent for the monoclinic phase give reasonably comparable fit which suggest that these are false minimums. It is possible that structural variations in different grain results in the peak broadening and asymmetry of the diffraction reflections. This can result from a heterogeneous sample with subtle variations in the degree of tetragonal distortion from one grain to another. The peak symmetry that results from structural variation in different grain affects different *hkl* reflections in different ways, so fitting two phases to the PXRD patterns improves the fit. However, the average structure is still tetragonal *I*4/*m*. A second tetragonal phase was added to the fit which drops the R_{wp} from 17.28 % to 12.31 %. The second tetragonal phase had a slightly larger *a* and smaller *c* lattice parameters, which accounts for asymmetry of all observed reflections. The Re–O distances for these phases are close to each other within error.

As the temperature was lowered to 90 K, new reflections and peak splitting in the synchrotron diffraction pattern indicate a lowering of symmetry from the tetragonal *I*4/*m* space group. The pattern was fitted to a monoclinic $P2_1/n$ space group. The structure can be described with the octahedral tilting scheme $a^-a^-c^+$ where there is out-of-phase octahedral tilt down the *a* and *b* axes and in-phase tilting along the *c* axis. The refined lattice parameters are listed in Table 2.1. This suggests the presence of a tetragonal to monoclinic structural transition, which is consistent with the observation in literature that the structural transition of Sr_2ZnReO_6 occurs somewhere above 250 K. [31] The R_{wp} of the fit is 12.087 %. The Re–O distances are close to each other within error.

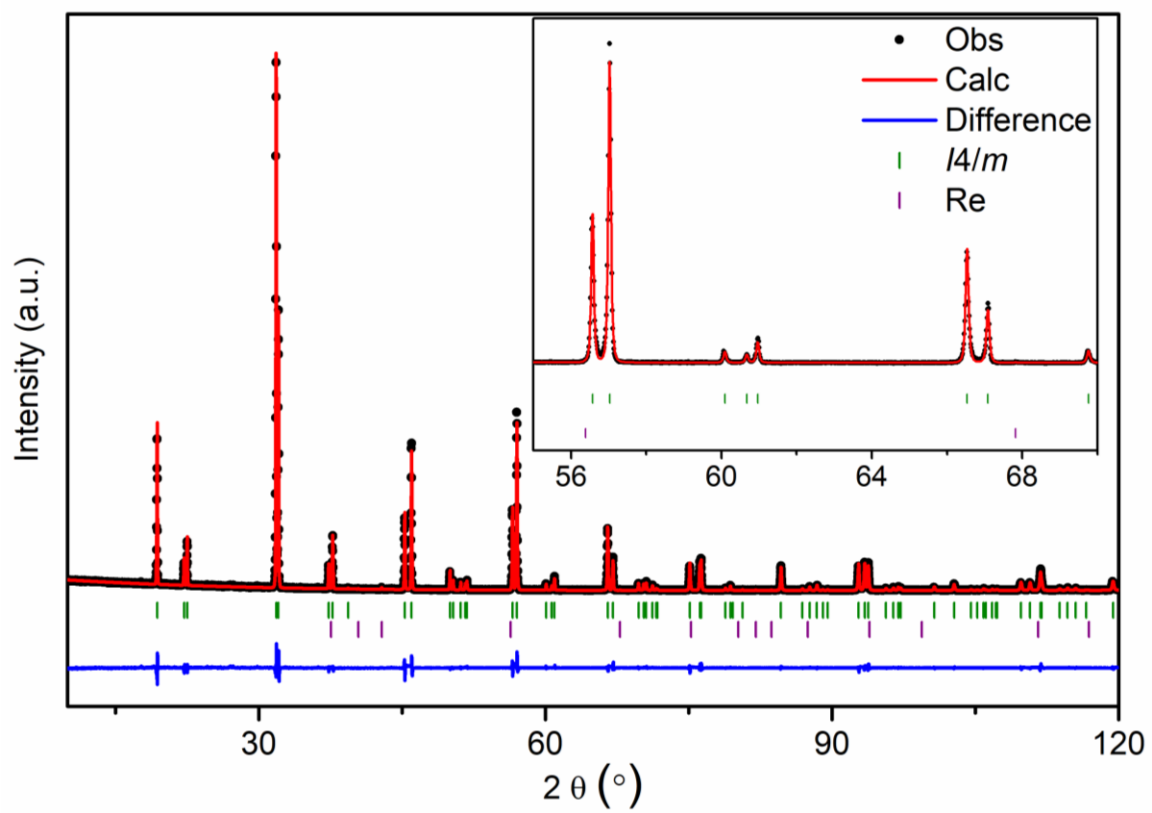

Figure 2.3: Room temperature laboratory diffraction data for Sr_2ZnReO_6.

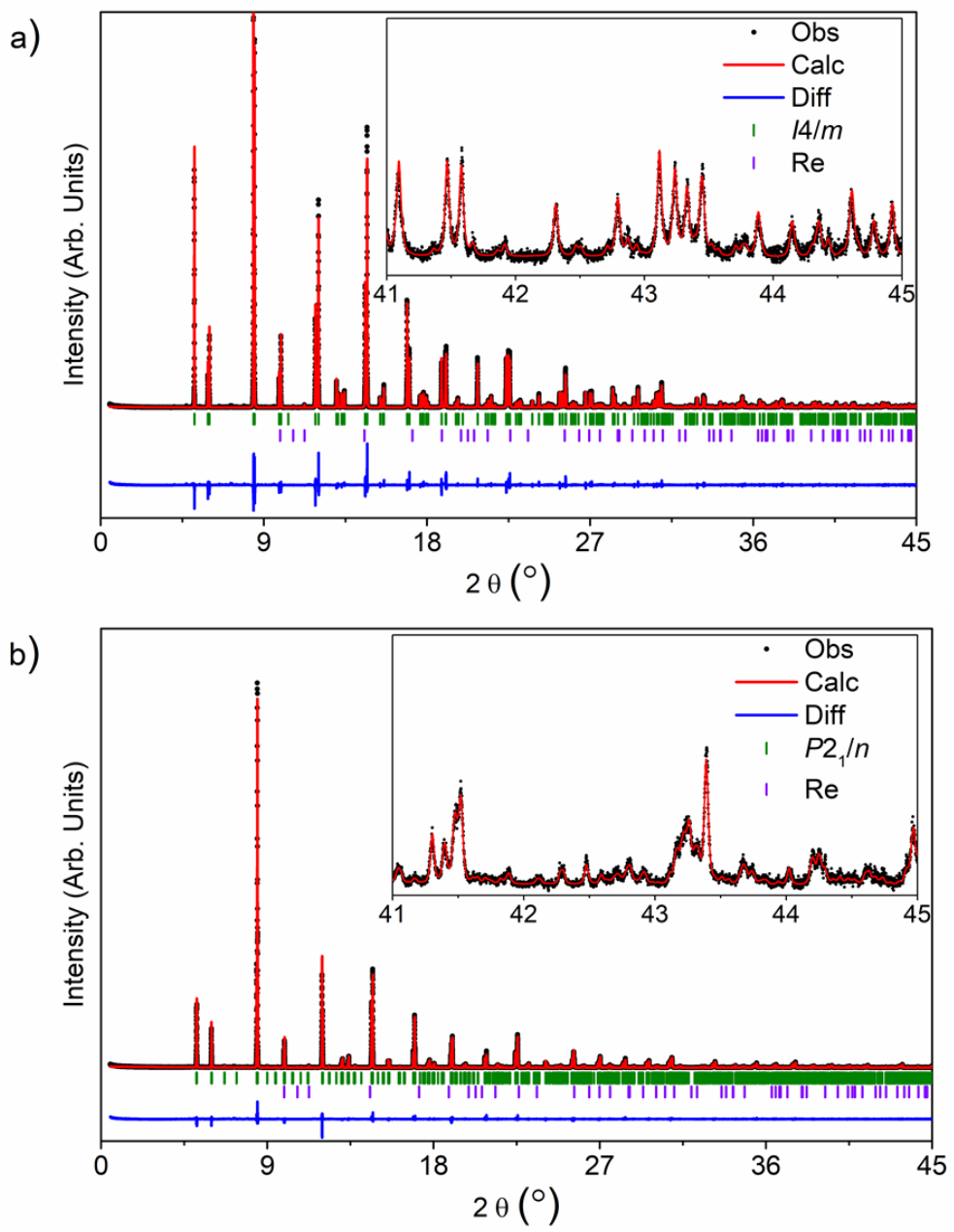

Figure 2.4: SXRD of Sr_2ZnReO_6 at a) 295 K and b) 90 K.

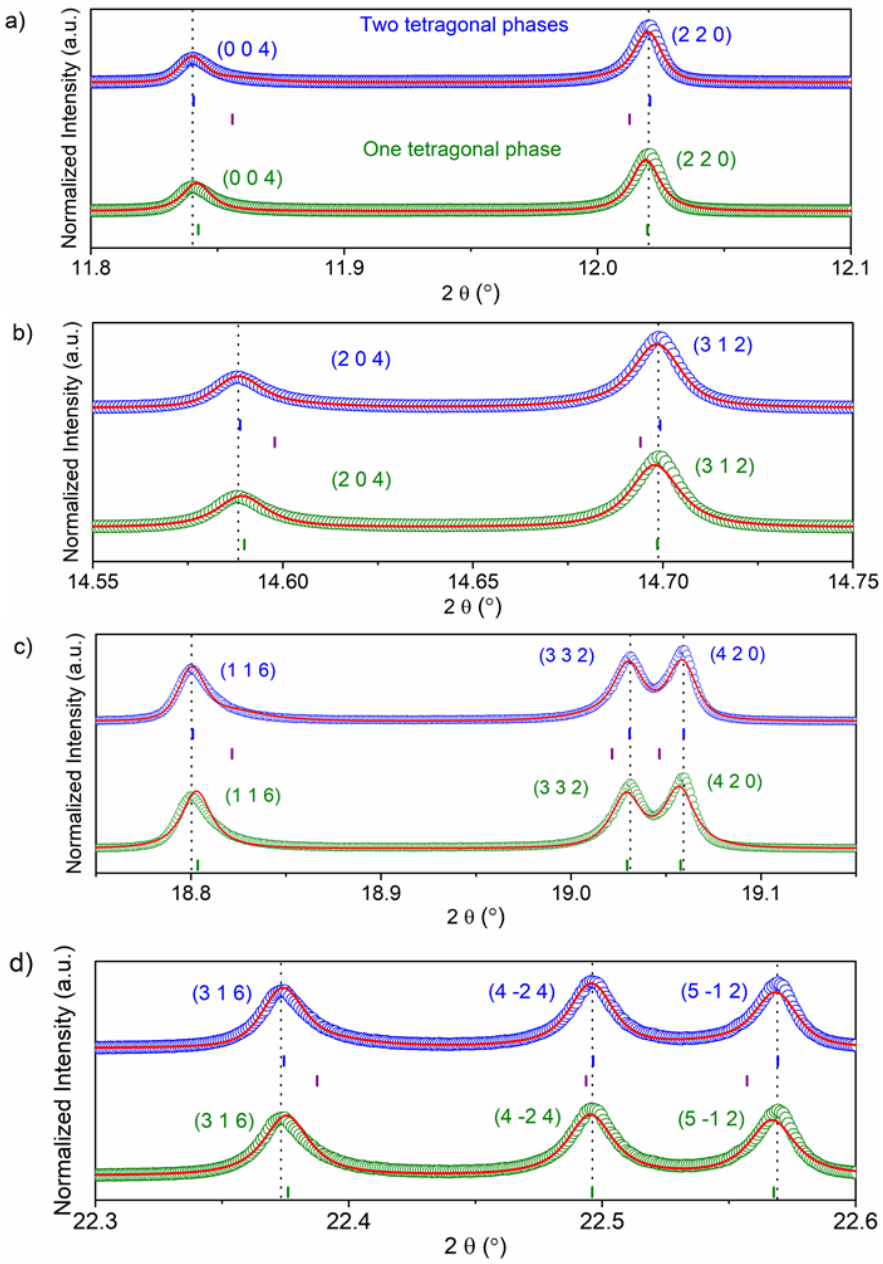

Figure 2.5: The Sr_2ZnReO_6 pattern at 295 K was fitted to one tetragonal phase (bottom, green) and two tetragonal phases (top, blue). The green tickmarks indicate the reflections allowed for one tetragonal phase. The blue and purple tickmarks indicate the reflections for two tetragonal phases. The dotted line represents the highest point of the reflection.

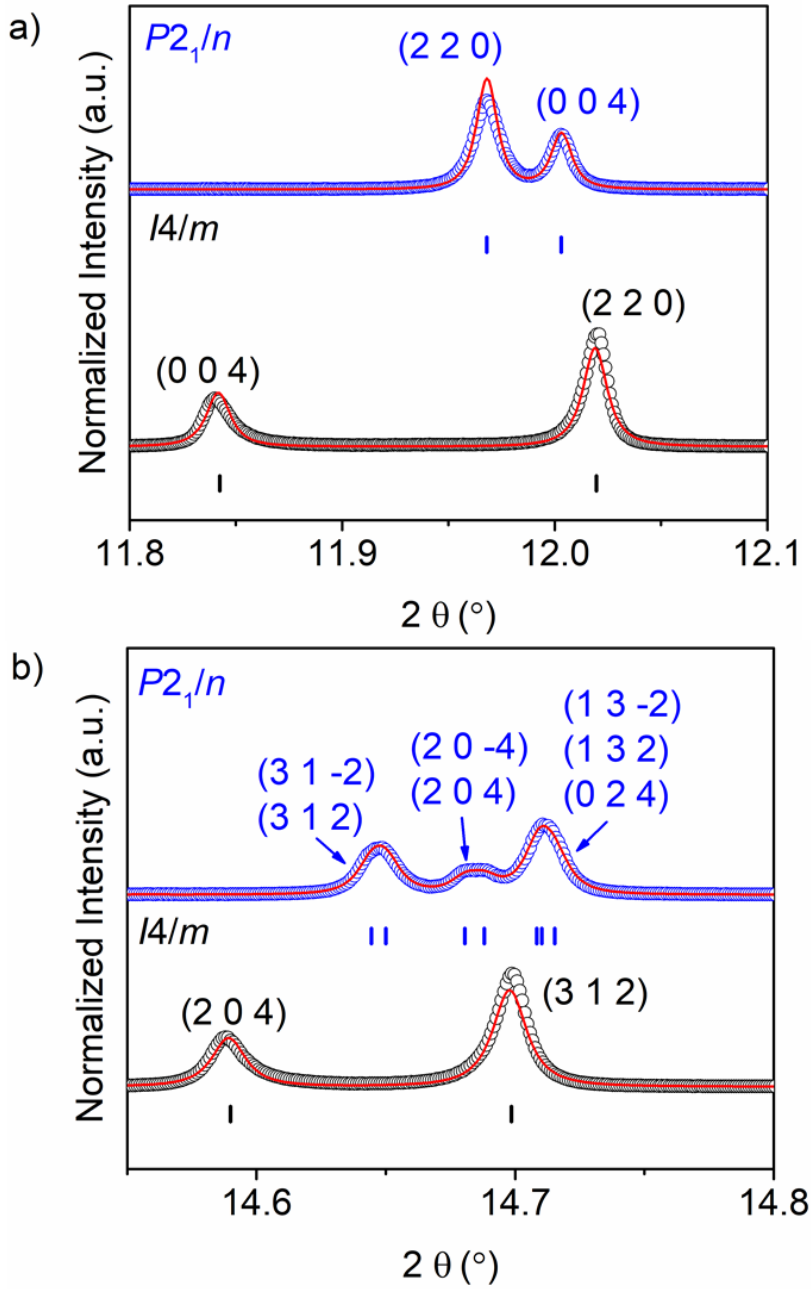

Figure 2.6: Differences in the peak splitting between the *I*4/*m* space group (295 K) and the $P2_1/n$ space group (90 K). The *I*4/*m* model fits the 295 K data well without the need to add a secondary monoclinic phase. Small asymmetry in some reflections such as the (0 0 4) and (2 0 4) were observed but the *I*4/*m* model still fits well.

Table 2.1: Structural information for Sr_2ZnReO_6. For the *I*4/*m* structure, the Zn^{2+} ions occupy the special position 2a (0 0 0) and Re^{6+} ions occupy the special position 2b (1/2 1/2 0). For the $P2_1/n$ structure, the Zn^{2+} occupy the special position 2c (0 1/2 0) and Re^{2+} occupy the special position 2d (1/2 0 0). Starting point for atomic positions were generated from SPuDS.

	295 K (PXRD)	295 K (SXRD)	295 K (SXRD two tetragonal phase fit)		90 K (SXRD)
R_{wp}	12.375 %	17.281 %	12.321 %		12.087 %
Space group	*I*4/*m*	*I*4/*m*	*I*4/*m*		$P2_1/n$
Weight percent	---	---	59.0(2)	40.9(2)	
a (Å)	5.57608(2)	5.575715(9)	5.57512(1)	5.57885(4)	5.617288(7)
b (Å)	5.57608(2)	5.575715(9)	5.57512(1)	5.57885(4)	5.581906(8)
c (Å)	8.00270(4)	8.00280(2)	8.00393(2)	7.99365(8)	7.89585(1)
β (°)	---	---	---	---	90.0312(2)
V ($Å^3$)	248.826(2)	248.796(1)	248.778(1)	248.790(5)	247.576(1)
Atomic positions					
Sr *x* *y* *z*	0 0.5 0.25	0 0.5 0.25	0 0.5 0.25		0.5018(2) 0.51440(6) 0.25027(6)
O1 *x* *y* *z*	0 0 0.2581(9)	0 0 0.2580(4)	0 0 0.2581(3)		0.2375(7) 0.2200(7) -0.022(1)
O2 *x* *y* *z*	0.221(1) 0.290(1) 0	0.2244(6) 0.2902(6) 0	0.2225(4) 0.2911(4) 0		0.2812(7) 0.7340(7) -0.024(1)
O3 *x* *y* *z*	---	---	---		0.4505(6) -0.0049(6) 0.2423(5)
B_{iso} ($Å^2$)					
Sr	0.67(2)	0.394(7)	0.396(5)		0.188(4)
Zn	0.12(4)	0.01(1)	0.01(1)		0.001(7)
Re	0.29(2)	0.089(5)	0.092(4)		0.114(3)
O1	1.8(2)	1.28(7)	0.97(5)		0.6(1)
O2	1.5(2)	0.80(6)	0.87(5)		0.7(1)
O3	---	---			0.64(7)
Bond distances					
Zn–O (Å)	2.037(8) ×4 2.066(7) ×2	2.045(3) ×4 2.064(4) ×2	2.043(2) ×4 2.066(2) ×2	2.044(2) ×4 2.063(2) ×2	2.054(4) ×2 2.058(4) ×2 2.062(4) ×2
Two Re–O (Å)	1.944(7) ×4 1.936(7) ×2	1.931(3) ×4 1.937(4) ×2	1.936(2) ×6	1.934(2) ×2 1.938(2) ×4	1.927(4) ×2 1.933(4) ×2 1.937(4) ×2

Room temperature PXRD pattern of Sr_2LiOsO_6 was fitted to the tetragonal *I*4/*m* space group. The compound has a similar octahedral tilting scheme $a^0a^0c^-$ to the Sr_2ZnReO_6 compound. The lattice parameters are a = 5.52114(5) Å and c = 7.98571(9) Å. Initial lattice parameters and atomic positions were taken from SPuDS and refined to final values recorded in Table 2.2. Antisite disorder of the Li^+ and Os^{7+} was modeled with occupancy of 0.980(2), which drops the R_{wp} from 15.689 % to 15.597 % which is not a large improvement. Complete ordering is expected for the large size difference (0.76 Å and 0.525 Å, respectively) and charge (1+ and 7+, respectively) difference. The site occupancy was then fixed to unity. There are uncompensated intensity and peak asymmetry that cannot be fit by the *I*4/*m* model. Refinement was done with the monoclinic space group $P2_1/n$ which is a common low symmetry space group observed in double perovskites with ordering at the octahedral site. The R_{wp} is 15.568 % which is not significantly improved from the tetragonal model. Since there are no additional peak splitting that would suggest a lower symmetry, the *I*4/*m* space group was assigned to this compound which is expected for a calculated tolerance factor of 0.983 which is < 1 for an ideal cubic double perovskite. Sr_2LiOsO_6 has been reported as both cubic $Fm\bar{3}m$ by Choy et al. and tetragonal *I*4/*m* by Feng et al. [33,34] The main difference between these two reports is the synthetic procedure. While Choy et al approached the synthesis by solid state method in air for 30 minutes, Feng et al. synthesized the compound under a high pressure of 6 GPa and high temperature of 1500 °C for 1 hour. In addition, the PXRD data from Choy et al showed visible peak asymmetry which might be resolved as tetragonal splitting in a higher resolution powder diffractometer. The lattice parameters from the sample in this chapter are comparable to

the report from Feng et al with the lattice parameters of a = 5.5237(3) Å and c = 7.9930(4) Å.

Synchrotron data at 295 K of Sr_2LiOsO_6 was fitted to the tetragonal $I4/m$ space group with an R_{wp} of 7.420. This is consistent with laboratory data. No peak splitting was observed that would indicate monoclinic symmetry. Attempts to fit the asymmetry of the reflections with microstrain or anisotropic broadening did not improve the refinement. The pattern was also fitted to the monoclinic space group $P2_1/n$ but the model did not significantly improve the refinement. The Os–O bond distances are close to each other within error. Neutron diffraction data at low temperature is currently in progress where the sensitivity of neutron to lighter elements like oxygen might result in more reliable structural refinement.

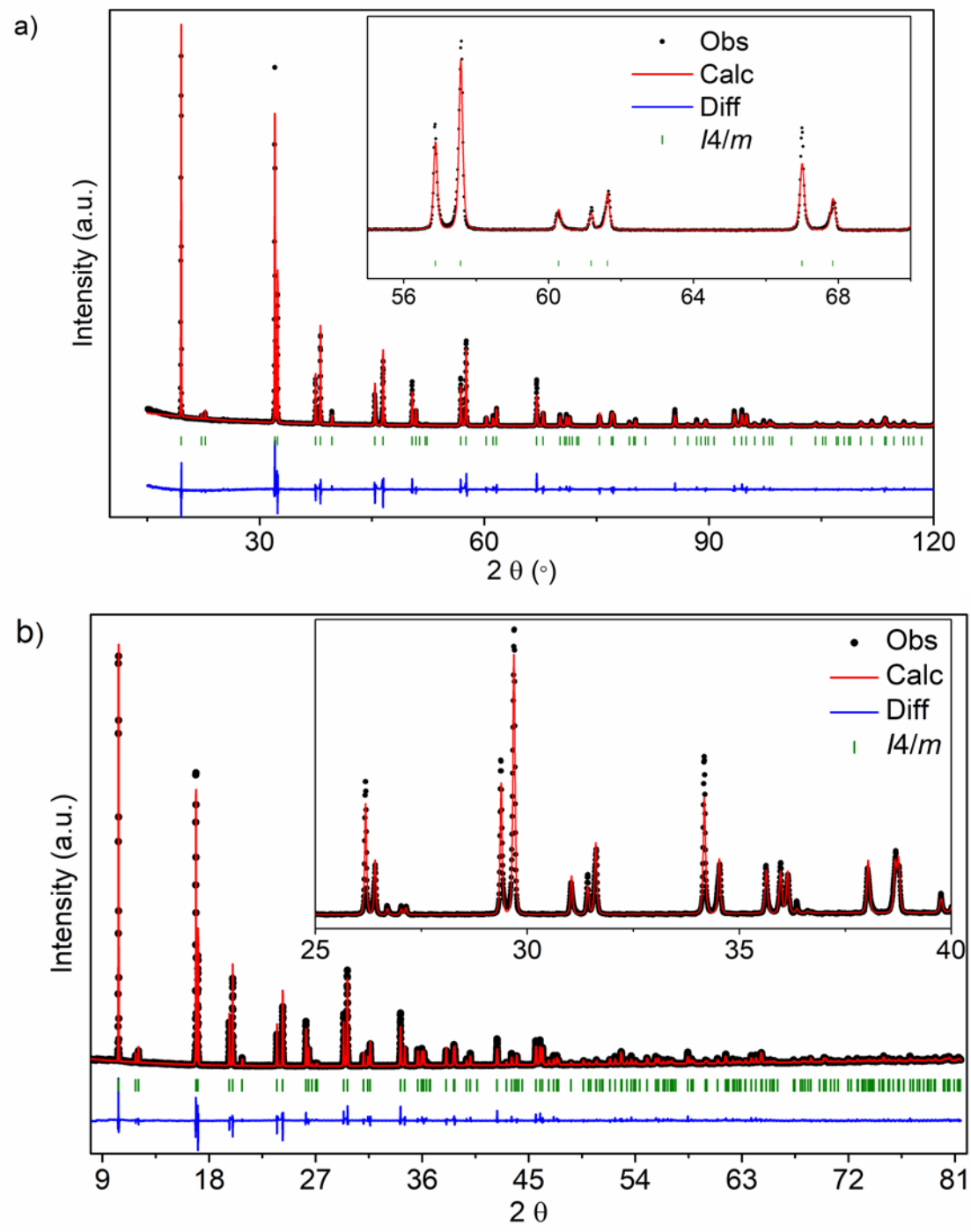

Figure 2.7: a) Room temperature PXRD data of Sr_2LiOsO_6 fitted to the tetragonal *I*4/*m* space group, b) SXRD of Sr_2LiOsO_6 fitted to the tetragonal *I*4/*m* space group.

Table 2.2: Structural information for Sr_2LiOsO_6. For the *I*4/*m* structure, the Li^+ occupy the special position 2a (0 0 0) and Os^{7+} occupy the special position 2b (1/2 1/2 0). The Sr^{2+} occupy the 4d (0, 1/2, 1/4) position. Starting point for atomic positions were generated from SPuDS. Distances are in angstrom, and volume is in cubic angstrom.

Temperature	295 K (PXRD)	295 K (SXRD)
R_{wp}	15.623 %	7.420 %
Space group	*I*4/*m*	*I*4/*m*
Weight percent	---	---
a (Å)	5.52114(5)	5.52746(4)
b (Å)	5.52114(5)	5.52746(4)
c (Å)	7.98572(9)	7.97506(6)
V (Å^3)	243.429(5)	243.661(4)
Atomic positions		
O1 *x* *y* *z*	0 0 0.258(1)	0 0 0.2632(8)
O2 *x* *y* *z*	0.26(2) 0.25(2) 0	0.288(2) 0.235(2) 0
B_{iso} (Å^2)		
Sr	0.49(7)	0.01(4)
Li	1(1)	0.1(7)
Os	0.39(4)	0.01(2)
O1	3.3(4)	1.5(2)
O2	2.9(4)	1.1(2)
Bond distances		
Li–O (Å)	2.0(1) ×4 2.06(1) ×2	2.054(9) ×4 2.099(7) ×2
Os–O (Å)	1.9(1) ×4 1.93(1) ×2	1.877(8) ×4 1.888(7) ×2

Room temperature PXRD pattern of Sr_2NaOsO_6 was fitted to the monoclinic $P2_1/n$ space group which is expected for a tolerance factor of 0.924. The octahedral tilting scheme for this structure is described by the Glazer notation of $a^-a^-c^+$. The refined lattice parameters are a = 5.71139(7) Å, b = 5.80322(7) Å, c = 8.0928(1) Å, and β = 90.022(5)°. Similar to other refinements, initial lattice parameter values and atomic positions were taken from SPuDS, although greater care in refining one parameter at a time was taken for this compound due to its low symmetry. Anti-site disorder of the Na^+ and Os^{7+} sites was modeled for the data, which results in unrealistic negative values for the occupancy and no significant improvement in the refinement (R_{wp} stays the same). As a result, the occupancy of Na and Os was fixed to unity. Ordering at the octahedral site is expected because of the size difference (1.02 Å and 0.525 Å) and charge (1+ and 7+) difference between Na^+ and Os^{7+}.

Synchrotron data at 295 K collected on the BXDS-WLE at the Canadian Light Source was fitted to the monoclinic space group $P2_1/n$ space group. The refined lattice parameters are a = 5.71446(3) Å, b = 5.80102(4) Å, c = 8.09795(5) Å, and β = 89.977(2) ° which are similar to the values from laboratory X-ray. The 90 K SXRD data was also fitted to the monoclinic space group with lattice parameters a = 5.69508(5) Å, b = 5.81897(6) Å, c = 8.06177(9) Å, and β = 90.104(1) °. The background at higher 2θ has high curvature that makes the refinement of low intensity reflections unreliable. As a result, one of the Os–O bond distances (1.97(1) Å) is unreasonably long for a Os^{7+}-O bond. A soft constraint was applied with Os-O bond length of 1.888 Å, which was taken from the single crystal work in the literature.[35] The Os–O bond distance that was previously too long

lengthened further to 2.20 Å with this soft constraint applied, which is more unreasonable than the previous value. The B_{iso} was then allowed to be refined separately for each oxygen, which results in more reasonable bond distances of 1.870(9) Å ×2, 1.886(8) Å ×2, 1.91(1) Å ×2. Although the precision in bond distances is better in the synchrotron data than the laboratory data, the values are not precise enough to conclude definitively how close the OsO_3 environment is to cubic symmetry. Low temperature neutron diffraction data is currently in progress in order to obtain more reliable bond distances.

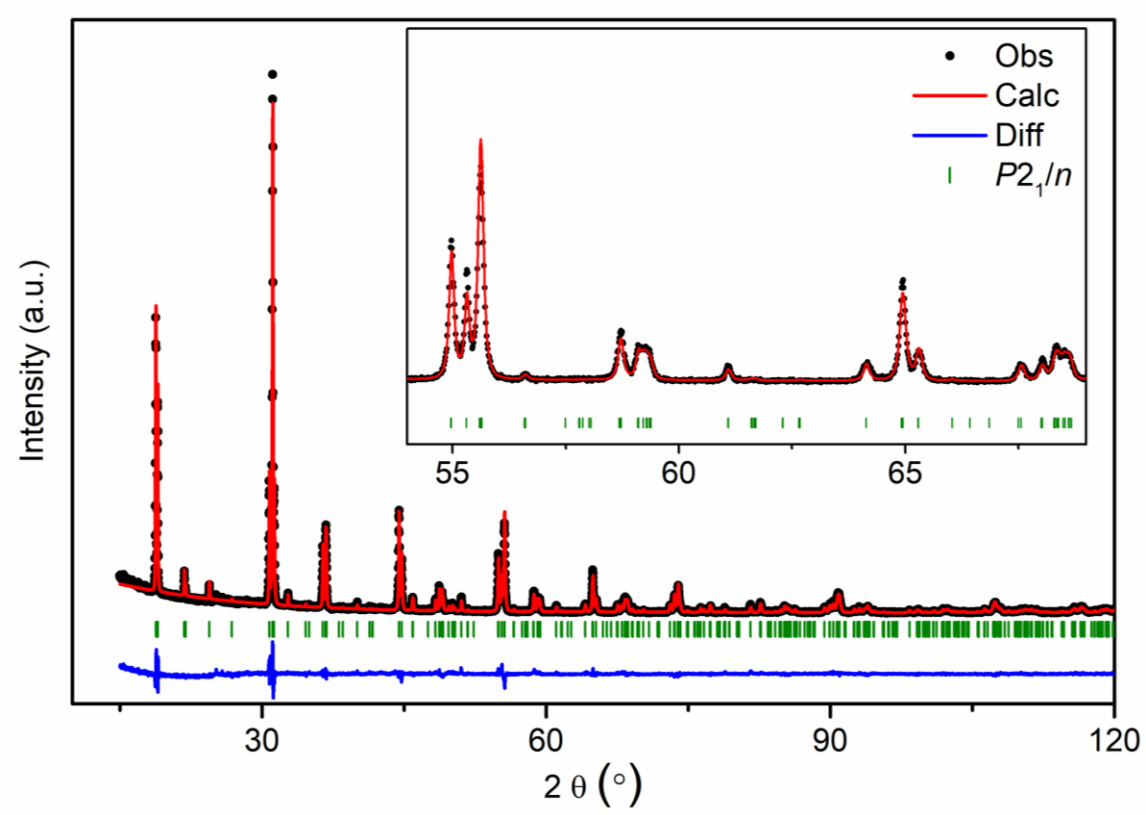

Figure 2.8: Room temperature PXRD of Sr_2NaOsO_6.

Table 2.3: Structural information for Sr_2NaOsO_6 at room temperature taken from the refinement of room temperature laboratory X-ray diffraction data. For the $P2_1/n$ structure, the Na^+ occupy the special position 2c (0 1/2 0) and Os^{7+} occupy the special position 2d (1/2 0 0).

Temperature	295 K PXRD	295 K SXRD
R_{wp}	10.902 %	4.347 %
R_p	8.875 %	3.118 %
Space group	$P2_1/n$	$P2_1/n$
a (Å)	5.71139(7)	5.71447(3)
b (Å)	5.80322(7)	5.80102(3)
c (Å)	8.0928(1)	8.09796(4)
β (°)	90.022(5)	89.977(2)
V (Å^3)	268.233(6)	268.445(2)
Atomic positions		
Sr *x*	0.492(1)	0.5068(8)
y	0.5414(3)	0.5404(2)
z	0.2511(3)	0.2522(1)
O1 *x*	0.233(3)	0.234(1)
y	0.156(3)	0.194(1)
z	-0.041(4)	-0.021(2)
O2 *x*	0.277(3)	0.296(1)
y	0.736(3)	0.742(1)
z	-0.043(4)	-0.042(1)
O3 *x*	0.406(3)	0.418(1)
y	-0.009(3)	-0.027(1)
z	0.238(2)	0.2302(8)
B_{iso} (Å^2)		
Sr	0.92(5)	0.86(2)
Na	0.01(3)	0.01(7)
Os	0.01(3)	0.04(1)
O1	3.5(3)	0.4(2)
O2	3.5(3)	0.4(2)
O3	3.5(3)	0.4(2)
Bond distances (Å)		
Na–O	2.122(19) ×2 2.189(18) ×2 2.421(19) ×2	2.226(7) ×2 2.227(7) ×2 2.240(6) ×2
Os–O	1.81(2) ×2 1.99(2) ×2 2.02(2) ×2	1.901(7) ×2 1.925(7) ×2 1.928(6) ×2

2.3.2 Investigating the magnetic properties

The temperature dependent magnetic susceptibility data for Sr_2ZnReO_6 suggest a ferromagnetic ground state. As the temperature was lowered to 20 K, the field-cooled magnetic susceptibility rises sharply and then flattens out, which is a behavior consistent with ferromagnetism. It is important to note that the inverse magnetic susceptibility is nonlinear from 300 K to 400 K. The gelatin sample capsule can melt or deform in the temperature range 323 K to 400 K which can move the sample off position in the measurement range, resulting in unreliable measurement. As a result, the magnetic susceptibility data from 300 K to 400 K were not included in the analysis. A linear Curie-Weiss function was fitted to the inverse magnetic susceptibility data from 100 K to 300 K with the diamagnetic correction from the core electron substracted. This yields an effective moment of 0.791(3) μ_B and a Weiss temperature of 27.4(8) K. The positive Weiss temperature indicates a ferromagnetic ground state. In $5d^1$ compounds the magnetic moment is significantly reduced due to spin-orbit coupling, and because of the small size of the moment subtracting the temperature independent contribution of the magnetism from defects is important. Above the magnetic ordering temperature, the sample is paramagnetic and thus follow the Curie-Weiss law at high temperature. To determine the size of the temperature independent correction, the magnetic susceptibility data was fitted to the equation

$$\chi = \frac{C}{(T - \theta)} + \chi_0$$

where χ is magnetic susceptibility, T is temperature, C is the Curie constant, θ is the Weiss constant, and χ_0 is the temperature independent correction. The χ_0 of $4.4(6)\times10^{-5}$ emu mol^{-1} Oe^{-1} was determined from iteratively fitting the magnetic susceptibility data from 100 K to 300 K to yield values that best fit the data. The temperature independent correction was subtracted from the data. This yields an effective moment of 0.716(9) μ_B and a Weiss temperature of 41.4(7) K. In addition, the isothermal magnetization at 2 K shows hysteretic behavior that is consistent with ferromagnetism. The saturated moment at 2 K is 0.13 μ_B /f.u. (formula unit).

Temperature dependent magnetic susceptibility of Sr_2LiOsO_6 shows an antiferromagnetic-like cusp at 15 K. In addition, the isothermal magnetization as a function of applied field taken at 2 K is linear, which is consistent with an antiferromagnetic ground state. However, specific heat measurement is necessary to confirm whether the ground state is antiferromagnetic or spin glass. A correction for diamagnetic contribution from the core electrons calculated from Pascal's constants was subtracted from the magnetic susceptibility data.[36] Typical Curie-Weiss analysis is unreliable due to the large degree of deviation from typical linear Curie-Weiss behavior for paramagnetic behavior above magnetic ordering temperature. A temperature independent correction to account for effects from defects of $4.15(6)\times10^{-4}$ emu mol^{-1} Oe^{-1} was determined from iteratively fitting the magnetic susceptibility data from 100 K to 300 K similar to the approach for Sr_2ZnReO_6. The temperature independent correction was subtracted from the data. This yields an effective moment of 0.789(3) μ_B and a Weiss temperature of −62.1(4) K. The effective moment is similar to the value from the isoelectronic compound Sr_2ZnReO_6. The

inverse magnetic susceptibility with the temperature independent correction follows linear Curie-Weiss behavior at high temperature.

Temperature dependent magnetic susceptibility of Sr_2NaOsO_6 shows a ferromagnetic-like sharp rise in the magnetic susceptibility starting at 20 K. Similar to the other $5d^1$ compounds, the Curie-Weiss fit is not reliable due to the nonlinearity of the inverse magnetic susceptibility. The temperature independent correction χ_0 of $5.2(6)\times10^{-4}$ emu mol^{-1} Oe^{-1} was determined from iteratively fitting the magnetic susceptibility data from 100 K to 300 K. Similar to the analysis with the isoelectronic compound Sr_2ZnReO_6 and Sr_2LiOsO_6, the temperature independent correction was subtracted from the data which yields am effective moment of 0.71(3) μ_B and a Weiss temperature of −34(4) K. The negative Weiss constant indicates some antiferromagnetic interactions are present. However, the ferromagnetic-like sharp rise in the magnetic susceptibility data and the isothermal magnetization as a function of applied field taken at 2 K shows a hysteresis consistent with ferromagnetic ground state. The saturated moment is 0.08 μ_B/f.u. which is lower than the 0.13 μ_B/f.u. from isoelectronic Sr_2ZnReO_6.

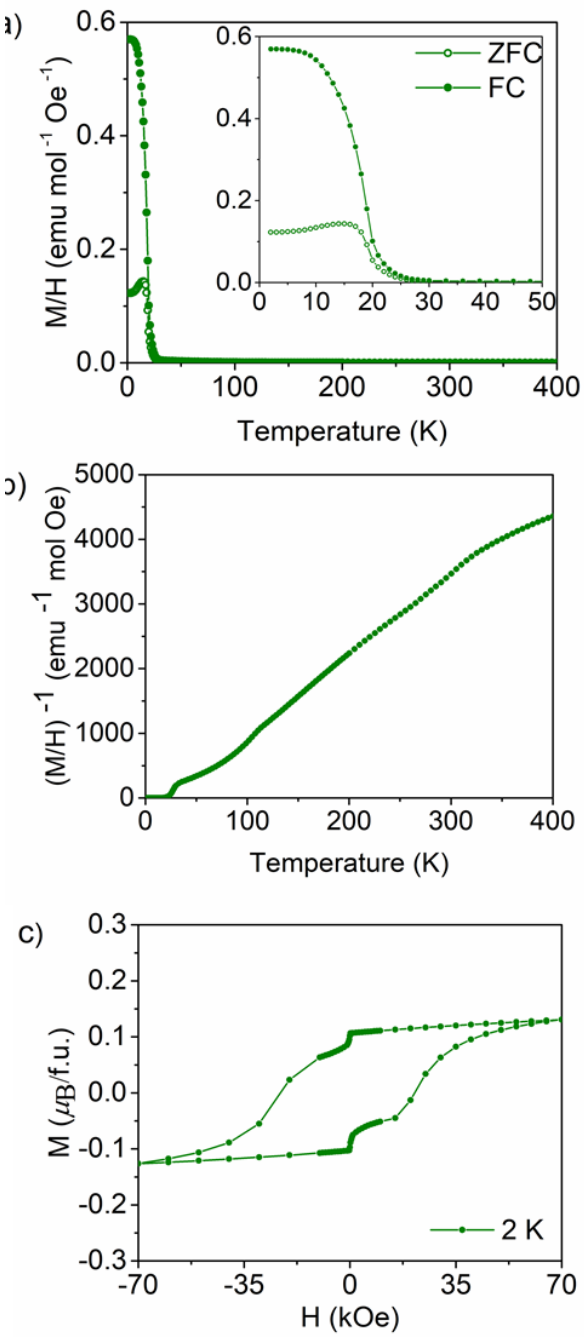

Figure 2.9: a) The magnetic susceptibility as a function of temperature for Sr_2ZnReO_6 at 1000 Oe, b) the inverse susceptibility, and c) isothermal magnetization at 2 K.

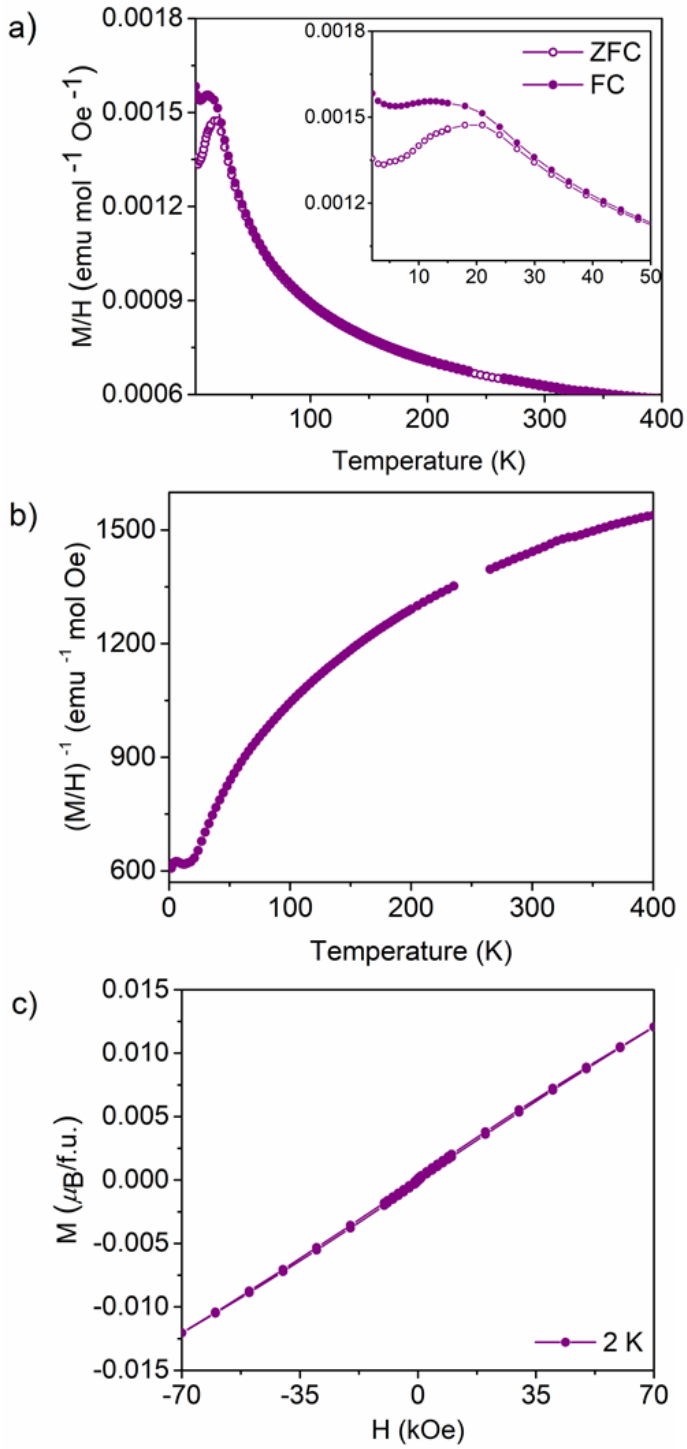

Figure 2.10: a) The magnetic susceptibility as a function of temperature for Sr_2LiOsO_6 at 1000 Oe, b) the inverse susceptibility, and c) isothermal magnetization at 2 K.

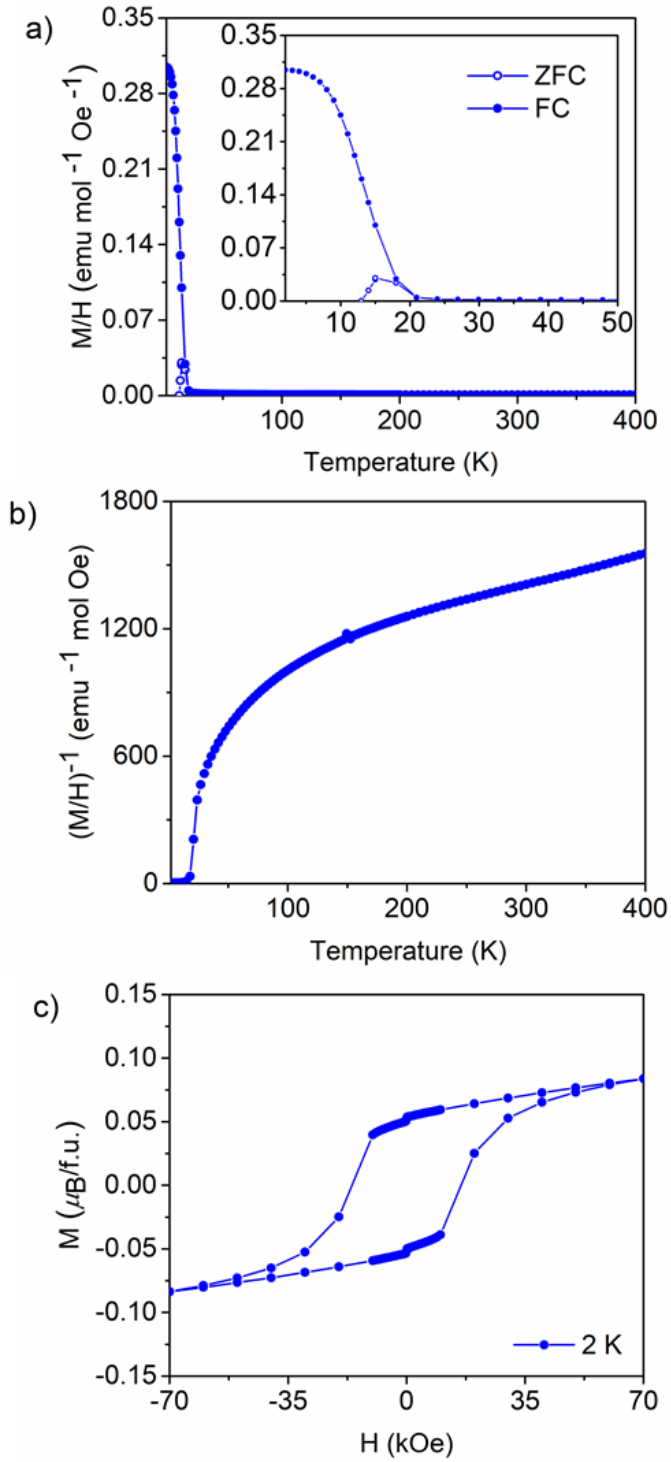

Figure 2.11: a) The magnetic susceptibility as a function of temperature for Sr_2NaOsO_6 at 1000 Oe, b) the inverse susceptibility, and c) isothermal magnetization at 2 K.

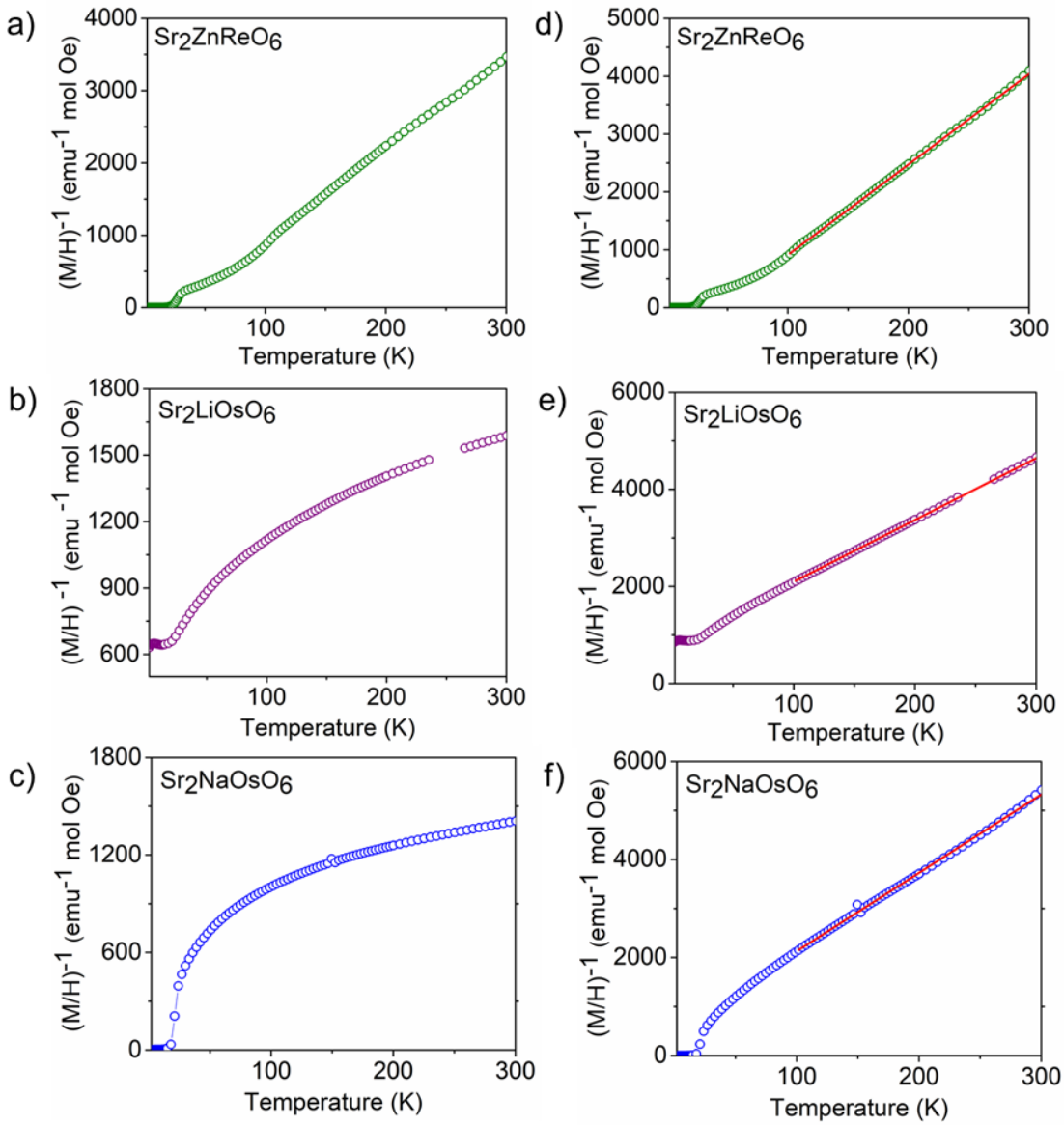

Figure 2.12: Inverse magnetic susceptibility as a function of temperature with correction for the core electron (left) and with temperature independent correction (right).

2.4 Discussion

Table 2.4: Calculated tolerance factor of Sr_2ZnReO_6, Sr_2LiOsO_6, and Sr_2NaOsO_6.

Compound	Tolerance factor	Space group 295 K	Space group 90 K	Magnetic ground state
Sr_2ZnReO_6	0.982	*I*4/*m*	$P2_1/n$	FM
Sr_2LiOsO_6	0.983	*I*4/*m*	*I*4/*m*	AFM or spin glass
Sr_2NaOsO_6	0.924	$P2_1/n$	$P2_1/n$	FM

The *I*4/*m* room temperature structure for Sr_2ZnReO_6 is expected given that the Goldschmidt tolerance factor for this compound calculated from Shannon ionic radii is 0.982 which is smaller than the 1.041 value for cubic Ba_2ZnReO_6. The bond lengths for Re–O are 1.931(3) Å in the *ab* plane and 1.937(4) Å along the *c* direction, which indicates a subtle elongation of the ReO_6 octahedra, although they are essentially the same within error. The bond lengths are longer than the 1.90 expected from ionic radii. [37] However, they are close to reported values in literature for Re–O bonds with Re^{6+} in isoelectronic compounds Ba_2ZnReO_6, Ba_2MgReO_6, and Sr_2MgReO_6.[38,39] The elongation of the ReO_6 octahedra was observed previously in Sr_2ZnReO_6 and Sr_2MgReO_6 for data collected at room temperature. [31,40] At 90 K the structure of Sr_2ZnReO_6 becomes monoclinic $P2_1/n$, although the bond distances are still close to each other within experimental error. Despite the distortion, a ferromagnetic ground state is observed like the cubic analog Ba_2ZnReO_6.

The compound Sr_2LiOsO_6 which has a similar tolerance factor of 0.983 to the Sr_2ZnReO_6 compound also has the tetragonal *I*4/*m* structure. This is expected with a lower tolerance factor than the cubic Ba_2LiOsO_6 with the tolerance factor of 1.042. At room temperature, the Os–O bonds on the *ab* plane is 1.877(8) Å and the bonds along the *c* direction is 1.888(7) Å which indicates an elongation of the OsO_3 octahedra. Despite the

similar tolerance factor with Sr_2ZnReO_6, Sr_2LiOsO_6 is tetragonal at 90 K. Neutron diffraction data collection is currently in the works for bond distances with higher precision. Interestingly, the magnetic behavior of Sr_2LiOsO_6 suggests that elongation of the octahedra results in an antiferromagnetic or a spin glass ground state.

Unlike Sr_2ZnReO_6 and Sr_2LiOsO_6, Sr_2NaOsO_6 has a monoclinic $P2_1/n$ structure at room temperature, which is expected for a smaller tolerance factor of 0.924. At room temperature, the bond distances from SXRD are 2×1.901(7) Å, 2×1.925(7) Å, and 2×1.928(6) Å. At 90 K, the bond distances from SXRD are 2×1.871(9) Å, 2×1.886(8) Å, and 2×1.908(9) Å. The Os–O bond distances at low temperature indicates small orthorhombic distortion of the octahedra. The behavior of the ferromagnetic Sr_2NaOsO_6 is similar to the monoclinic Sr_2ZnReO_6.

The magnetic properties of these $5d^1$ double perovskites indicates that orthorhombic distortions can stabilize a ferromagnetic ground state while tetragonal distortions can stabilize antiferromagnetic or spin glass ground state. From our work, Sr_2ZnReO_6 and Sr_2NaOsO_6 crystallize in the same monoclinic $P2_1/n$ space group at low temperature with ferromagnetic magnetic ground states. However, Sr_2LiOsO_6 which has similar tolerance factor to Sr_2ZnReO_6 crystallizes in tetragonal $I4/m$ space group with antiferromagnetic ground state. Interestingly, NMR work done on Ba_2NaOsO_6 indicates that orthorhombic distortion occurs in the single crystal sample above the ferromagnetic transition temperature. The Na NMR peak splits into two below 11 K and two sets of three peaks below 10 K. The orthorhombic distortion is associated with the stabilization of a canted ferromagnetic ground state. [41,42] This signature of lowering of symmetry has been associated with orbital ordering, where the electron occupation of the d_{xy}, d_{yz}, and d_{xy}

orbitals are not degenerate.[43] In our ferromagnetic monoclinic Sr_2ZnReO_6 and Sr_2NaOsO_6 compounds, the monoclinic structural distortions split the degeneracy of the three crystallographic directions, which can possibly results in nondegenerate t_{2g} orbital occupation, although it is not clear what the pattern of orbital ordering would be if it exists. Further experimental evidence is necessary in order to fully elucidate the factors that stabilize different magnetic ground states.

Table 2.5: List of $5d^1$ double perovskites.

	Tolerance factor	Space group*	B′ – O dist. (Å)	Ground state†	Ref
Ba_2MgReO_6	1.054	$Fm\bar{3}m$ $T = 3.5$ K	1.926	FM $T_C = 18$ K	38
Ba_2ZnReO_6	1.049	$Fm\bar{3}m$ $T = 90$ K	1.906	FM $T_C = 16$ K	38
Ba_2LiOsO_6	1.050	$Fm\bar{3}m$ $T = 300$ K	1.888	AFM $T_N = 8$ K	35,44
Ba_2NaOsO_6	0.986	$Fm\bar{3}m$ $T = 300$ K	1.870	FM $T_C = 7$ K	35
Ba_2CdReO_6	0.997	$I4/m$ $T = 90$ K	1.923×4 1.904×2	AFM $T_N = 4$ K	45
Ba_2CaReO_6	0.985	$I4/m$ $T = 17$ K	1.964×4 1.935×2	AFM $T_N = 15$ K	46
Sr_2MgReO_6	0.994	$I4/m$ $T = 6$ K	1.882×4 1.929×2	Spin glass $T_g = 45$ K	40
Sr_2ZnReO_6	0.982	$P2_1/n$ $T = 90$ K	1.927 ×2 1.933 ×2 1.937 ×2	FM $T_C = 17$ K	This work
Sr_2LiOsO_6	0.983	$I4/m$ $T = 300$ K	1.912 ×4 1.929 ×2	AFM $T_N = 15$ K	This work
Sr_2CaReO_6	0.928	$P2_1/n$ $T = 4$ K	1.907×2 1.921×2 1.904×2	Spin glass $T_g = 14$ K	39
Sr_2NaOsO_6	0.924	$P2_1/n$ $T = 300$ K	1.871 ×2 1.886 ×2 1.908 ×2	FM $T_C = 13$ K	This work

2.5 Conclusion

The double perovskites Sr_2ZnReO_6, Sr_2LiOsO_6, and Sr_2NaOsO_6 were synthesized by the solid state method, and the structural and magnetic properties were characterized. Synchrotron diffraction data on Sr_2ZnReO_6 indicates that the compound undergoes a

tetragonal $I4/m$ to monoclinic $P2_1/n$ phase transition. Synchrotron diffraction data also indicates that Sr_2LiOsO_6 crystallizes in the tetragonal $I4/m$ space group while Sr_2NaOsO_6 crystallizes in the monoclinic $P2_1/n$ space group. Both the monoclinic Sr_2ZnReO_6 and Sr_2NaOsO_6 compounds are ferromagnetic, while the tetragonal Sr_2LiOsO_6 is antiferromagnetic or spin glass. This indicates that the $5d^1$ magnetism has a complex relationship with crystal structure, where different $5d^1$ octahedra distortions yields different magnetic ground states.

Chapter 3 Structure and Magnetic Properties of Solid Solution $Ba_2Na_xCa_{1-x}OsO_6$

3.1 Introduction

The magnetic ground state of $5d^1$ double perovskites is stabilized by a balance between spin, charge, and orbital degrees of freedom. In this chapter, the effect of the charge degree of freedom on the magnetism is explored. Ba_2NaOsO_6 is a $5d^1$ cubic double perovskite with the ferromagnetic transition at 8 K. Ba_2CaOsO_6 is a $5d^2$ cubic double perovskite with an antiferromagnetic transition at 50 K. Both of these systems are cubic with lattice parameters that are within ~1% of each other (8.2870(3) Å and 8.3619(6) Å, respectively) which suggests the composition $Ba_2Na_xCa_{1-x}OsO_6$ should form a complete solid solution. By substituting the Na^+ site with Ca^{2+}, $5d^2$ Os^{6+} is introduced into the system. This allows for the study of the effect of the magnetic ground state as a function of charge doping.

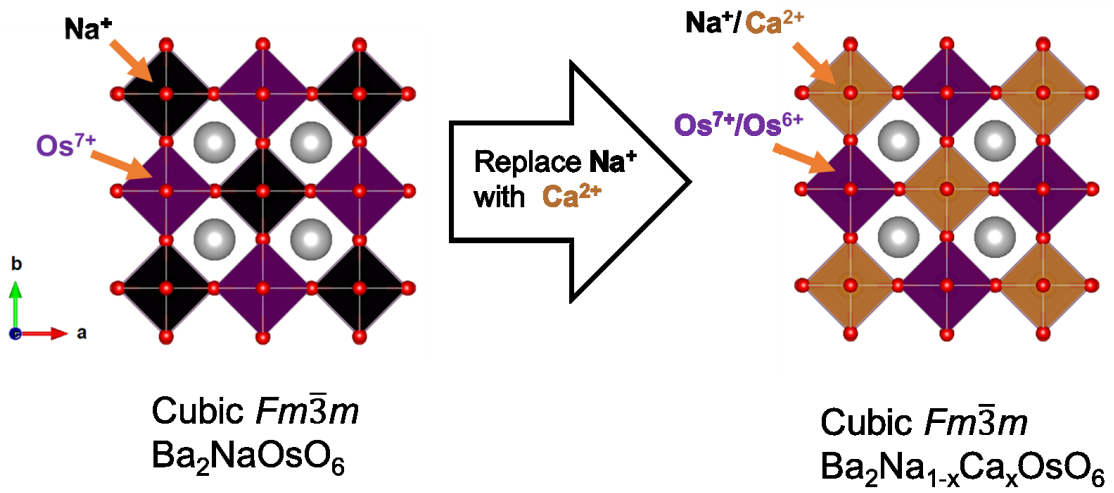

Figure 3.1: Substituting the Na^{+} site with Ca^{2+} to form the composition $Ba_2Na_xCa_{1-x}OsO_6$.

3.2 Experimental

Polycrystalline samples of the $Ba_2Na_xCa_{1-x}OsO_6$ (x = 1, 0.875, 0.75, 0.625, 0.50, 0.25, 0.10, 0) solid solution were synthesized in evacuated quartz tubes. Stoichiometric amounts of BaO (Sigma-Alrich, 99.99 % trace metals basis), CaO (Sigma-Alrich, 99.9 % trace metals basis), Na_2O_2 (Alfa Aesar, 95 %) and Os powder (Sigma-Alrich, 99.9 % trace metals basis) were ground in a mortar and pestle, transferred to an alumina tube, sealed in a quartz tube under vacuum. A separate alumina cap containing PbO_2 was also included in the sealed quartz tube as the decomposition of PbO_2 into PbO and O_2 at 600 °C provided the oxygen source to oxidize Os metal. Because highly toxic OsO_4 can form from the reaction of Os metal and O_2 at 400 °C, this reaction must be carried out inside an evacuated quartz tube with a theoretical product yield of 1 gram to prevent an overpressure of O_2 that ruptures the reaction vessel and release OsO_4. To ensure the full oxidation to Os^{7+}, the reaction was done with an excess of 1/4 mol of oxygen for every mol of product. The

reaction vessel was heated at 1000 °C for 24 hours. Samples with two cubic phases present were reground and heated for an additional 12 hours at 1000 °C.

$2\ BaO + (1/2)\ x\ Na_2O_2 + (1-x)\ CaO + Os + (7/2)\ PbO_2 \rightarrow Ba_2Na_xCa_{1-x}OsO_6 + (7/2)\ PbO + 1/4\ O_2$

Room temperature powder X-ray diffraction data (PXRD) was collected using a Bruker D8 Advance powder diffractometer (40 kV, 40 mA, sealed Cu X-ray tube) equipped with an incident beam monochromator (Johansson type SiO_2 crystal) and a Lynxeye XE-T position sensitive detector. Phase purity and cation ordering were determined by powder Rietveld refinement in TOPAS-Academic (v6).[29] Starting values for atomic positions were generated from SPuDS.[30]

Magnetic susceptibility as a function of temperature (2 K–400 K) was collected for each sample with an applied field of 1000 Oe in zero field cooled (ZFC) and field cooled (FC) conditions using the Superconducting Quantum Interference Device (SQUID). Approximately 100 mg of sample was loaded in a gelatin capsule and mounted in a plastic straw. Magnetization versus applied field data were taken on the same instrument with an applied field of -70 kOe to 70 kOe at 2 K and 300 K for all samples.

3.3 Results

3.3.1 The structure of the $Ba_2Na_xCa_{1-x}OsO_6$ solid solution

The room temperature PXRD data of the $Ba_2Na_xCa_{1-x}OsO_6$ solid solution were fitted with the $Fm\bar{3}m$ space group observed Ba_2NaOsO_6 and Ba_2CaOsO_6. The lattice parameter of the x = 1 sample is 8.28566(5) Å, which is comparable to the value of

8.2870(3) Å reported for single crystal specimens of Ba_2NaOsO_6.[35] The lattice parameter of the x = 0 sample is 8.35780(2) Å, which is slightly smaller than the 8.3619(6) Å reported in literature.[47] With increasing concentration of Ca^{2+}, the lattice parameter increases as expected.

Some samples in the $Ba_2Na_xCa_{1-x}OsO_6$ solid solution series consist of two different cubic phases. The PXRD data of the x = 0.75 and 0.50 samples show a shoulder at every reflections that suggest the presence of a secondary cubic phase. The data for these samples were fitted to two cubic phases, which significantly improves the model and lowers the R_{wp}. The smaller lattice parameter (a1) is likely to have a higher concentration of Na^+, and the larger lattice parameter (a2) is likely to have a higher concentration of Ca^{2+}. However, attempts to refine the occupancy of the Na^+ and Ca^{2+} results in unstable refinement due to the low resolution of the diffractometer and the low X-ray scattering factor of the Na^+. The occupancy was fixed to the composition values. The presence of a secondary cubic phase in these composition suggest that they might be kinetic products. The secondary cubic phase has a larger lattice parameter which suggest a higher concentration of Os^{6+}. The lattice parameter of the secondary cubic phase, 8.3431(2) Å for the x = 0.75 sample and 8.3513(1) Å for the x = 0.50 sample are both smaller than 8.35780(2) Å for the x = 0 sample (Ba_2CaOsO_6). If there is a miscibility of the Ca^{2+} in this solid solution system, one would expect the lattice parameters of the two cubic phases to remain near constant as a function of increasing Ca^{2+} concentration. In addition, the phase percent of each cubic phase would be dependent on the concentration of Ca^{2+}. However, the cubic lattice parameter of the majority cubic phase in the $Ba_2Na_xCa_{1-x}OsO_6$ solid solution system increases linearly with increasing Ca^{2+} concentration, which suggests solubility of the Na^+/ Ca^{2+}. Thus, the small

presence of a secondary cubic phase in the x = 0.75 and 0.50 samples is likely to be an indication that the samples are kinetic products.

Samples with high concentration of Ca^{2+} (x = 0.25–0) contain a secondary phase $Ba_{11}Os_4O_{24}$ which has a ferromagnetic transition at 6 K. The ferromagnetic secondary phase is 3–6 weight percent. The presence of a secondary cubic phase in the $Ba_2Na_xCa_{1-x}OsO_6$ system is possibly due to the difficulty of oxidizing Os metal to Os^{7+} uniformly. The lattice parameter of the majority cubic phase plotted as a function of composition shows a linear increase with increasing concentration of Ca^{2+}.

Table 3.1: Phase composition of the $Ba_2Na_xCa_{1-x}OsO_6$ system from PXRD analysis.

x	Phase 1 wt.%	a1 (Å)	Phase 2 wt.%	a2 (Å)	$Ba_{11}Os_4O_{24}$ wt. %
1	100	8.28566(5)	0	0	0
0.875	100	8.29693(3)	0	0	0
0.75	93.4(3)	8.30452(3)	6.6(3)	8.3431(2)	0
0.625	100	8.31801(4)	0	0	0
0.50	87.3(4)	8.32985(6)	12.6(4)	8.3513(1)	0
0.25	97.0(3)	8.34349(3)	0	0	3.0(3)
0.10	93.7(3)	8.35279(3)	0	0	6.3(3)
0	96.2(3)	8.35780(2)	0	0	3.8(3)

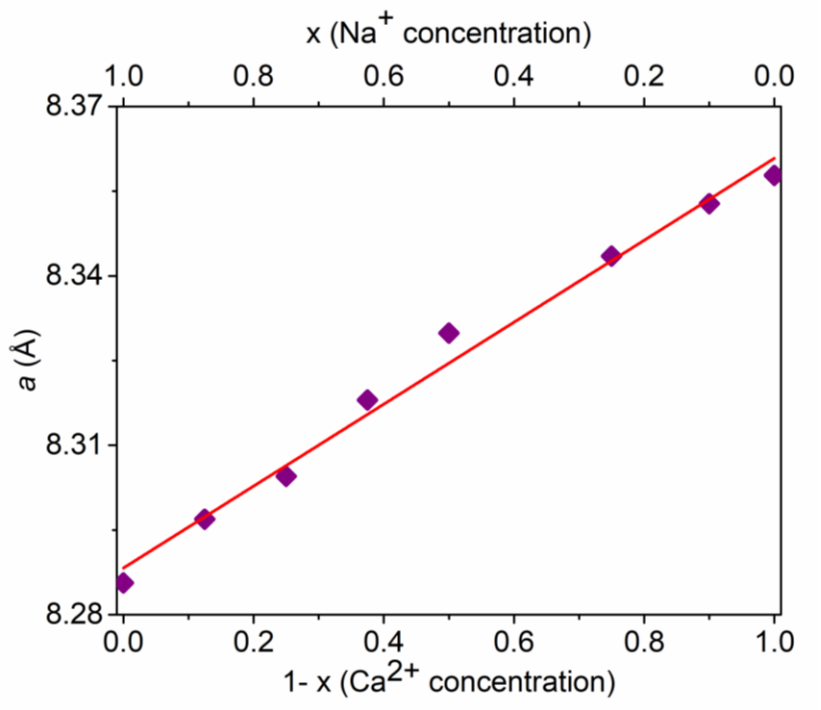

Figure 3.2: Cubic lattice parameter versus concentration of Ca^{2+} (bottom axis) and concentration of Na^{+} (top axis).

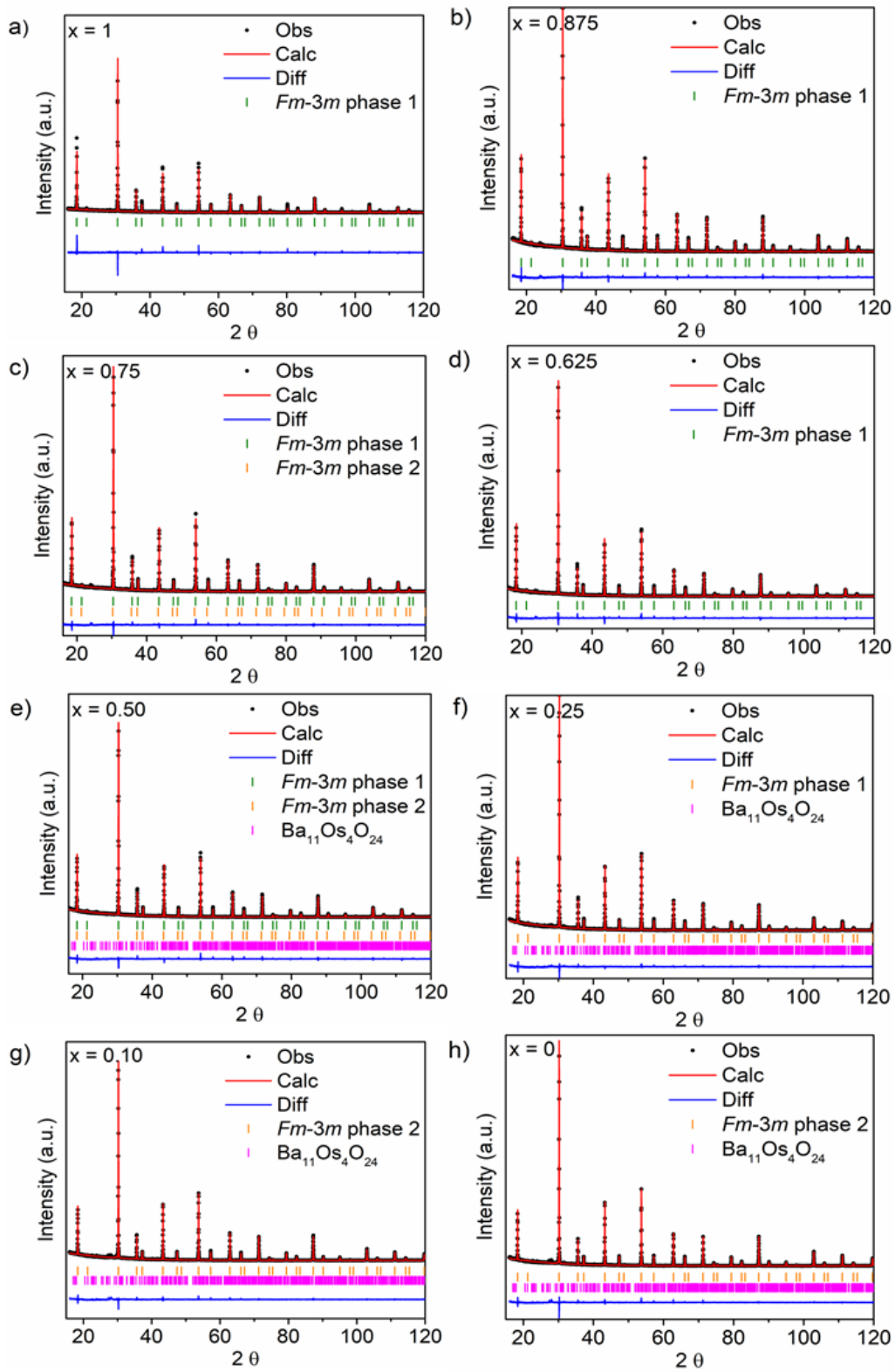

Figure 3.3: Room temperature PXRD of the $Ba_2Na_xCa_{1-x}OsO_6$ solid solution.

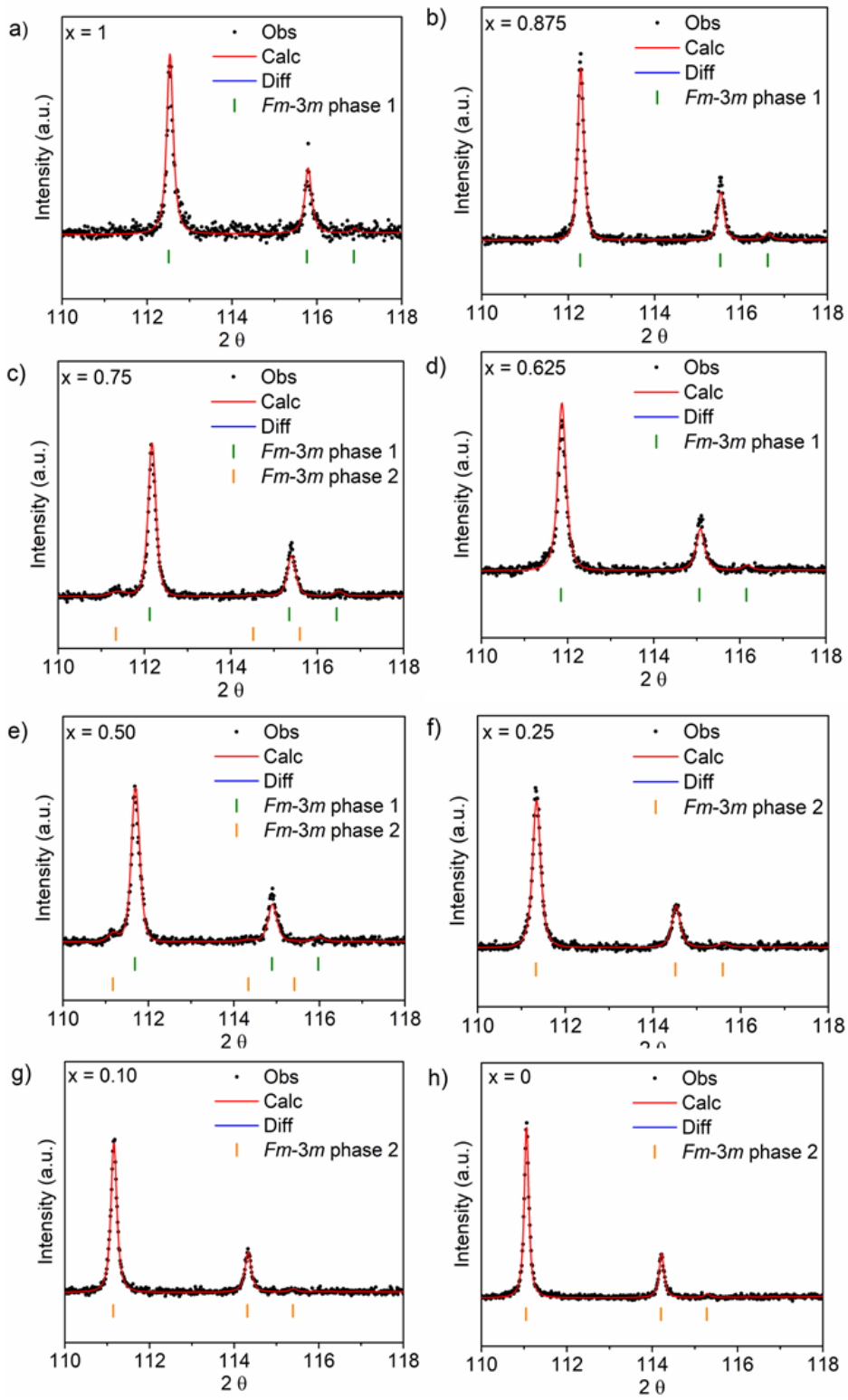

Figure 3.4: Zoom-in region of the PXRD patterns for $Ba_2Na_xCa_{1-x}OsO_6$.

3.3.2 Magnetic susceptibility measurements on the $Ba_2Na_xCa_{1-x}OsO_6$ solid solution

Magnetic susceptibility measurement as a function of temperature for the x = 1 sample shows a ferromagnetic sharp rise in the magnetic susceptibility near 6 K. In addition, isothermal magnetization measurements at 2 K shows a small hysteresis loop that is consistent with ferromagnetism. The single crystal Ba_2NaOsO_6 previously reported has a ferromagnetic transition at 8 K and a saturation magnetization of ~0.15 μ_B/formula unit. [35] Similar to the treatment of the magnetic susceptibility data for the distorted $5d^1$ compounds in chapter 2, the temperature independent contribution of the magnetism from defects is subtracted from the data. To determine the size of the temperature independent correction, the magnetic susceptibility data was fitted to the equation

$$\chi = \frac{C}{(T - \theta)} + \chi_0$$

where χ is magnetic susceptibility, T is temperature, C is the Curie constant, θ is the Weiss constant, and χ_0 is the temperature independent correction. The temperature dependent correction is $1.08(8)\times10^{-4}$ emu mol^{-1} Oe^{-1}, which is in the same order of magnitude for the single crystal values at $3(1)\times10^{-5}$ to1.79×10^{-4} emu mol^{-1} Oe^{-1}. [48] The addition of a temperature dependent correction to the Curie-Weiss analysis was applied to all the samples in the $Ba_2Na_xCa_{1-x}OsO_6$ series.

The Ba_2CaOsO_6 sample has a lower antiferromagnetic transition temperature of 45 K than reported in literature of 50 K. [46,47] The effective moment of 1.47(2) μ_B and the Weiss constant of −132(2) K are both smaller than the reported literature values of 1.640(1) μ_B and 156.2(3) K.[47] The literature report did not use a temperature independent correction which might account for the difference.

As the Ca^{2+} is substituted in the Na^{+} site, the magnetic ground state becomes more antiferromagnetic-like, and the magnetic transition temperature shifts to higher temperature. The x = 0.875 (12.5% Ca^{2+}) sample is mostly antiferromagnetic with the linear isothermal magnetization data at 2 K and significantly smaller magnetic susceptibility by one order of magnitude from the ferromagnetic compound. This suggests that a small amount of Os^{6+} is sufficient in destabilizing the $5d^1$ ferromagnetic ground state. The magnetic ordering temperature was estimated by selecting the temperature at which the field-cooled and zero-field cooled magnetic susceptibility diverges. As the concentration of Ca^{2+} increases, the magnetic transition temperature shifts to higher values and approaches the ~45 K value of the Ba_2CaOsO_6 antiferromagnetic transition. In addition, the inverse magnetic susceptibility as a function of temperature becomes more linear. For all samples in the solid solution except for the x = 1 sample, the inverse magnetic susceptibility data were fitted to the Curie-Weiss law from 100–300 K. The inverse magnetic susceptibility data for all samples were also fitted to the Curie-Weiss law with a temperature independent correction. The effective moment increases with increasing concentration of Ca^{2+} which is consistent with increasing $5d^2$ Os^{6+}. In addition, the Weiss constant decreases to more negative values with increasing concentration of Ca^{2+} which indicates increasing antiferromagnetic interactions.

Isothermal magnetization collected at 2 K for all samples demonstrates the destabilization of the $5d^1$ ferromagnetic ground state with Ca^{2+} substitution as the magnetization becomes more linear with applied field. The isothermal magnetization at 2 K for the x = 0.875–0.5 samples are linear with applied field which is indicates antiferromagnetic behavior. At 2 K, the x = 0–0.25 samples exhibit a soft ferromagnetic like feature where the magnetization as a function of applied field is S shaped and saturated to ~0.06 μ_B/formula unit at 70 kOe. Isothermal magnetization collected at 25 K which is below the 45 K magnetic transition temperature is linear with applied field. The ferromagnetic feature at 2 K for the x = 0–0.25 samples is likely due to the $Ba_{11}Os_4O_{24}$ which is ferromagnetic at 6 K. This is consistent with the 3–6 % $Ba_{11}Os_4O_{24}$ by weight detected in the PXRD data for these three samples.

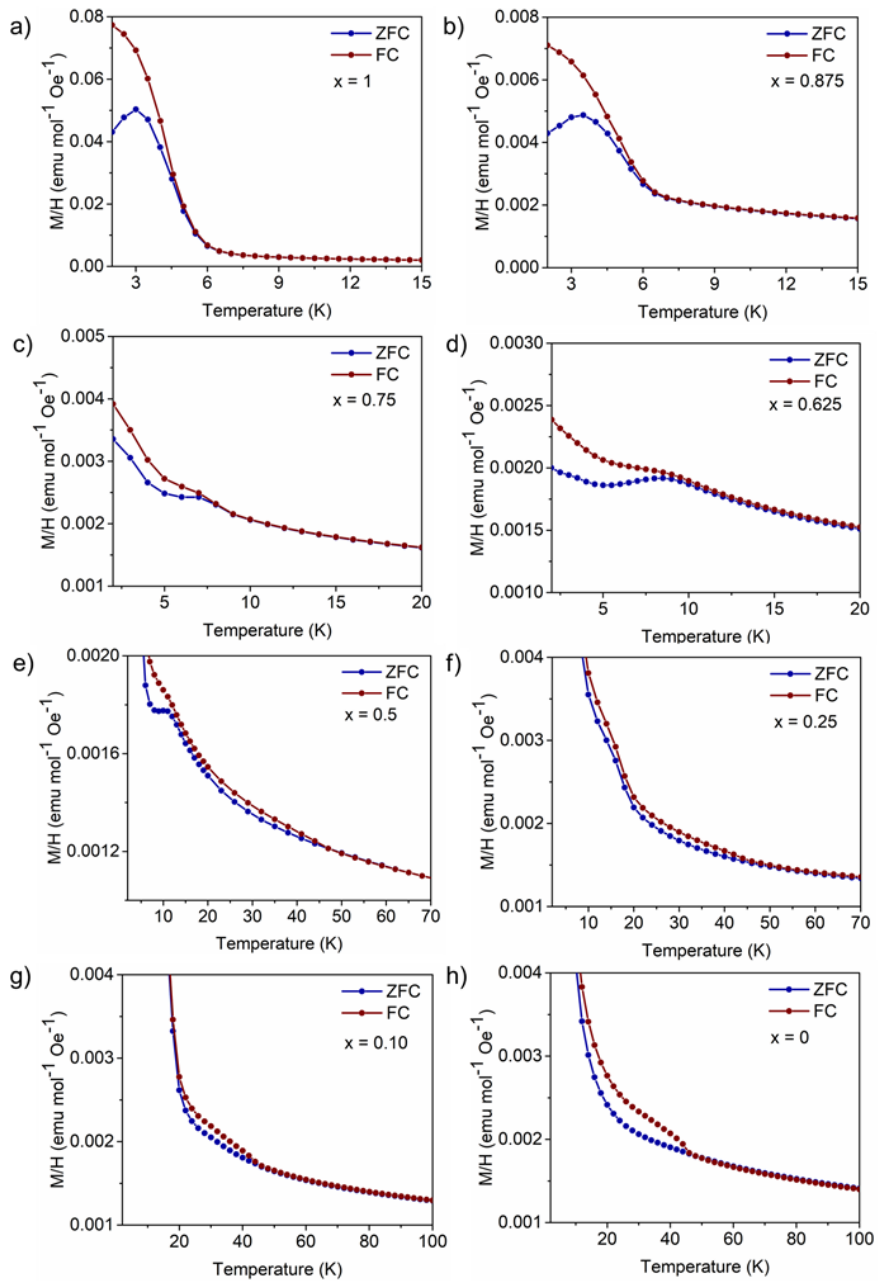

Figure 3.5: Magnetic susceptibility as a function of temperature for x = 0–1 samples. The switch from ferromagnetic to antiferromagnetic ground state occurs between x = 1 and x = 0.875. There is a ferromagnetic impurity in the x = 0–0.25 samples which makes the antiferromagnetic cusp difficult to observe.

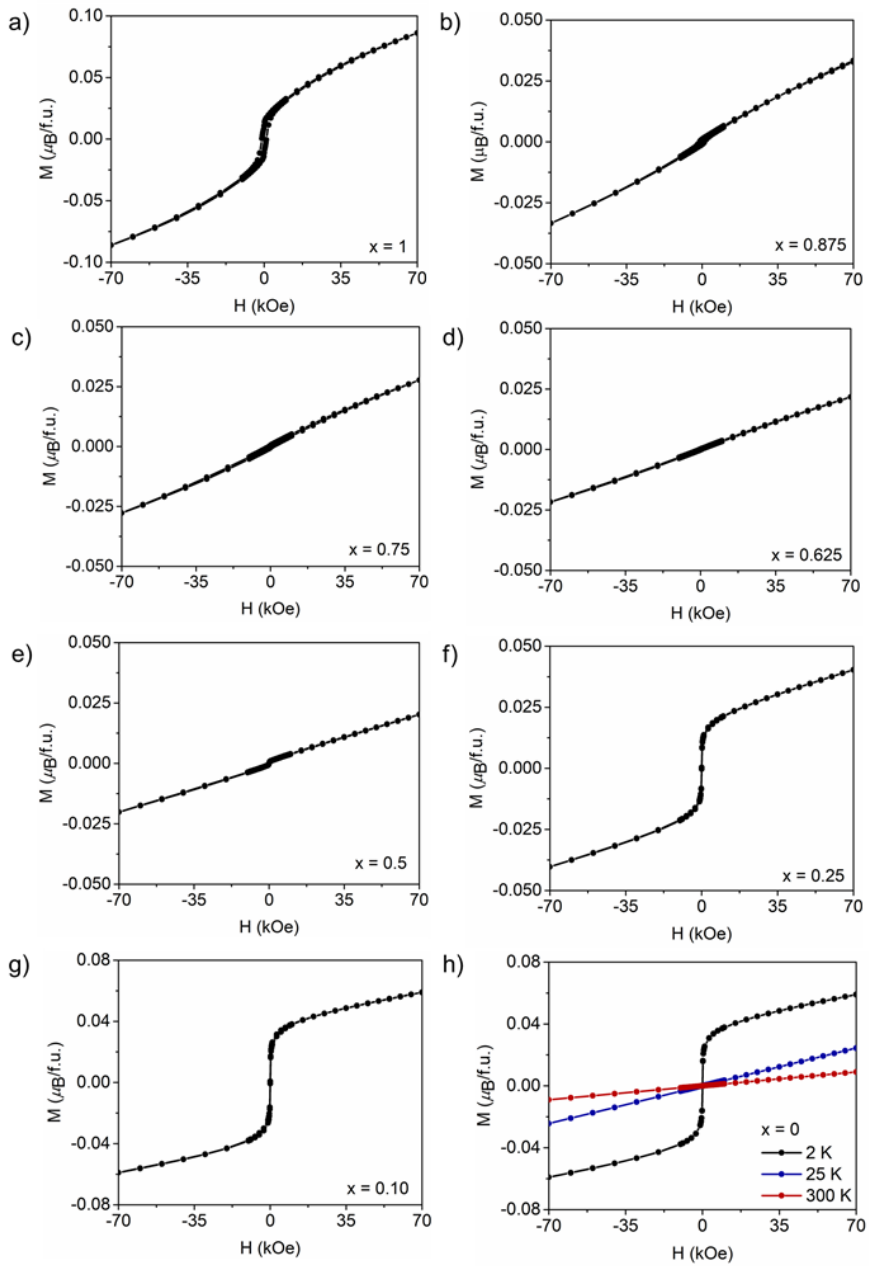

Figure 3.6: Magnetization versus field for the x = 0–1 samples at 2 K. The transition at 45 K for the x = 0 sample is antiferromagnetic as confirmed by the linear magnetization versus field curve at 25 K. The presence of the ferromagnetic impurity is observed in the x = 0–0.25 samples.

Table 3.2: Magnetic transition temperatures for the x = 0–1 samples.

Composition (x)	Transition Temperature (K)
1 (Na 100%, Ca 0%)	5 (FM)
0.875 (Na 87.5%, Ca 12.5%)	6 (AFM)
0.75 (Na 75%, Ca 25%)	8 (AFM)
0.625 (Na 62.5%, Ca 37.5%)	10 (AFM)
0.50 (Na 50%, Ca 50%)	13 (AFM), 41 (AFM)
0.25 (Na 25%, Ca 75%)	43 (AFM)
0.10 (Na 10%, Ca 90%)	44 (AFM)
0 (Na 0%, Ca 100%)	45 (AFM)

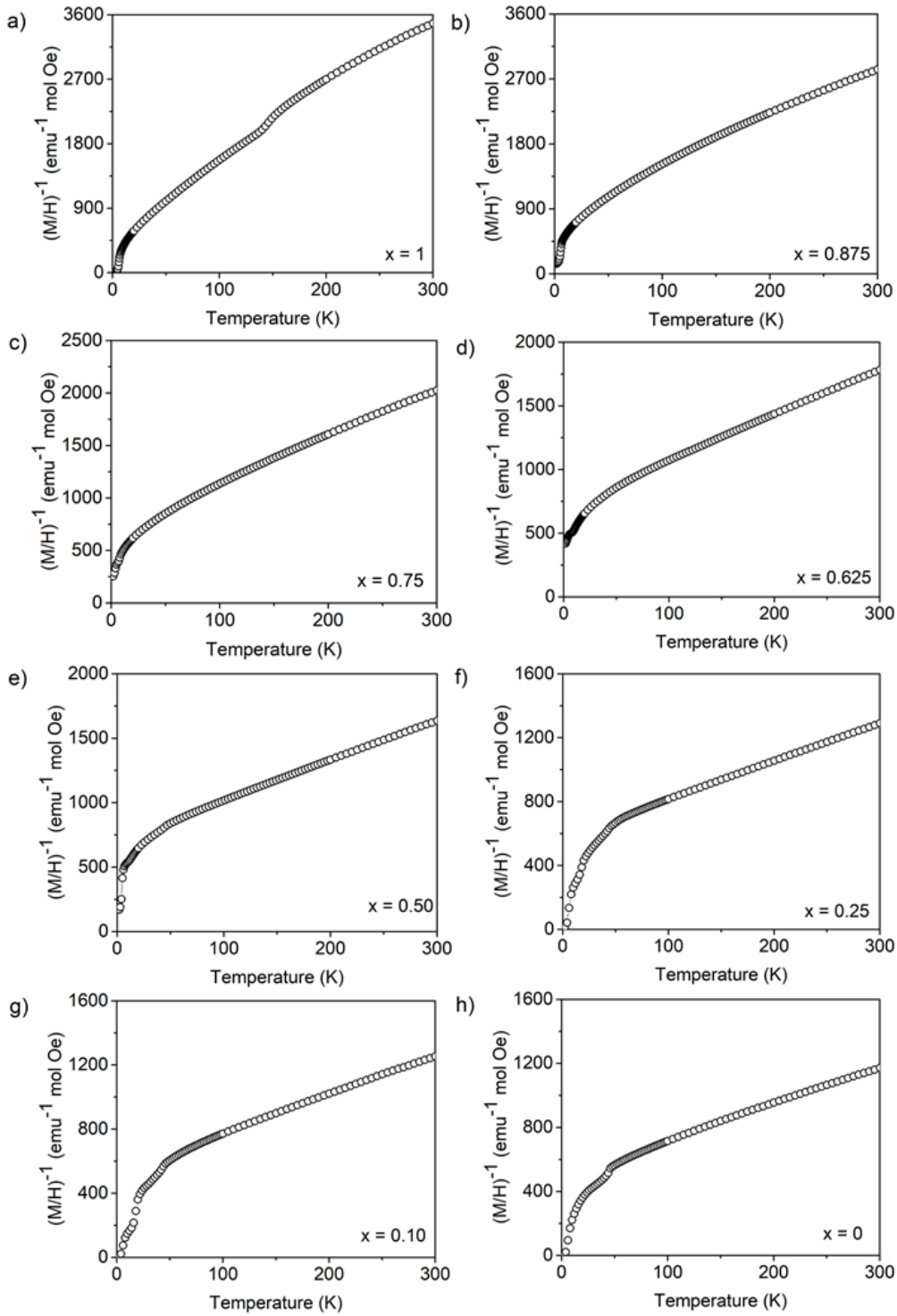

Figure 3.7: Inverse magnetic susceptibility as a function of temperature for the x = 0–1 samples with the diamagnetic correction for the core electrons.

Table 3.3: Effective moments and Weiss constants from Curie-Weiss fit on zero-field cooled data with and without a temperature independent correction.

	Core electron correction only			With χ_0 correction		
x	μ_{eff} (μ_B/f.u.)	Θ (K)	R^2	μ_{eff} (μ_B/f.u.)	Θ (K)	R^2
1				0.64(3)	5(4)	0.99693
0.875	1.067(8)	−123(2)	0.99746	0.823(3)	−56.9(3)	0.99999
0.75	1.329(8)	−156(2)	0.99847	1.062(6)	−90.0(7)	0.99999
0.625	1.510(3)	−207.0(6)	0.99986	1.39(1)	−178(1)	0.99998
0.50	1.608(3)	−229.6(7)	0.99986	1.48(1)	−198(2)	0.99998
0.25	1.853(5)	−257(1)	0.99975	1.64(1)	−207(1)	0.99999
0.10	1.825(7)	−224(1)	0.9995	1.557(8)	−165.6(9)	0.99999
0	1.88(1)	−218(2)	0.9986	1.47(2)	−132(2)	0.99995

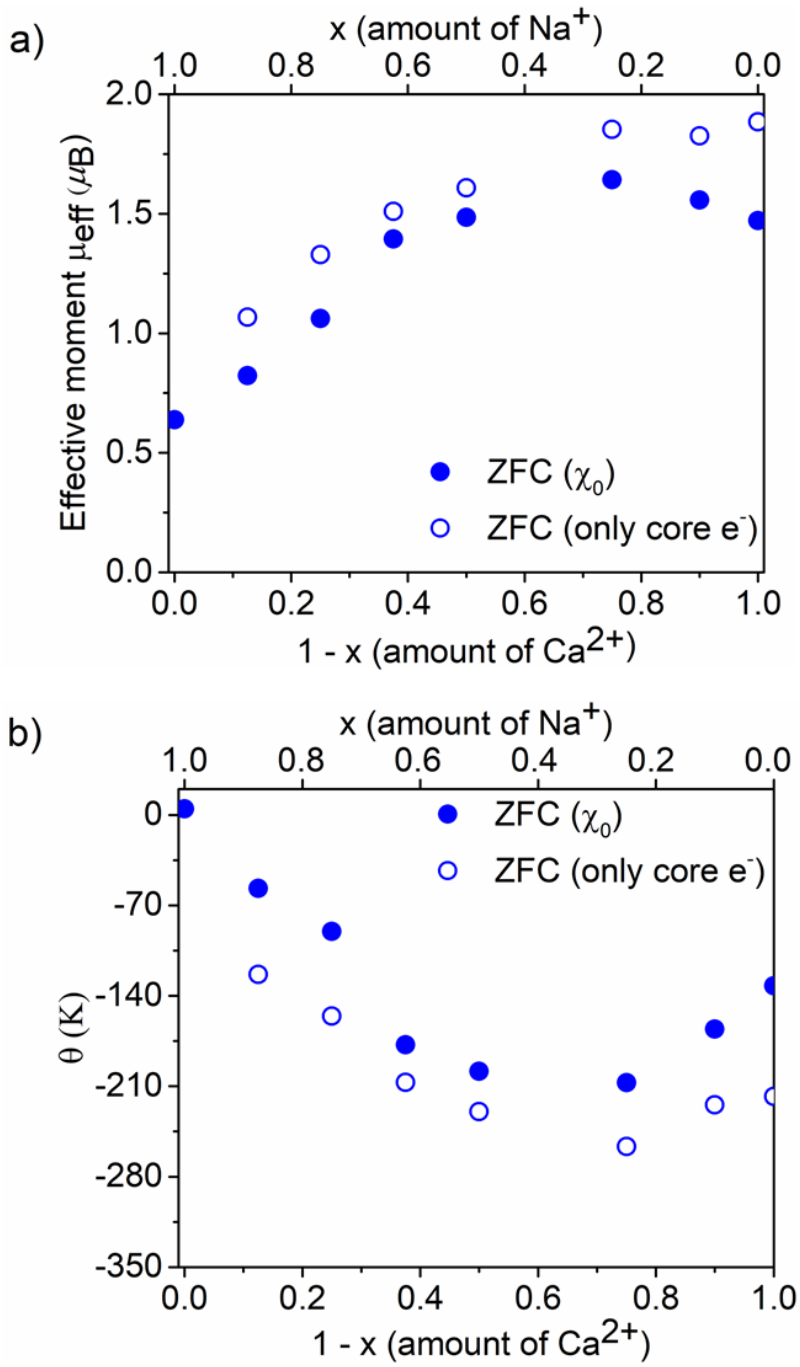

Figure 3.8: a) Effective moment as a function of Ca^{2+}concentration, b) Weiss constant as a function of Ca^{2+}concentration.

3.4 Discussion

Compare to the single crystal Ba_2NaOsO_6 with M_{sat} ~ 0.2 μ_B at 2 K, the magnetic saturation of our Ba_2NaOsO_6 powder sample is significantly lower, and the ferromagnetic transition temperature is at a lower temperature of 6 K as opposed to 8 K.[35] The polycrystalline samples, unlike the single crystal, may have more oxygen vacancies, which introduces Os^{6+} and can lower the Curie temperature. Different polycrystalline samples of Ba_2NaOsO_6 synthesized using the same reagents and reaction batch size can have different Curie temperature and magnetic saturation due to differences in defects (Appendix A). The Ba_2CaOsO_6 sample has a lower magnetic transition temperature than the report in literature at 50 K, which can also be due to differences in defect concentration.

The evolution of the magnetic properties in the $Ba_2Na_xCa_{1-x}OsO_6$ series show the destabilization of the $5d^1$ ferromagnetic ground state at low calcium concentration. With approximately ~12.5% $Ca^{2+,}$ the magnetic ground state is antiferromagnetic. Assuming a random distribution of Ca^{2+}, ~12.5% Ca^{2+} occupation is less than Os^{7+} octahedral environment having five Na^+ neighbors and one Ca^{2+} neighbor. This highlights how fragile this ferromagnetic ground state is to Na^+/Ca^{2+} disorder at the *B* site. There are two possible mechanisms for this destabilization. The first possibility is the electronic effects from the introduction of Os^{6+} with increasing Ca^{2+} concentration, and the randomized distribution of this Os^{7+}/Os^{6+} oxidation states throughout the lattice. The second possibility is the lattice strain from replacing the smaller Na^+ with the larger Ca^{2+} and having a random distribution of Na^+/Ca^{2+} which randomized this lattice strain. From Chapter 2 with the distorted $5d^1$ double perovskite Sr_2ZnReO_6, Sr_2LiOsO_6, and Sr_2NaOsO_6, the magnetic ground state is

shown to be sensitive to the environment of the $5d^1$ cation, so the effects of lattice strain on magnetic ground state is possible. From the current data, it is unclear which mechanism has a larger effect, or if both are important. Current efforts with collaborators in muon spin spectroscopy (mμSR), solid state nuclear magnetic resonance (NMR), X-ray magnetic circular dichroism, and computation are currently underway in order to understand this unusual evolution from ferromagnetism to antiferromagentism.

The evolution of the effective magnetic moment and the Weiss constant is also unusual. The effective moment increases with increasing Ca^{2+} concentration up to x = 0.25 or 75% Ca^{2+}, but then levels off at higher Ca^{2+} concentration. The increase of effective moment is consistent with the growing concentration of $5d^2$ Os^{6+}. However, the leveling off of effective moment at ≥ 75% Ca^{2+} is unexpected. In addition, the Weiss constant decreases with increasing Ca^{2+} concentration up to x = 0.25 or 75% Ca^{2+}, but then levels off at higher Ca^{2+} concentration. The decreasing Weiss constant indicates a strengthening of antiferromagnetic interactions with increasing $5d^2$ Os^{6+}. The saturation at ≥ 75% Ca^{2+} is similar to the trend observed in the effective moment. Preliminary analysis on muon spin spectroscopy data shows a monotonic increase in magnetic transition temperature with Ca^{2+} doping, which is at odds with the saturation of both effective moment and Weiss constant at ≥ 75% Ca^{2+}. One possible explanation is that spin-orbit coupling which reduces the magnetic moment, does not change linearly with Os^{6+} concentration. However, further experiment and computation efforts are currently in progress to investigate these unusual effects.

3.5 Conclusion

The $Ba_2Na_xCa_{1-x}OsO_6$ solid solution was synthesized in order to investigate the effect of Ca^{2+} substitution on the ferromagnetic ground state of Ba_2NaOsO_6. Small concentration of ~12.5 % Ca^{2+} is sufficient to destabilize the ferromagnetic ground state, which highlights the fragile nature of this magnetic ground state. The magnetic transition temperature increases with increasing Ca^{2+} concentration and approaches the transition temperature of the Ba_2CaOsO_6 compound. Current experiments are still ongoing in order to determine the mechanism of this rapid destabilization.

Chapter 4 Structural and Magnetic Phase Diagram of $Ba_xSr_{2-x}NiOsO_6$

4.1 Introduction

Double perovskites containing both 3d and 5d transition metals are an interesting playground to investigate unusual magnetism, due to the variety of competing short range and long range superexchange pathways. Previous work on Ca_2NiOsO_6, Sr_2NiOsO_6, and Ba_2NiOsO_6 suggested that substitution at the *A*-site changes both the structure and the magnetic ground state. Monoclinic $P2_1/n$ Ca_2NiOsO_6 is reported as ferrimagnetic, tetragonal $I4/m$ Sr_2NiOsO_6 was reported as antiferromagnetic, and cubic $Fm\bar{3}m$ Ba_2NiOsO_6 was reported to be antiferromagnetic below 2.1 T and ferromagnetic above 2.1 T and 100 K. This suggests the sensitivity of the magnetic ground state to structural changes. Previous work on other 3d-5d double perovskites suggest that because of the orbital energy mismatch and the competition between the short and long range superexchange interactions, the Goodenough-Kanamori rules[49] cannot be used to make accurate predictions of the magnetic ground state.

In this chapter, the $Ba_xSr_{2-x}NiOsO_6$ (x = 0.2–2) structural and magnetic phase space are explored. By replacing the Ba^{2+} with the smaller Sr^{2+} ion, the positive chemical pressure decreases the Ni–O–Os bond angle which results in an increase of octahedral tilting. This allows us to investigate how the magnetic ground state changes with small perturbation to the structure.

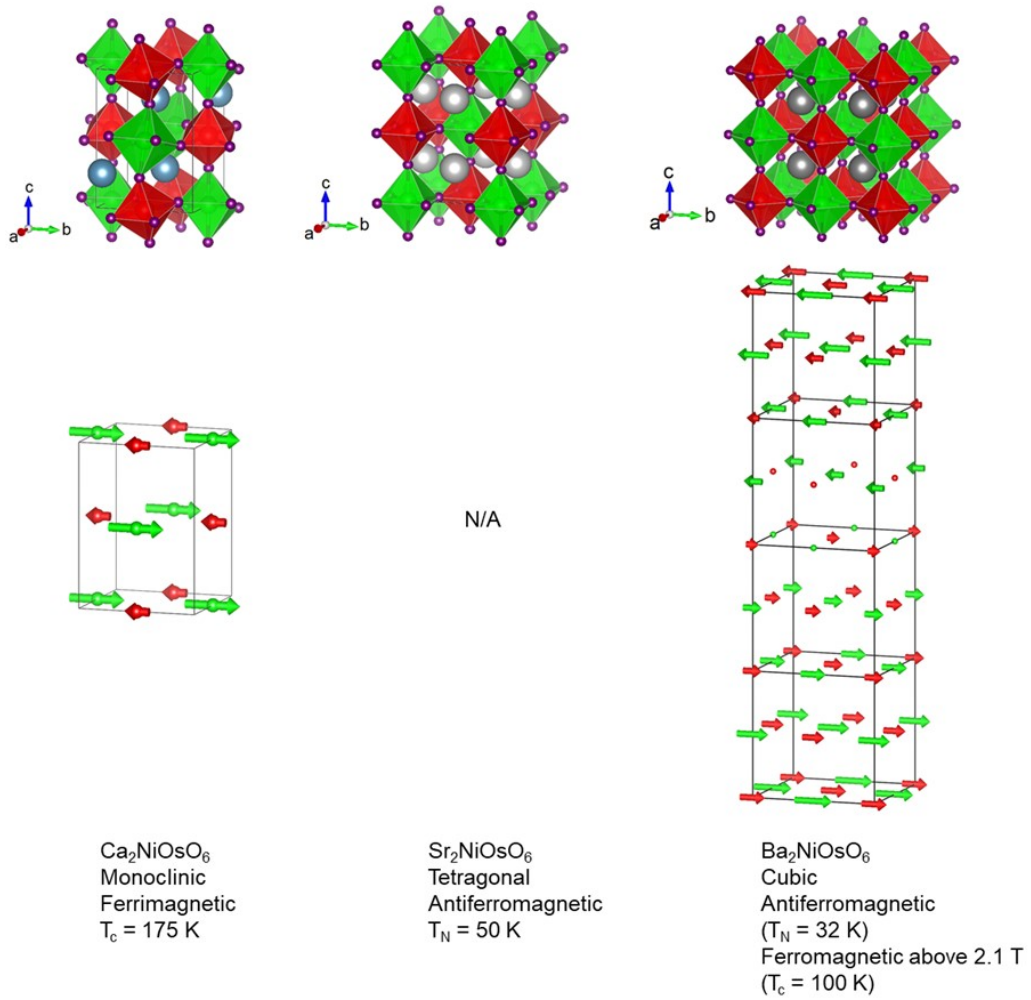

Figure 4.1: Different magnetic ground states of the nickel osmate double perovskites adapted from references [1,50,51]. The magnetic unit cell of high pressure Ba_2NiOsO_6 is cut in half to better visualize the spin arrangement.

4.2 Experimental

Solid solutions of $Ba_xSr_{2-x}NiOsO_6$ (x = 0.2–2) were synthesized using a conventional solid state method with stoichiometric amounts of BaO_2 (99%, Cerac), SrO_2 (99.9% trace metal basis, Sigma-Aldrich), NiO (99.9%, Strem Chemicals), and osmium powder (99.9% trace metals basis, Sigma-Aldrich). The mixture was ground in a mortar and pestle and loaded in a capped alumina tube which was placed in a quartz tube along with a separate container of PbO_2. This quartz tube was sealed under vacuum before being heated to 1000 °C for 48 hours. The PbO_2 acts as an in-situ oxygen source by decomposing to PbO and O_2 at 600 °C. An excess of 1/4 mol O_2 was produced in order to ensure complete oxidation of Os^{6+}. The resulting black powders were then reground and reheated at 1100 °C for another 12 hours to improve sample quality. The stoichiometric reaction is shown below:

$$x\ BaO_2 + (2-x)\ SrO_2 + NiO + Os + (3/2)\ PbO_2 \rightarrow Ba_xSr_{2-x}NiOsO_6 + (3/2)\ PbO + (1/4)\ O_2$$

Powder X-ray diffraction (PXRD) data was collected using a Bruker D8 Advance powder diffractometer (40 kV, 40 mA, sealed Cu X-ray tube) equipped with an incident beam monochromator (Johansson type SiO_2 crystal) and a Lynxeye XE-T position sensitive detector. Variable temperature X-ray diffraction data on the x = 1.2 and 1.4 samples were collected at Durham University on a Bruker D8 X-ray diffractometer from 10 K to 300 K with 5 K steps. Phase purity and cation ordering were determined by powder Rietveld refinement in TOPAS-Academic (v6).[52]

Magnetic susceptibility as a function of temperature (2.5 K–400 K) was collected for each sample with an applied field of 1000 Oe in zero field cooled (ZFC) and field cooled (FC) conditions using a Superconducting Quantum Interference Device (SQUID). A 30–40 mg sample was loaded in a gelatin capsule and mounted in a plastic straw. The diamagnetic contribution from core electrons was subtracted prior to analyzing the data. Magnetization versus applied field data were taken on the same instrument with an applied field of −70 kOe to 70 kOe at 5 K and 300 K for all samples, and also at 60 K for the x = 1.4, 1.6, 1.8, and 2.0 samples.

AC magnetic susceptibility measurement was obtained for the x = 0.6, 1.2, and 1.4 sample using a QD Physical Property Measurement System (PPMS). For each composition the same sample was used for the PPMS and SQUID measurements. The experiment spanned the range of 50–10000 Hz and 20–60 K with a magnetic field of 0.02 Oe. Heat capacity was collected for the x = 1.2 sample from 20 K to 300 K with step size of 4 K on the PPMS.

Neutron powder diffraction measurements for the x = 0.6 sample were conducted at the POWGEN beamline at the Spallation Neutron Source at Oak Ridge National Laboratory. A sample size of 1.2 g $Ba_{0.6}Sr_{1.4}NiOsO_6$ was loaded into a 6 mm vanadium can for the POWGEN Automatic Changer (PAC). A one hour scan was taken at 1.066 Å (Frame 2), and a two hour scan was taken at 3.731 Å (Frame 5) at 10 K and 60 K. A two hour scan was taken at 1.066 Å (Frame 2), and a one hour at 3.731 Å (Frame 4) at 300 K. Rietveld refinements on these diffractograms were done in GSAS and TOPAS-Academic (v6).

Neutron powder diffraction measurements were conducted at the GEM (General Materials Diffractometer) instrument at the ISIS Neutron and Muon source for the x = 1.2 and 2.0 samples. Approximately 7 grams of sample was made by combining six samples, each ~1 g. After the samples were combined they were heated once more in an evacuated quartz tube at 1000 °C for 24 hours. For the x = 1.2 sample, one hour scans were collected at 300 K, 200 K, 150 K, 120 K, 100 K, 90 K, 75 K, 60 K, and 50 K; two hour scans were collected for temperatures near the magnetic transition: 40 K, 25 K, and 10 K; and a four hour scan was collected at 5 K. For the x = 2.0 sample, one hour scans were collected at 300 K, 200 K, 150 K, 120 K, 90 K, 75 K, 60 K, 50 K, 25 K, and a two hour scan was collected at 5 K. In order to determine the presence of magnetic reflections, the diffraction patterns below the magnetic transition temperature were compared to the patterns collected at 120 K, rather than 300 K, to account for the added background that comes from the cryostat. Rietveld refinements on these diffractograms were done in TOPAS-Academic (v6).

4.3 Results

4.3.1 Structural studies on $Ba_xSr_{2-x}NiOsO_6$

The room temperature powder X-ray diffraction patterns for $Ba_xSr_{2-x}NiOsO_6$ (x = 0.2–2) were modeled with three space groups: tetragonal $I4/m$, cubic $Fm\bar{3}m$, and trigonal $P\bar{3}m1$. All PXRD refinements were completed assuming a random distribution of Ba^{2+} and Sr^{2+} at the *A*-site. The possibility of antisite disorder between Ni^{2+} and Os^{6+} cations was

also investigated, but these refinements did not improve R_{wp} or goodness of fit significantly. Thus, their occupations were fixed to unity. The occupation and complete ordering of the *B*-site observed in X-ray diffraction was assumed to extend to the neutron diffraction refinements, which are not very sensitive to antisite disorder due to the similar neutron scattering lengths of Os and Ni.[53]

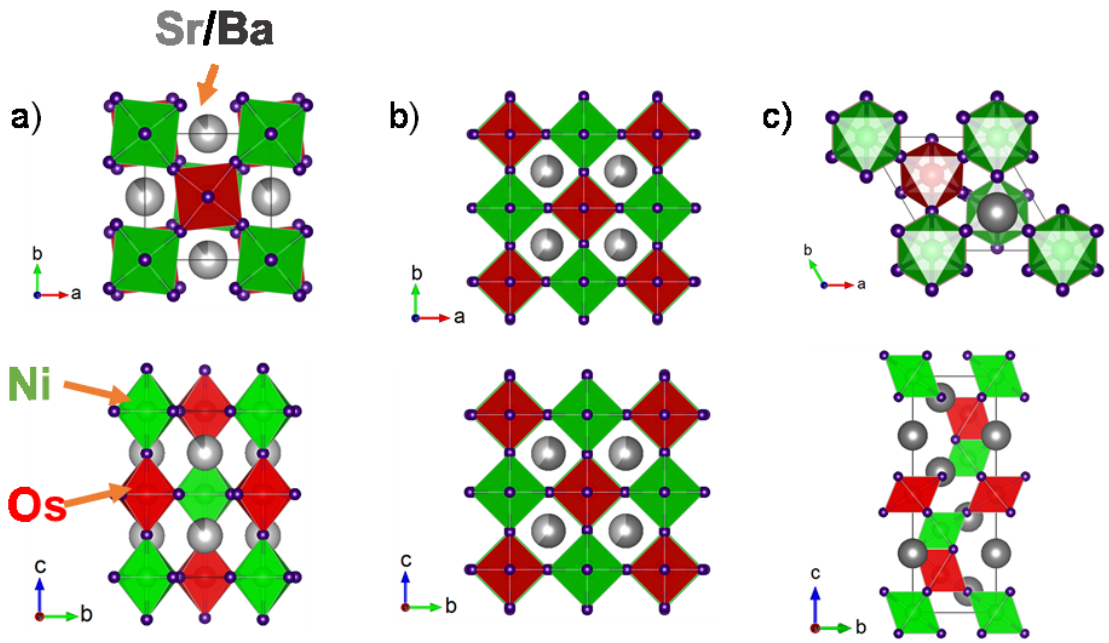

Figure 4.2: The three main phases in the $Ba_xSr_{2-x}NiOsO_6$ series a) $I4/m$, b) $Fm\bar{3}m$, and $P\bar{3}m1$.

Powder X-ray diffraction patterns (PXRD) of the x = 0.2–0.6 samples were fitted to the $I4/m$ space group previously reported for Sr_2NiOsO_6. The room temperature powder X-ray diffraction pattern of the x = 0.6 sample was fitted to both $I4/m$ and $Fm\bar{3}m$ with the tetragonal structure giving a better fit (R_{wp} of 13.23 and 11.54, respectively). No observable tetragonal splitting was observed for the x = 0.6 sample in the PXRD data, although the

asymmetric peak profile suggests the symmetry is lower than cubic. Fitting the neutron diffraction data at 300 K for the x = 0.6 sample with the $Fm\bar{3}m$ space group does not properly account for the intensities of some of weak reflections. Fitting with the $I4/m$ space group improves the refinement at these low intensity reflections, dropping the R_{wp} from 7.025 to 6.640. Due to the better sensitivity of neutron diffraction to oxygen position, the room temperature structure of the x = 0.6 sample was assigned to be $I4/m$. It is possible that the tetragonal to cubic phase transition for x = 0.6 is close to room temperature, which explains the unusual shape of the peak profile in the PXRD pattern.

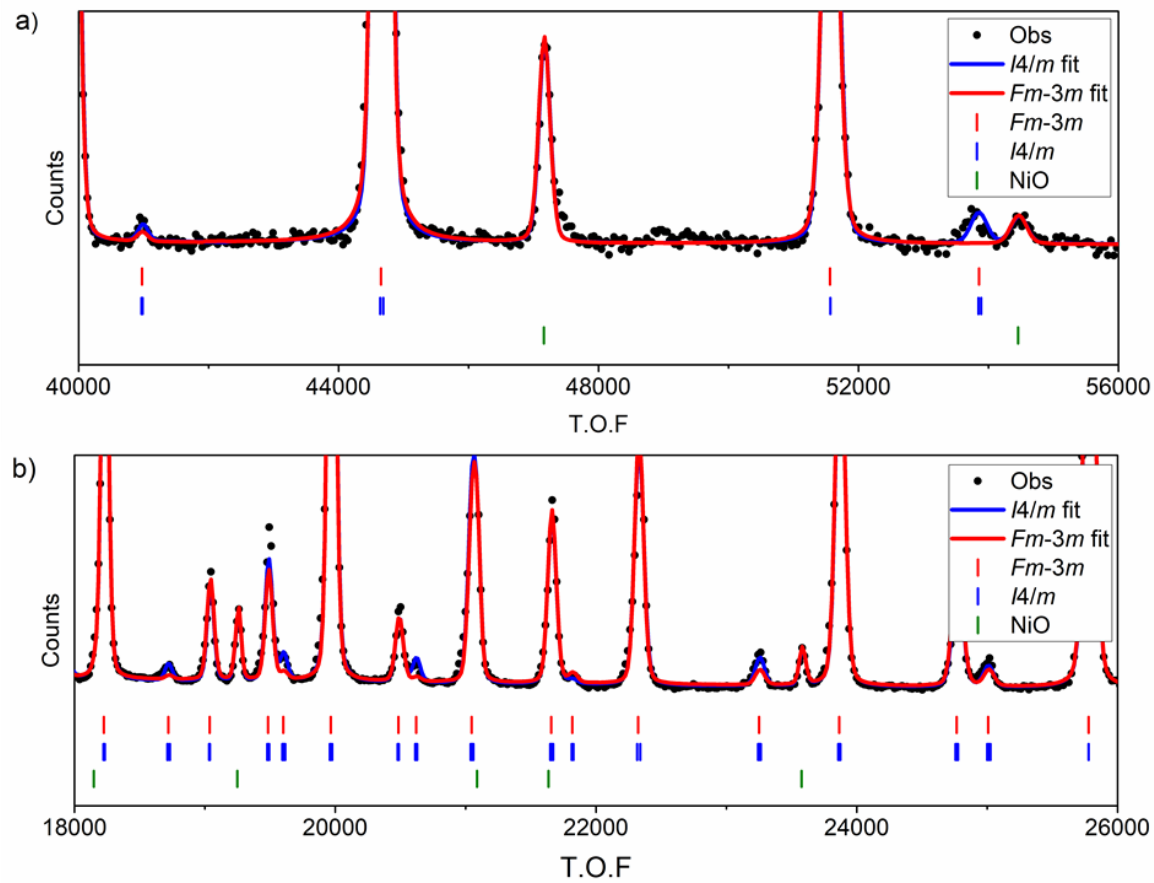

Figure 4.3: Powder neutron diffraction pattern at 300 K of the x = 0.6 sample which appears metrically cubic with laboratory X-ray diffraction. Rietveld refinements show that the *I*4/*m* structural model gives a better fit than the $Fm\bar{3}m$ and *I*4/*m* model.

The room temperature PXRD pattern of the x = 0.8–1.2 sample fit well with the $Fm\bar{3}m$ space group with symmetric PXRD peaks. Variable temperature PXRD and neutron diffraction data of the x = 1.2 sample at 5 K shows that the structure remains cubic down to at least 5 K, which is below the magnetic transition temperature. The lattice parameter as a function of temperature for the x = 1.2 sample shows an expansion of the lattice with increasing temperature.

The PXRD data of x = 1.4–1.8 shows a mixture of $Fm\bar{3}m$ and $P\bar{3}m1$ phases with increasing percentage of the trigonal phase with increasing barium substitution. Variable temperature X-ray diffraction on the x = 1.4 sample shows the lattice parameter for both the cubic and the trigonal phase expand with increasing temperature, with no change in the percentage of each phase. At x = 2.0, the PXRD pattern only the trigonal phase with $P\bar{3}m1$ symmetry is observed. The most common space groups reported for double perovskite-related hexagonal structure are $P6_3/mmc$, $P6_3mc$, *and* $P\bar{3}m1$. Previous reports have assigned $P\bar{3}m1$ to $Ba_2Fe_{1.12}Os_{0.88}O_6$,[54] $P6_3mc$ to $Ba_2Fe_{0.86}Os_{1.14}O_6$,[55] $P6_3mc$ to $Ba_2Co_{0.84}Os_{1.16}O_6$,[55] and $P6_3/mmc$ to $Ba_2Mn_{1.34}Os_{0.66}O_6$.[55] Thus, our Ba_2NiOsO_6 sample was indexed in GSAS-II and Topas-6. By doing Rietveld refinement using the possible space groups of $P\bar{3}m1$, $P6_3mc$, and $P6_3/mmc$, the $P\bar{3}m1$ space group with less restricted systematic absences due to lack of glide planes or screw axes yields the best fit that accounts for all intensity. Rietveld refinement was done on all X-ray and neutron diffraction data using this space group.

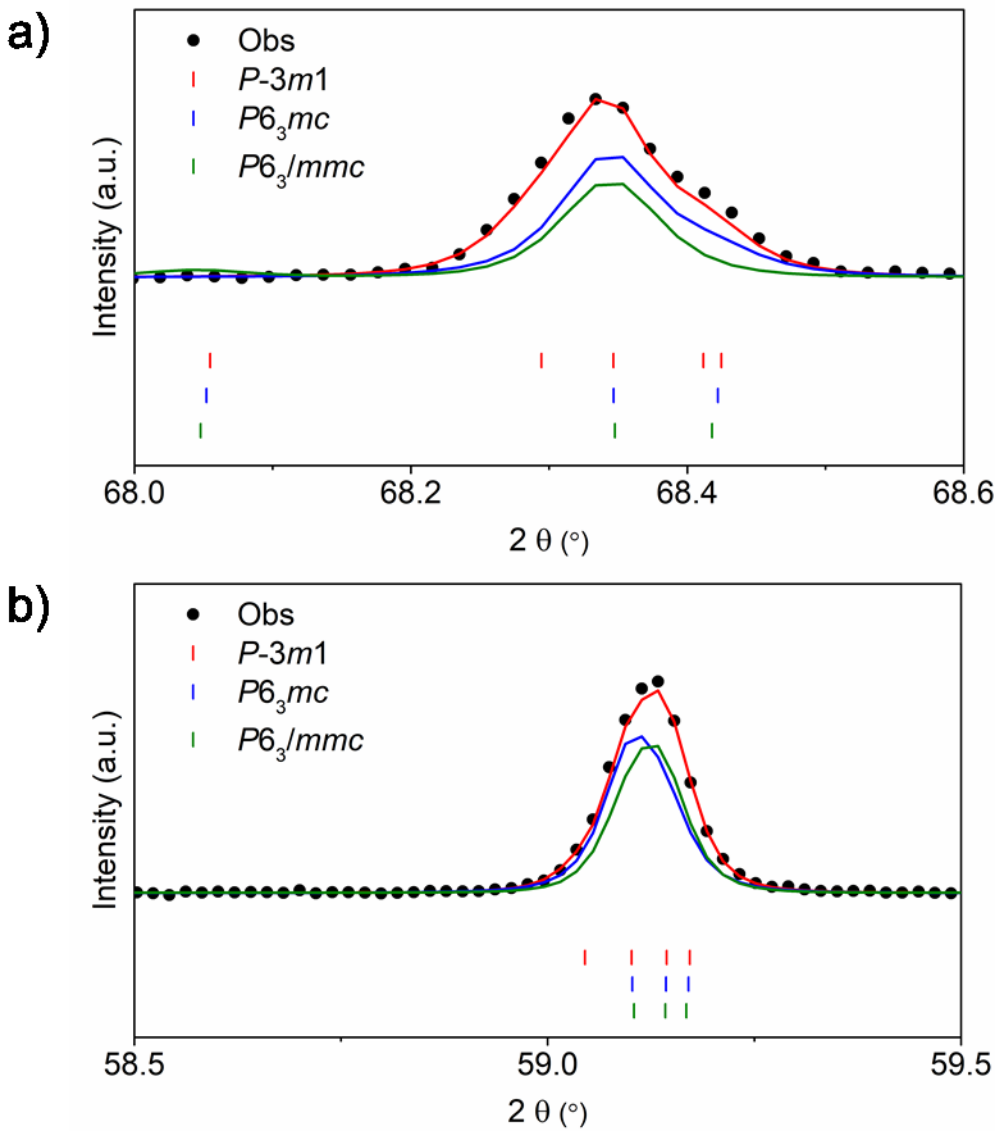

Figure 4.4: The x = 2.0 sample was fitted with the $P\bar{3}m1$, $P6_3mc$, and $P6_3/mmc$ space group.

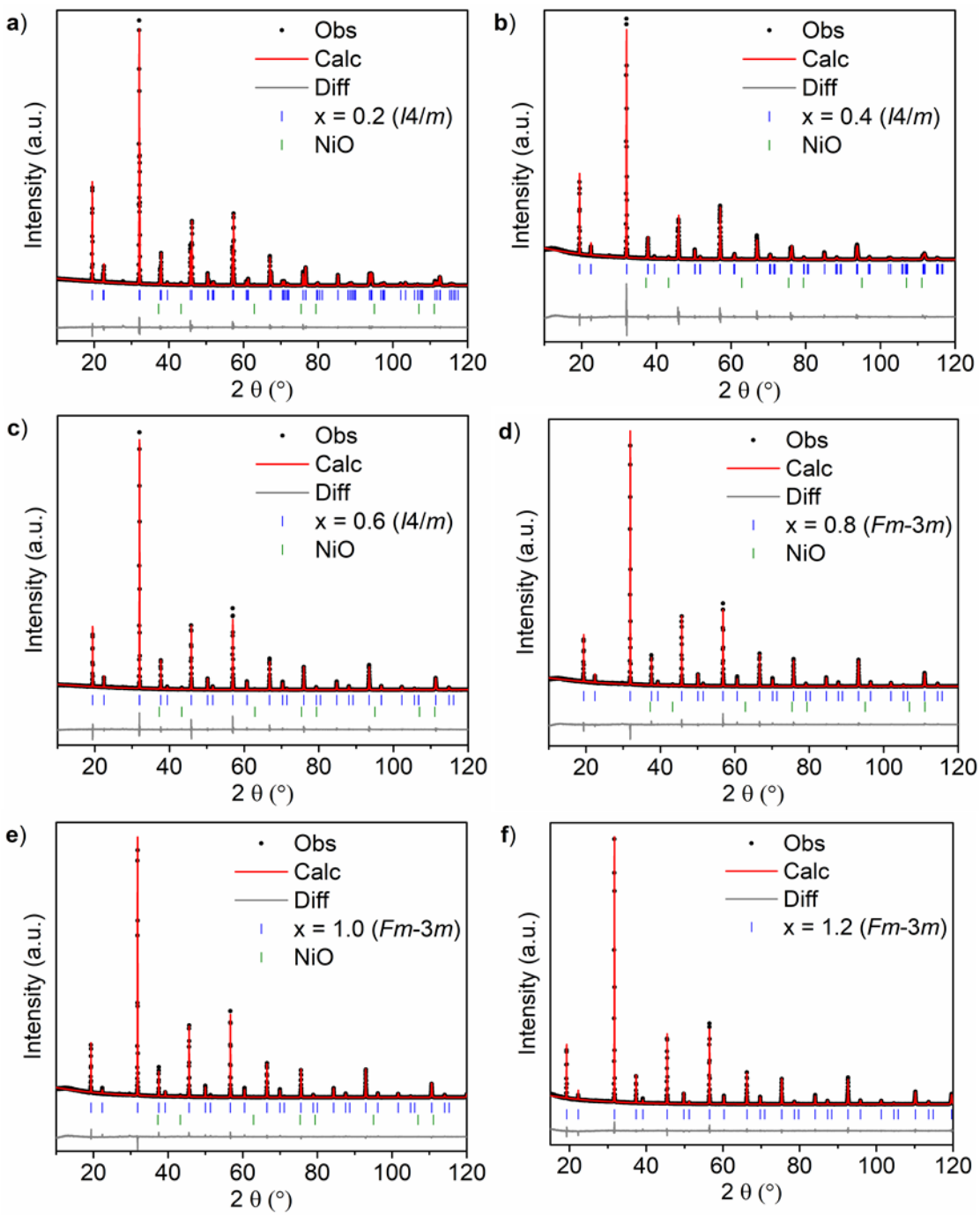

Figure 4.5: The room temperature PXRD patterns of x = 0.2–1.2.

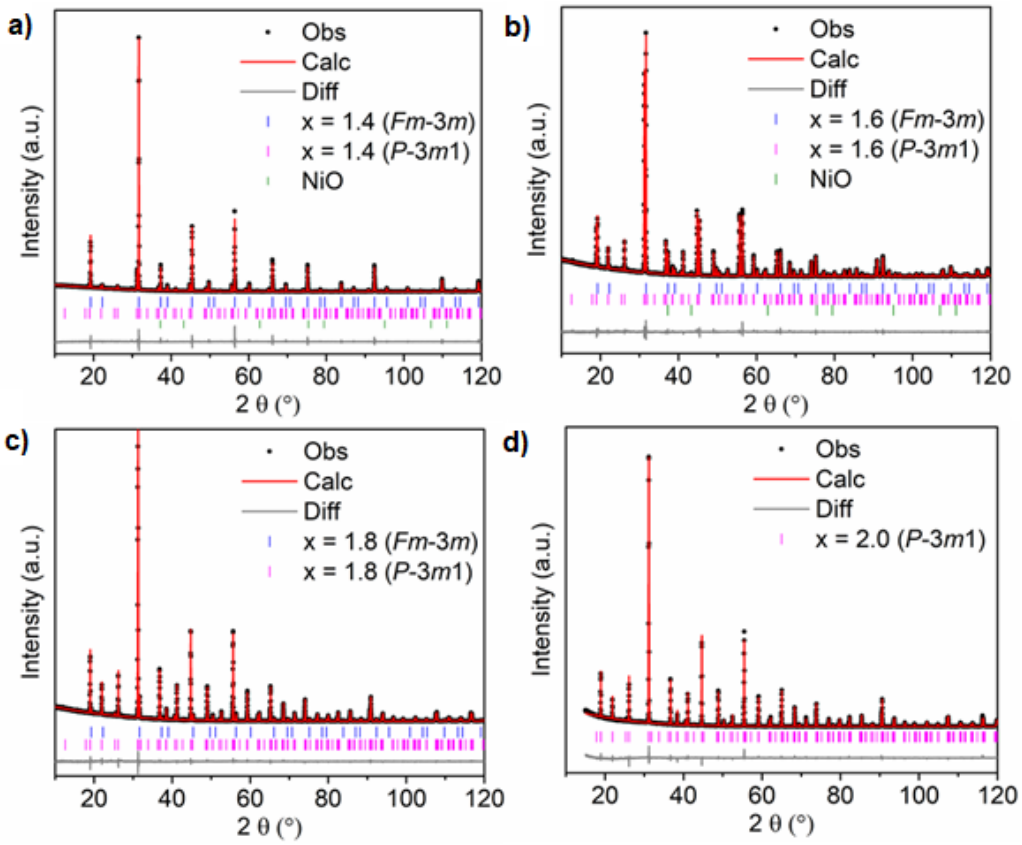

Figure 4.6: The room temperature PXRD patterns of x = 1.4–2.0.

Table 4.1: Structural information for I/4m samples (x = 0.2–0.6) taken from refinement of the laboratory X-ray data. The Ba/Sr occupy the 4d (0 0 1/4) site. The Ni occupy the 2a (0 0 0) site, and the Os occupy the (0 0 1/2) site. B_{iso} was fixed to the same value for Ni and Os.

X	0.2	0.4	0.6
Space group	*I*4/*m*	*I*4/*m*	*I*4/*m*
a (Å)	5.55301(3)	5.57666(7)	5.5957(1)
c (Å)	7.92427(5)	7.9161(1)	7.9158(2)
Volume (Å^3)	244.352(3)	246.186(8)	247.86(1)
R_{wp}	8.840	11.848	11.320
Gof	2.072	2.960	2.444
O1 (0, 0, z), 4e	0 0 0.2550(7)	0 0 0.250(2)	0 0 0.259(2)
O2 (x, y, 0), 8h	0.280(1) 0.226(1) 0	0.283(3) 0.219(3) 0	0.271(3) 0.220(4) 0
Ba/Sr B_{iso}(Å^2)	0.59(2)	0.67(5)	0.64(5)
Ni B_{iso}(Å^2)	0.16(2)	0.23(3)	0.01(2)
Os B_{iso}(Å^2)	0.16(2)	0.23(3)	0.01(2)
O B_{iso}(Å^2)	0.8(1)	0.4(2)	0.4(2)

Table 4.2: Structural information for $Fm\bar{3}m$ structures (x = 0.8–1.4) taken from refinement of the laboratory X-ray data. The Ba/Sr occupy the 8c (1/4 1/4 1/4) site. The Ni occupy the 2a (1/2 1/2 1/2) site, and the Os occupy the 4a (0 0 0) site. Phase percent is by weight. B_{iso} was fixed to the same value for Ni and Os.

x	0.8	1.0	1.2	1.4	1.6	1.8
Space group	$Fm\bar{3}m$	$Fm\bar{3}m$	$Fm\bar{3}m$	$Fm\bar{3}m$	$Fm\bar{3}m$	$Fm\bar{3}m$
% wt.	0 %	0 %	0 %	88.1(2) %	46.3(1) %	4.31(8) %
a (Å)	7.93145(3)	7.94978(3)	7.97021(3)	7.98548(4)	7.98705(4)	7.98923(9)
Volume (Å^3)	498.952(6)	502.418(5)	506.302(6)	509.223(6)	509.517(7)	509.93(2)
R_{wp}	8.136 %	7.566 %	7.789 %	10.471 %	6.445 %	5.744 %
Gof	1.741	1.708	1.785	2.213	1.396	1.218
O (x, 0, 0), 24e	0.2497(5)	0.2471(5)	0.2470(6)	0.2447(7)	0.2425(7)	0.241(4)
Ba/Sr B_{iso}(Å^2)	0.27(5)	0.59(6)	0.86(9)	1.5(2)	0.40(4)	0.2(1)
Ni B_{iso}(Å^2)	0.01(2)	0.01(2)	0.01(2)	0.01(3)	0.15(2)	0.2(1)
Os B_{iso}(Å^2)	0.01(2)	0.01(2)	0.01(2)	0.01(3)	0.15(2)	0.2(1)

Table 4.3: Structural information for $P\bar{3}m1$ structures (x = 1.4–2.0) taken from refinement of the laboratory X-ray data. The Ba/Sr occupy the 2c and 2d Wyckoff site. The Ni occupy the 1a and 2d site. The Os occupy the 1b and 2d site.

X	1.4	1.6	1.8	2.0
Space group	$P\bar{3}m1$	$P\bar{3}m1$	$P\bar{3}m1$	$P\bar{3}m1$
Wt. %	11.6(2) %	52.7(1) %	95.69(8) %	100 %
A	5.71852(8)	5.71824 (2)	5.71873(2)	5.73100(2)
C	14.0469(4)	14.0459(1)	14.04780(7)	14.06890(8)
Volume	397.809(6)	397.745(4)	397.867(3)	462.085(3)
R_{wp}	10.417	6.337	5.744	7.453
Gof	2.213	1.373	1.218	1.708
Ba/Sr (1)	0 0 0.249(2)	0 0 0.2478(5)	0 0 0.2487(3)	0 0 0.2504(4)
Ba/Sr (2)	1/3 2/3 0.091(1)	1/3 2/3 0.0897(3)	1/3 2/3 0.0890(2)	1/3 2/3 0.0899(3)
Ba/Sr (3)	1/3 2/3 0.403(1)	1/3 2/3 0.4034(3)	1/3 2/3 0.4036(2)	1/3 2/3 0.4044(2)
Ni(2)	1/3 2/3 0.645(3)	1/3 2/3 0.6517(8)	1/3 2/3 0.6522(5)	1/3 2/3 0.6504(7)
Os(2)	1/3 2/3 0.8390(9)	1/3 2/3 0.8406(2)	1/3 2/3 0.8409(1)	1/3 2/3 0.8398(2)
O1	0.517(6) −0.517(6) 0.267(6)	0.515(2) −0.515(2) 0.252(3)	0.511(1) −0.511(1) 0.249(2)	0.5122(9) −0.5122(9) 0.268(1)
O2	0.845(7) −0.845(7) 0.090(5)	0.840(2) −0.840(2) 0.084(2)	0.833(1) −0.833(1) 0.082(1)	0.829(2) −0.829(2) 0.089(2)
O3	0.825(8) −0.825(8) 0.432(4)	0.839(2) −0.839(2) 0.420(1)	0.843(1) −0.843(1) 0.4172(9)	0.824(2) −0.824(2) 0.424(2)
Ba/Sr B_{iso}(Å^2)	0.01(9)	0.40(4)	0.44(2)	0.18(3)
Ni B_{iso}(Å^2)	0.01(9)	0.15(2)	0.02(2)	0.1(1)
Os B_{iso}(Å^2)	0.01(9)	0.15(2)	0.02(2)	0.1(1)
O B_{iso}(Å^2)	0.01(9)	0.7(1)	0.58(8)	2.9(2)

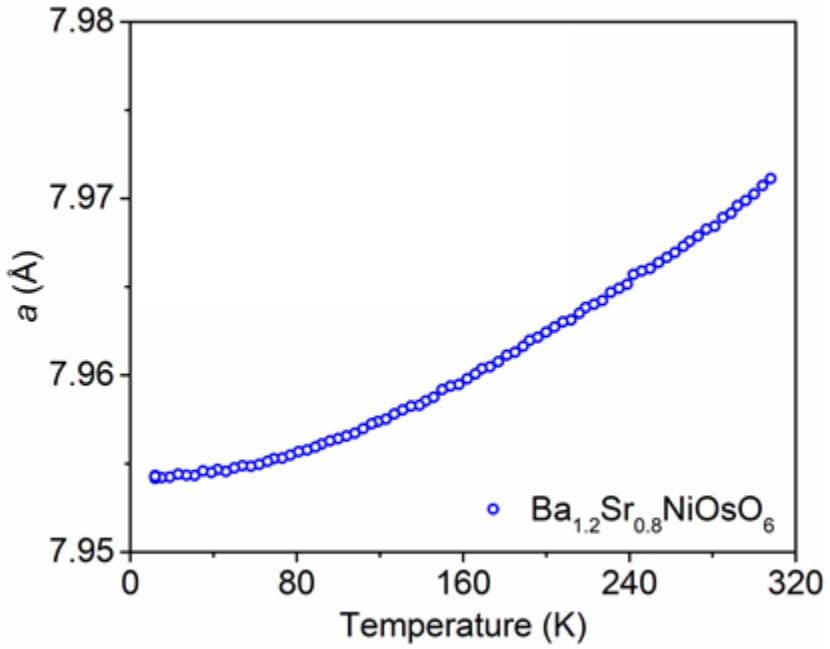

Figure 4.7: Variable temperature PXRD of the x = 1.2 sample showing an increase in lattice parameter with increasing temperature. The structure remains cubic below the magnetic transition at 40 K.

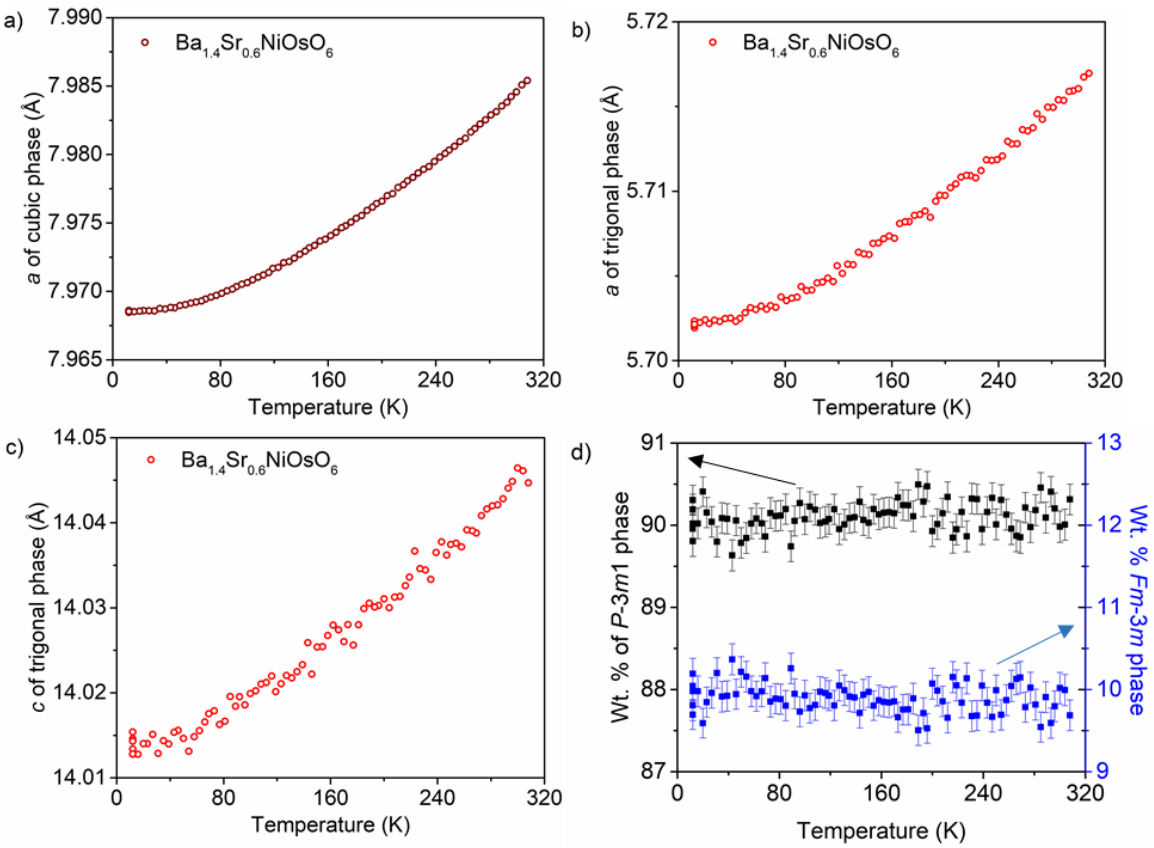

Figure 4.8: Variable temperature PXRD of the x = 1.4 sample showing an increase in lattice parameter with increasing temperature for both the cubic and the trigonal phase. The phase composition is constant with temperature.

Variable temperature PXRD data above 300 K were collected for the x = 0–0.4 samples, and lattice parameters obtained from Rietveld refinement were plotted as a function of temperature in order to determine the tetragonal to cubic phase transition temperature for each sample. The *a* lattice parameter of the tetragonal space group (a_{tetra}) is related to the a lattice parameter of the cubic space group (a_{cubic}) by the relationship $a_{\text{tetra}}\sqrt{2} \approx a_{\text{cubic}}$. Thus, the tetragonal to cubic phase transition is expected where $a\sqrt{2}$ and *c* converge. A linear function was fitted to the phase transition temperature as a function of composition. The resulting linear function is consistent with the structural observation of tetragonal x = 0.2–0.6 and cubic 0.8–1.2 at room temperature.

Table 4.4: Tetragonal to cubic phase transition temperatures taken from variable temperature PXRD data used for the linear fit.

Composition (x)	Tetragonal to cubic phase transition (K)
0	653
0.2	533
0.4	453

The $Fm\bar{3}m$ and $P\bar{3}m1$ phase fractions obtained from Rietveld refinements of the x = 1.4–1.6 were used in conjunction with the lever rule to estimate the width of the mixed phase region. Using the lever rule, the phase fraction dependence of these boundaries are:

$$\text{Phase fraction of } Fm\bar{3}m = \frac{e_2 - x}{e_2 - e_1}$$

$$\text{Phase fraction of } P\bar{3}m1 = \frac{x - e_1}{e_2 - e_1}$$

where e_1 is the largest barium content that can be accommodated within the cubic phase, e_2 is the smallest barium content that can be accommodated within the trigonal phase, and x is the amount of barium substitution. From PXRD analysis of the x = 1.4, 1.6, and 1.8 samples, the phase fraction as a function of composition can be expressed by three independent equations. Due to the errors on the phase fraction of the PXRD analysis, the phase fraction of the cubic phase and the phase fraction of the trigonal phase were expressed with three equations each from the x = 1.4, 1.6, and 1.8 samples. The values for e_1 and e_2 are solved from the x = 1.4 and 1.6 equations, then the x = 1.4 and 1.8 equations, and finally the x = 1.6 and 1.8 equations. The resulting values for e_1 and e_2 were averaged. The boundary between the cubic and the mixed phase region was determined to be x = 1.35(1). The boundary between the mixed phase region and the trigonal phase was determined to be x = 1.83(1).

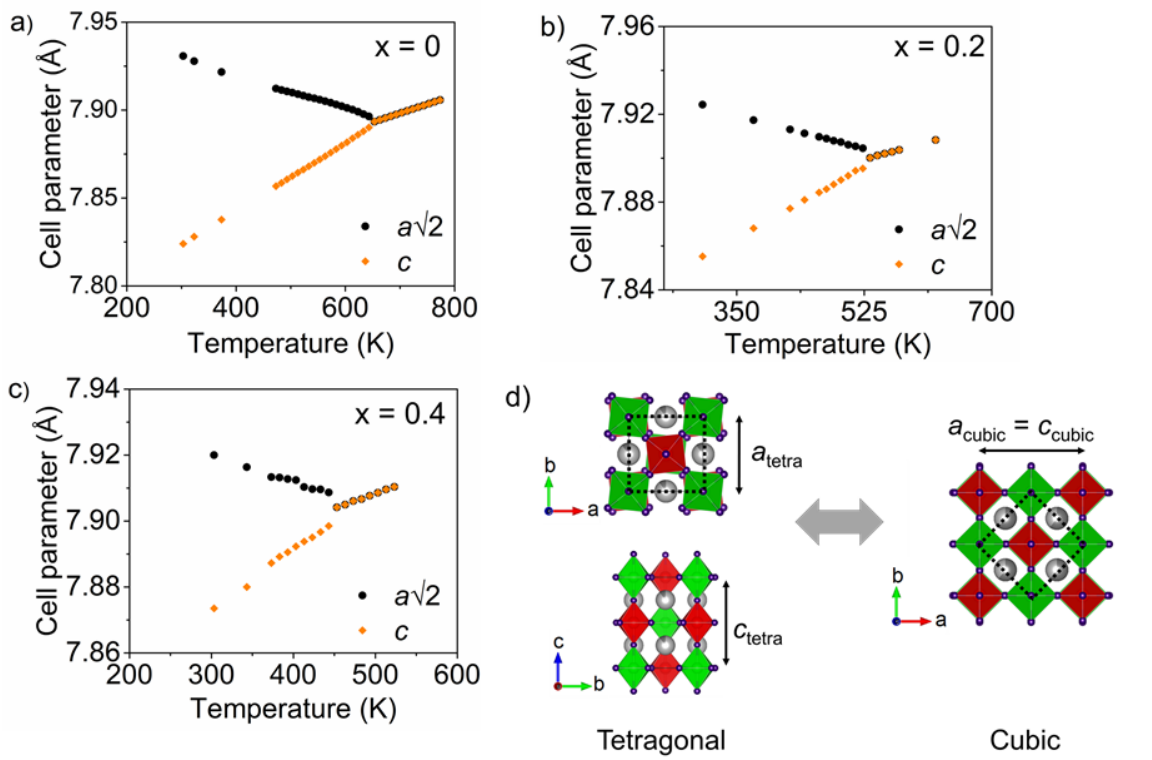

Figure 4.9: Cell parameters for the x = 0–0.4 samples as a function of temperature. The tetragonal to cubic transition is defined here as the temperature at which $a\sqrt{2}$ and c converge.

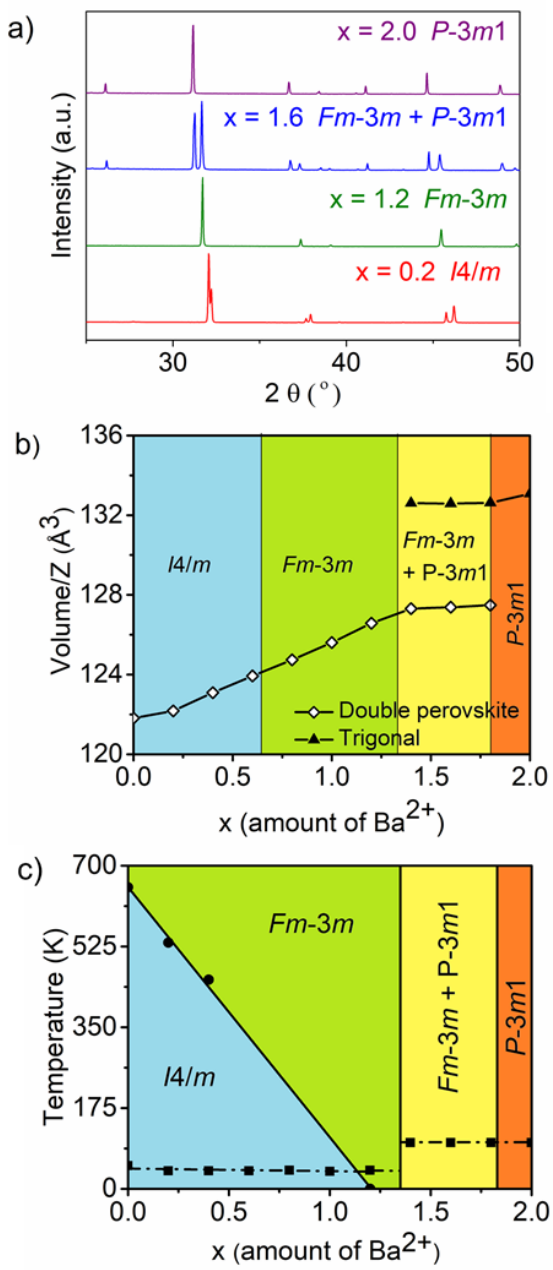

Figure 4.10: a) PXRD patterns of the four structural regions for the $Ba_xSr_{2-x}NiOsO_6$ (x = 0.2–2) system, b) Volume/Z at room temperature as a function of barium amount, c) structural phase diagram where the solid lines separates structural regions and the dash lines separate the paramagnetic state from the magnetic ground state.

Table 4.5: Selected structural information for the $Ba_xSr_{2-x}NiOsO_6$ series. The ∠Ni–O–Os bond angles are for the corner-connected ∠Ni–O–Os bonds. Data for x = 1.2 and 2.0 were taken from neutron diffraction data which has more precise oxygen positions.

x	**0.2 (PXRD)**	**1.2 (NPD)**	**2.0 (NPD)**
Space group	$I4/m$	$Fm\bar{3}m$	$P\bar{3}m1$
a (Å)	5.55301(3)	7.972(1)	5.731(2)
c (Å)	7.92427(5)	---	14.067(4)
Volume (Å^3)	244.352(3)	506.5(2)	400.1(3)
R_{wp}	8.832	3.661	2.810
Gof	2.070	2.743	1.971
Os–O (Å)	1.941(6) ×2 1.951(7) ×4	1.9272(4) ×6	1.9298(9) ×6 1.933(1) ×2 1.948(2) ×4
∠Ni–O–Os (corner connected)	167.5(5)° 180°	180° ---	179.85(7) ° 175.00(7) °
∠Ni–O–Os (face sharing)	---	---	82.58(4) °

4.3.2 DC and AC magnetic susceptibility

DC magnetic susceptibility as a function of temperature at 1 kOe for the samples in the $I4/m$ structural region shows an antiferromagnetic-like cusp at 40 K. A linear Curie-Weiss function was fitted to the inverse magnetic susceptibility for the temperature region of 150 K to 400 K for all samples. For these samples within the $I4/m$ phase space, the Weiss constant extracted from the fit are all positive values which suggest ferromagnetic interactions despite the antiferromagnetic cusp in the magnetic susceptibility data. There is

no observable trend with the calculated effective moment as a function of barium substitution concentration. The effective moment values are close to approximately 3.6 μ_B which is smaller than the spin only value of 4 μ_B. Isothermal magnetization at 5 K is linear for the x = 0.2 sample. As the amount of barium substitution increases, a small opening is observed, but does not saturate up to 70 kOe. This indicates that the *I*4/*m* phase space is not fully a long-range antiferromagnetic ground state. AC magnetic susceptibility on the x = 0.6 (in the *I*4/*m* region) showed slight shifting of the transition temperature to higher values with increasing frequency. Frequency dependence of the magnetic transition temperature would suggest a glassy magnetic ground state.[56] The temperature step size is not fine enough to calculate the amount of shifting or the activation energy between the low-lying metastable states. There is no feature in the neutron diffraction pattern at 10 K that would indicate long range magnetic order, which is consistent with a spin glass magnetic state.

Table 4.6: Weiss temperature and effective moment extracted from linear Curie-Weiss fit from 150 K to 400 K for the $Ba_xSr_{2-x}NiOsO_6$ series. Weiss constant and effective moment from linear Curie-Weiss fitting of the inverse susceptibility data from 150 K to 400 K. Some of the mixed phase samples have an amount of NiO impurity so the phase percent listed here do not add up to 100 %.

Composition (x)	Structure (300 K)	Weiss temperature (K)	Effective moment (μ_B)
0.2	$I4/m$	24(1)	3.64(2)
0.4	$I4/m$	41.2(5)	3.613(6)
0.6	$I4/m$	50.2(3)	3.638(3)
0.8	$Fm\bar{3}m$	68.2(5)	3.614(6)
1.0	$Fm\bar{3}m$	74.7(4)	3.503(5)
1.2	$Fm\bar{3}m$	78.6(4)	3.613(5)
1.4	87.4(2) % $Fm\bar{3}m$ 12.3(2) % $P\bar{3}m1$	97(3)	3.58(4)
1.6	51.5(2) % $P\bar{3}m1$ 47.4(2) % $Fm\bar{3}m$	48.5(8)	3.61(1)
1.8	95.68(8) % $P\bar{3}m1$ 4.32(8) % $Fm\bar{3}m$	7.3(9)	3.63(1)
2.0	$P\bar{3}m1$	−17.7(5)	3.852(7)

Variable temperature DC magnetic susceptibility at 1 kOe for the samples in the $Fm\bar{3}m$ phase space shows a similar cusp at 40 K that was observed in the $I4/m$ structure, which suggest the two structures have similar magnetic ground state. The Curie-Weiss fit of the inverse susceptibility from 150 K to 400 K yields a positive Weiss constant and an effective moment of 3.5–3.6 μ_B, similar to the $I4/m$ samples. Isothermal magnetization collected at 5 K shows no magnetic saturation and small opening loop, also similar to the $I4/m$ samples. For the x = 1.2 sample, typical glassy frequency dependence of the transition temperature was not observable in the AC susceptibility measurement within the 1 K step

size used for the data collection which suggests complex glassy behavior. There is no feature in the specific heat measurement, which confirms there is no long range magnetic ordering for the $Fm\bar{3}m$ structure.

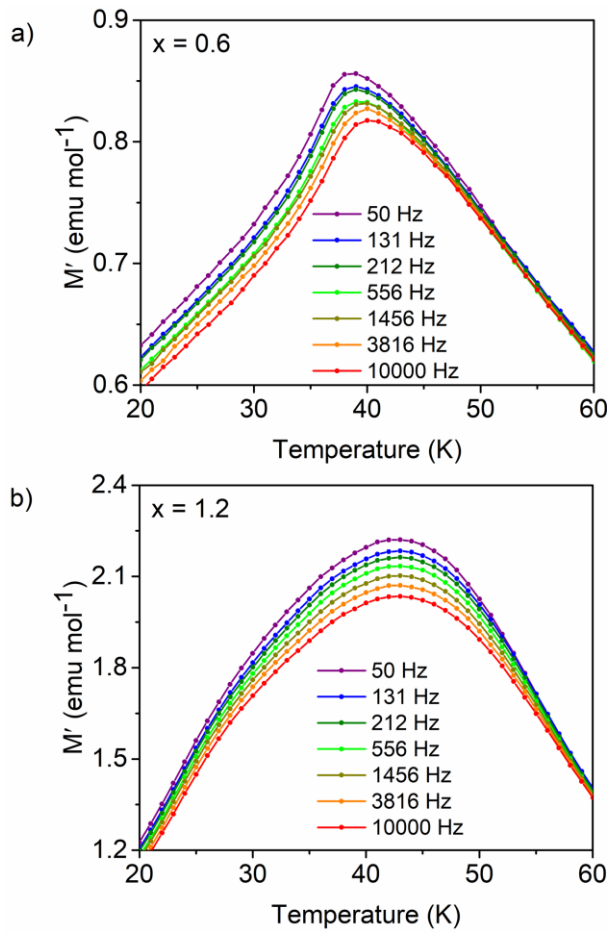

Figure 4.11: AC magnetic susceptibility for x = 0.6 and x = 1.2.

DC magnetic susceptibility at 1000 Oe of the x = 1.4–1.8 samples with mixed cubic and trigonal phases show a sharp rise in magnetic susceptibility below 100 K which is consistent with the onset of ferromagnetism or ferrimagnetism. Isothermal magnetization measurement at 60 K show saturation of the magnetization which also confirms the presence of a ferromagnetic or ferrimagnetic phase. Since the cubic $Fm\bar{3}m$ phase is glassy,

the ferromagnetism or ferrimagnetism at 100 K must originate from the trigonal $P\bar{3}m1$ phase. The x = 1.4 and x = 1.6 samples with ~10 % and ~ 50% also show a weak cusp at approximately 40 K which is consistent with the glassy cubic $Fm\bar{3}m$ phase observed in the x = 1.2 sample. The magnetic data of the mixed phase samples show both signatures of the trigonal $P\bar{3}m1$ and cubic $Fm\bar{3}m$ phases.

Variable temperature DC magnetic susceptibility measurement at 1 kOe for the trigonal Ba_2NiOsO_6 compound showed a ferromagnetic-like transition at 108 K where the sharp rise in magnetic susceptibility occurs. A linear Curie-Weiss function, fitted to the inverse magnetic susceptibility from 150 K to 400 K, results in a Weiss temperature of −17.7(5) K. The negative Weiss value signals the presence of antiferromagnetic coupling in the compound. This suggest a ferrimagnetic ground state, which is confirmed by solving the magnetic structure from neutron diffraction at 5 K. The effective moment extracted from the Curie-Weiss fit is 3.852(7) μ_B. Isothermal magnetization collected at 60 K shows a magnetic hysteresis with a saturation magnetization of 0.51 μ_B /f.u. Isothermal magnetization collected at 5 K shows a magnetic hysteresis and saturation at 0.71 μ_B /f.u.

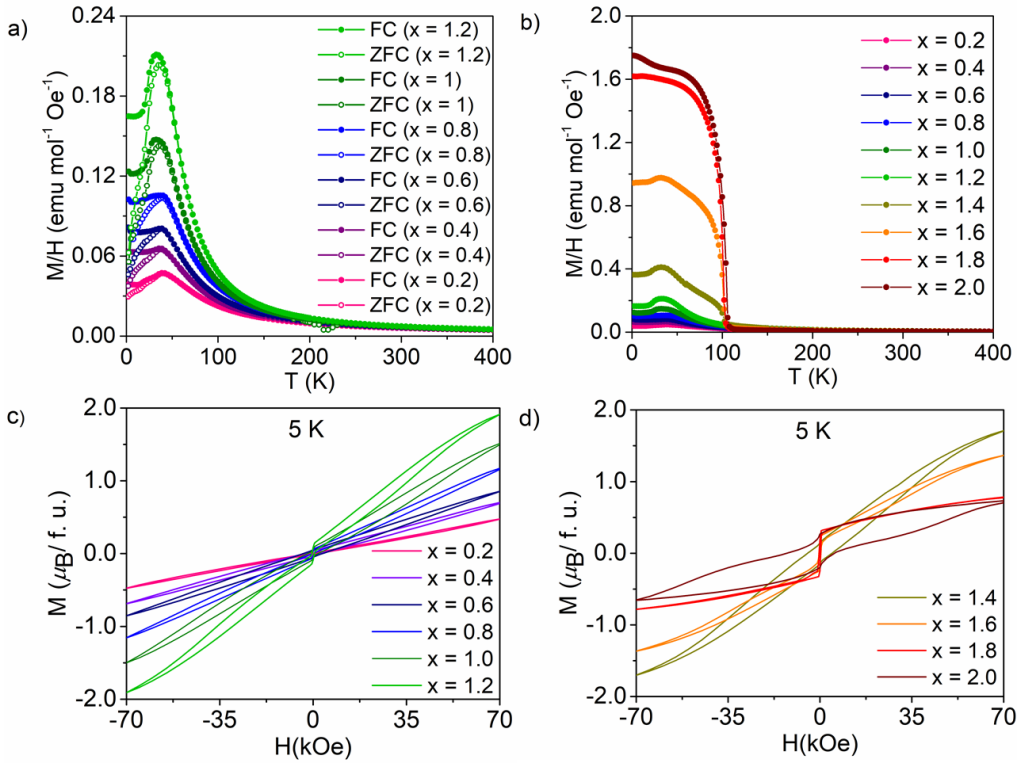

Figure 4.12: a) Temperature dependent magnetic susceptibility for x = 0.2–1.2 with a cusp at 40 K, b) temperature dependent magnetic susceptibility measured with field-cooled condition for x = 0.2–2.0, c) isothermal magnetization at 5 K for x = 0.2–1.2, d) isothermal magnetization at 5 K for x = 1.4–2.0.

4.3.3 Neutron diffraction

Neutron diffraction data for the x = 0.6 sample was taken above the 40 K cusp in the magnetic susceptibility data at 300 K and 60 K and below at 10 K in order to search for signatures of long range magnetic ordering. Comparing the neutron diffraction data at 300 K to the pattern at 60 K showed further distortion of the unit cell as the tetragonal splitting became more prominent. Comparing the neutron diffraction pattern at 60 K and 10 K shows

neither an apparent change in the intensity of any reflection nor the presence of new reflections. This suggests that the *I*4/*m* structure in the $Ba_xSr_{2-x}NiOsO_6$ system does not exhibit long range magnetic order and has a glassy magnetic state.

Variable temperature neutron diffraction taken for the x = 1.2 sample above and below 40 K show weak signature of magnetic ordering. Rietveld refinement of the neutron diffraction patterns at all temperature including ones below the magnetic transition temperature fits well with the $Fm\bar{3}m$ space group. The lack of a feature in the specific heat measurement indicates a glassy magnetic ground state. To confirm this, neutron diffraction patterns taken at 10 K, 25 K, and 60 K were subtracted from the pattern taken at 5 K. No observable difference is observed between the 25 K, 10 K and 5 K patterns, as would be expected since these all fall below the cusp at 40 K seen in the magnetometry data. Subtracting the 60 K pattern from the 5 K pattern, yields two broad features at d spacing of 4.44 Å and 4.27 Å. Since the secondary phase NiO has an antiferromagnetic transition above room temperature, these small magnetic signature are likely to originate from the main perovskite phase. Report on high pressure cubic Ba_2NiOsO_6 show a modulated antiferromagnetic ground state at 32 K with magnetic reflection at 2θ of ~31.5° and 32.8° or d spacing of ~4.44 Å and 4.27 Å, respectively (λ = 2.41 Å). The magnetic reflections in high pressure cubic Ba_2NiOsO_6 are similar to our weak magnetic features in the x = 1.2 sample. However, unlike the high pressure cubic Ba_2NiOsO_6, no observable feature near 40 K that would indicate long range ordering was observed in specific heat of the x = 1.2 sample. The lack of a feature in the specific heat data indicates that there is no entropy change associated with the magnetic transition at 40 K. This suggests that the 40 K transition is a spin glass transition, where the barium and strontium disorder at the *A*-site

destabilizes the complex magnetism observed in high pressure cubic Ba_2NiOsO_6. The modulated antiferromagnetic structure is 8 unit cells along one of the cubic axes. Variation in distribution of barium and strontium can differ from unit cell to unit cell which can destabilize this complex antiferromagnetism. This results in a mostly glassy sample with some volume of sample containing small magnetic domains, which are observable in neutron diffraction on 7 grams of sample as low intensity and broad reflections. However, this is not detectable with specific heat measurement on 10 mg of sample.

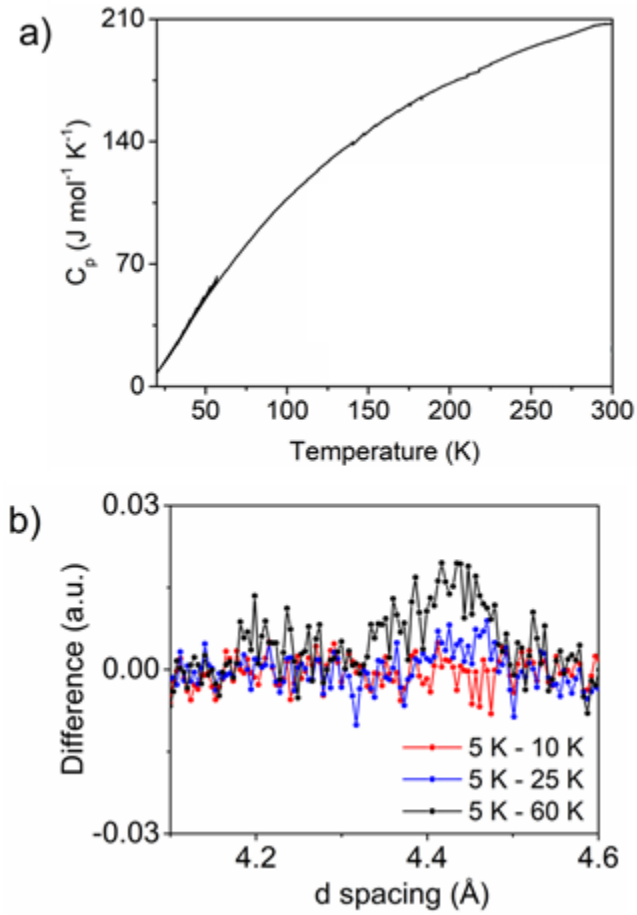

Figure 4.13: a) Specific heat measurement for x = 1.2 sample. No feature is observed around 40 K which indicates the cusp in the magnetic susceptibility data is not a long range ordered state, b) difference between the 5 K pattern and 10 K, 25 K, 50 K, and 60 K for $Ba_{1.2}Sr_{0.8}NiOsO_6$.

Variable temperature neutron diffraction data of Ba_2NiOsO_6 (x = 2.0) show magnetic reflections that appear below 100 K. Neutron patterns from 90 K and below can be fitted to the $P\bar{3}m1$ space group, but there is extra intensity at multiple reflections such as the (2 −1 1) and (1 0 −3) that is not accounted for with Rietveld refinements of the

nuclear structure. Comparing the patterns at 120 K and 90 K show that this increase in intensity appears below the magnetic transition temperature at 100 K, suggesting long range magnetic ordering is present. This is consistent with the observation of ferrimagnetism in the SQUID data.

A Pawley refinement of the neutron diffraction data at 5 K accounts for all reflections and their intensity. This indicates that the magnetic unit cell is identical to the nuclear unit cell. Using ISODISTORT,[57] the magnetic structures consistent with k point of (0 0 0) were generated. Possible magnetic space groups are $P\bar{3}m'1$, $C2/m$, $C2'/m'$, $P\bar{1}$, $P\bar{3}'m'1$, $C2'/m$, $C2/m'$, $P\bar{1}'$ which are variations in orientation of the magnetic moments. Rietveld refinements with comparable goodness of fit and R_{wp} can be obtained for each of these space group. The space groups $C2/m$, $C2'/m'$, $C2'/m$, and $C2/m'$ all contain extra reflections that are not observed in the neutron diffraction pattern, and therefore are not the best model to describe the magnetic unit cell. Placing the constraint that all the Ni moments are equal in magnitude and all the Os moments are equal in magnitude results in either the $P\bar{3}m'1$ or the $P\bar{1}$ space groups as the best model for the magnetic structure. Since there is not a significant improvement in the refinement with the lower symmetry $P\bar{1}$ space group, the higher symmetry $P\bar{3}m'1$ space group was assigned as the magnetic structure of Ba_2NiOsO_6. This structure consists of corner sharing Ni and Os that are ferromagnetically coupled to each other and face sharing Ni and Os that are antiferromagnetically coupled to each other. The refined moment size is 1.94(6) μ_B for Ni^{2+} and 0.64(9) μ_B for Os^{6+} at 60 K. The refined moment size is 2.14(6) μ_B for Ni^{2+} and 0.66(8) μ_B for Os^{6+} at 5 K. Every magnetic unit cell has three formula unit, so the calculated magnetization per unit cell is $|Ni(1) - 2\times(Ni(2)) - Os(1) + 2\times(Os(2))| = 1.3(2)\ \mu_B$ at 60 K and 1.5(2) μ_B at 5 K. Dividing

by the number of formula unit per unit cell results in 0.4(2) μ_B/f.u. and 0.5(2) μ_B/f.u. These moment sizes are consistent with saturated moments of 0.51 μ_B /f.u. and 0.71 μ_B /f.u. from isothermal magnetization versus applied field SQUID measurements at 60 K and 5 K respectively. The refined magnetic structure is consistent with ferrimagnetic ground state.

An important consideration in analyzing the neutron diffraction data is the size of the magnetic moment, which can be too small to detect by neutron diffraction experiment. Spin orbit coupling was previously observed to lower the $5d^2$ Os^{6+} magnetic moment. Experimentally, this moment could be as high as 0.60 μ_B, as reported for Sr_2MgOsO_6 at 10 K, or as low as 0.2–0.3 μ_B at 3–4 K as reported for Ba_2CaOsO_6, Ba_2MgOsO_6, Ba_2ZnOsO_6.[47,58,59] The magnetic moment of the 3d metal Ni^{2+} obtained at 2 K are 1.92(6) μ_B and 2.04(6) μ_B for Sr_2NiMoO_6 and Ba_2NiMoO_6 respectively.[60] The refined magnetic moments of the Os^{6+} and Ni^{2+} from the 5 K neutron diffraction pattern for Ba_2NiOsO_6 are comparable to these values.

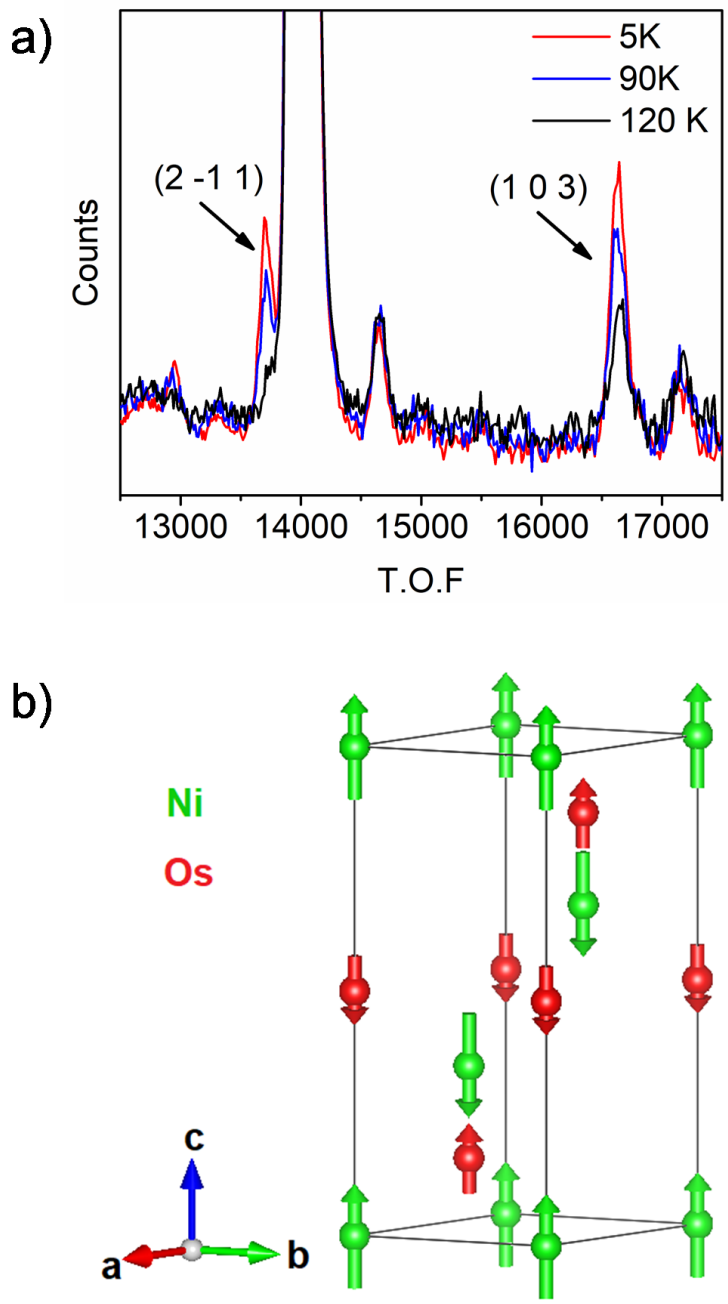

Figure 4.14: a) Magnetic reflections that appeared below 100 K, b) the refined magnetic structure of Ba_2NiOsO_6.

4.4 Discussion

The phase diagram of this series of compounds can be divided into four structural regions: $I4/m$, $Fm\bar{3}m$, mixed phase $Fm\bar{3}m$ and $P\bar{3}m1$, and $P\bar{3}m1$. At low barium concentration, the system adopts the $I4/m$ space group similar to the previously reported Sr_2NiOsO_6 compound.[51] The structure adopts the octahedral tilting scheme $a^0a^0c^-$ where the octahedral tilt is out-of-phase down the c-axis. At intermediate amount of barium substitution, the system becomes cubic $Fm\bar{3}m$. At higher barium substitution, the system becomes a mixture of $Fm\bar{3}m$ and $P\bar{3}m1$ phases due to the fact that the Ba^{2+} is too large to occupy the cubotahedron site in the 3D framework of corner connected octahedra. Instead, with full barium occupation at the A-site, the structure of Ba_2NiOsO_6 is trigonal $P\bar{3}m1$ which is the 6L hexagonal derivative of the perovskite structure with ordering of the cations.

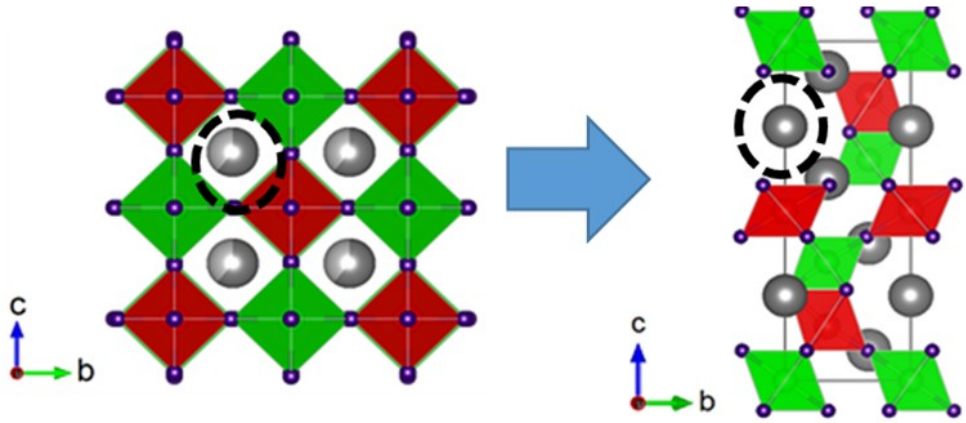

Figure 4.15: At high barium concentration at the A-site, the solid solution $Ba_xSr_{2-x}NiOsO_6$ adopts the trigonal space group (right) to accommodate the large size of the barium.

Goodenough-Kamamori rules for 180° superexchange predicts that Ni^{2+} and Os^{6+} magnetic interaction should be ferromagnetic. Thus, a cubic double perovskite with Ni and Os in the octahedral sites should be ferromagnetic. However, previously reported cubic Ba_2NiOsO_6 has a modulated antiferromagnetic ground state that is 8 unit cells in length along one of the cubic crystallographic axis. The ferromagnetic ground state can only be access with an external applied field of 2.1T. [1] The complex magnetic structure and behavior indicates the competing presence of long range interactions which are likely to be antiferromagnetic. While local Ni–O–Os interactions in this magnetic structure are ferromagnetic, the competition from the long range antiferromagnetic interactions results in a modulated antiferromagnetic structure.

The reported cubic Ba_2NiOsO_6 and our $Ba_{1.2}Sr_{0.8}NiOsO_6$ solid solutions are isostructural but the magnetisms are different. Both the $Ba_{1.2}Sr_{0.8}NiOsO_6$ reported here and the previously reported cubic antiferromagnetic Ba_2NiOsO_6 crystalizes in the $Fm\bar{3}m$ (a = 7.972(1) Å at 5 K and 8.0298(1) Å at 4 K, respectively). The Ni–O distance is 2.0552(3) Å and 2.088(2) Å, and the Os–O distance is 1.9236(3) Å and 1.927(2) Å for $Ba_{1.2}Sr_{0.8}NiOsO_6$ and Ba_2NiOsO_6, respectively. The main difference between these two cubic samples is the mixed *A*-site of the $Ba_{1.2}Sr_{0.8}NiOsO_6$. This indicates that the antiferromagnetic ground state, metamagnetic transitions, and ferromagnetism above 2.1 T of the cubic structure is very sensitive to the local distortion that arise from Sr/Ba disorder. Long range Ni–O–Os–O–Ni and Os–O–Ni–O–Os magnetic interactions competes with short range Ni–O–Os interactions, and the relative strengths of these interactions are sensitive to changes in bond angles. While the overall space group of $Ba_{1.2}Sr_{0.8}NiOsO_6$ is cubic below the magnetic transition temperature, locally there is likely

to be a random mix of linear 180° Ni–O–Os bonds and nonlinear Ni–O–Os bonds due to the Sr/Ba disorder that destabilize the modulated antiferromagnetic ground state leading to spin glass behavior. This further highlights the importance of the variety of short range and long range magnetic interactions in stabilizing the complex magnetic structure in previously reported cubic Ba_2NiOsO_6.

The trigonal Ba_2NiOsO_6 consists of alternating layers of Ni and Os octahedral that are corner connected to face-sharing Ni–Os octahedral dimers. Temperature dependent magnetic susceptibility, isothermal magnetization at 5 K, and magnetic structure solved from neutron diffraction data at 5 K all indicates that trigonal Ba_2NiOsO_6 has a ferrimagnetic ground state. The Ni–O–Os bond angles are 82.58(4) ° for the face-sharing Ni and Os octahedra and 179.85(7) ° and 175.00(7) ° for the corner sharing Ni and Os octahedra. From the magnetic structure solved from neutron diffraction data at 5 K, the coupling of the corner-sharing Ni and Os octahedra is ferromagnetic with Ni–O–Os bond angles close to 180°. The coupling of the face-sharing Ni and Os octahedra is antiferromagnetic with Ni–O–Os bond angles close to 90°. Both of these interactions are consistent with the Goodenough-Kanamori rules for 180° and 90° superexchange interactions. This indicates that in the absence of the complex long range Ni–O–Os–O–Ni and Os–O–Ni–O–Os magnetic interactions observed in the perovskite structures ($I4/m$ and $Fm\bar{3}m$), the Ni and Os magnetic exchange follows the Goodenough-Kanamori rules.

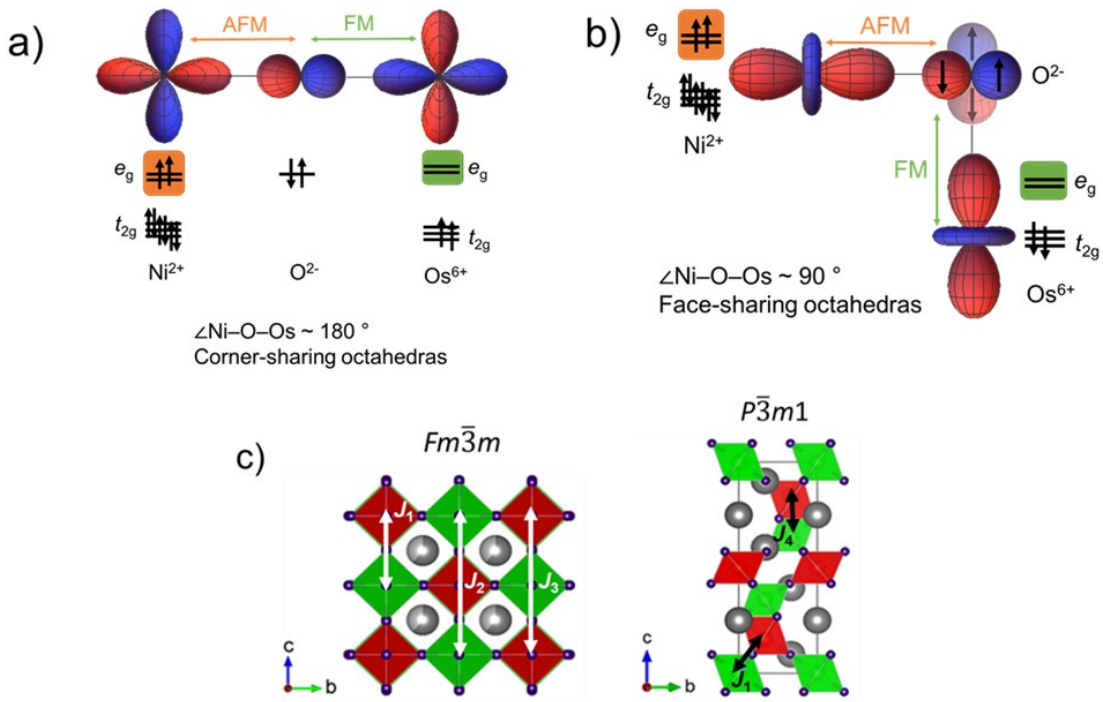

Figure 4.16: a) 90° superexchange results in antiferromagnetic Ni–Os interaction, b) 180° superexchange results in ferromagnetic interaction between the half-filled Ni e_g and empty Os e_g orbitals, c) the perovskite structure houses both short range (J_1) and long range (J_2, J_3) magnetic interactions, while the trigonal structure is dominated by short range (J_1, J_4) magnetic interactions.

4.5 Conclusion

$Ba_xSr_{2-x}NiOsO_6$ was synthesized using the solid state method, and the structure was characterized using laboratory X-ray diffraction. A phase diagram with composition versus temperature was determined from variable temperature X-ray diffraction. The compositions with the $I4/m$ and $Fm\bar{3}m$ structure have a magnetic transition at 40 K with

no signature of long range magnetic order observed in variable temperature neutron diffraction. The trigonal $P\bar{3}m1$ structure has a ferrimagnetic ground state which was determined from magnetometry and neutron diffraction. We found that long range magnetic interaction is important in the double perovskite structures to stabilize the magnetic ground state which results in magnetic behavior that deviates from Goodenough-Kanamori prediction. In the absence of these long range interactions, Ni and Os magnetic exchange follows the Goodenough-Kanamori rules.

References

(1) Feng, H. L.; Calder, S.; Ghimire, P.; Yuan, Y.; Shirako, Y.; Ghimire, M. P.; Yuan, Y.; Shirako, Y.; Tsujimoto, Y.; Matsushita, Y.; Hu, Z.; Kuo, C.; Tjeng, L. H.; Pi, T.; Soo, Y.; He, J.; Tanaka, M.; Katsuya, Y.; Richter, M.; Yamaura, K. *Phys. Rev. B* **2016**, *94*, 235158.

(2) Kayser, P.; Martínez-Lope, M. J.; Alonso, J. A.; Retuerto, M.; Croft, M.; Ignatov, A.; Fernández-Díaz, M. T. *Inorg. Chem.* **2013**, *52* (19), 11013–11022.

(3) Streltsov, S. V.; Khomskii, D. I. *Proc. Natl. Acad. Sci. U. S. A.* **2016**, *113* (38), 10491–10496.

(4) Ou, X.; Li, Z.; Fan, F.; Wang, H.; Wu, H. *Sci. Rep.* **2014**, *4* (c), 2–6.

(5) Samanta, K.; Sanyal, P.; Saha-Dasgupta, T. *Sci. Rep.* **2015**, *5*, 1–8.

(6) Chen, W. T.; Mizumaki, M.; Seki, H.; Senn, M. S.; Saito, T.; Kan, D.; Attfield, J. P.; Shimakawa, Y. *Nat. Commun.* **2014**, *5* (May), 1–7.

(7) Fujioka, J.; Yamada, R.; Kawamura, M.; Sakai, S.; Hirayama, M.; Arita, R.; Okawa, T.; Hashizume, D.; Hoshino, M.; Tokura, Y. *Nat. Commun.* **2019**, *10* (1), 1–6.

(8) Kumar, R.; Sheptyakov, D.; Khuntia, P.; Rolfs, K.; Freeman, P. G.; Rønnow, H. M.; Dey, T.; Baenitz, M.; Mahajan, A. V. *Phys. Rev. B* **2016**, *94*, 174410.

(9) Arai, K.; Takigawa, M.; Yonezawa, S.; Muraoka, Y.; Hiroi, Z. *Phys. B Condens. Matter* **2006**, *378–380* (SPEC. ISS.), 878–879.

(10) Yonezawa, S.; Muraoka, Y.; Matsushita, Y.; Hiroi, Z. *J. Phys. Condens. Matter* **2004**, *16* (3), 8–12.

(11) Vyaselev, O.; Arai, K.; Yamazaki, J.; Takigawa, M.; Hanawa, M.; Hiroi, Z. *Phys. B Condens. Matter* **2003**, *329–333* (II), 959–960.

(12) Ruyan, A. S. B.; Rustum, G. *Mat. Res. Innov.* **2000**, *4*, 3–26.

(13) Goto, T.; Kimura, T.; Lawes, G.; Ramirez, A. P.; Tokura, Y. *Phys. Rev. Lett.* **2004**, *92* (25 I), 1–4.

(14) Zheng, T.; Wu, J.; Xiao, D.; Zhu, J. *Prog. Mater. Sci.* **2018**, *98* (January), 552–624.

(15) Schneemeyer, L. F.; Waszczak, J. V.; Zahorak, S. M.; van Dover, R. B.; Siegrist, T. *Mater. Res. Bull.* **1987**, *22* (11), 1467–1473.

(16) Ishihara, T.; Yamada, T.; Arikawa, H.; Nishiguchi, H.; Takita, Y. *Solid State Ionics* **2000**, *135* (1–4), 631–636.

(17) Goldschmidt, V. M. *Naturwissenschaften* **1926**, *14* (21), 477–485.

(18) Glazer, A. M. *Acta Crystallogr. Sect. B Struct. Crystallogr. Cryst. Chem.* **1972**, *28* (11), 3384–3392.

(19) Stokes, H. T.; Kisi, E. H.; Hatch, D. M.; Howard, C. J. *Acta Crystallogr. Sect. B Struct. Sci.* **2002**, *58* (6), 934–938.

(20) Woodward, P. M. *Acta Crystallogr. Sect. B Struct. Sci.* **1997**, *53* (1), 32–43.

(21) Mitchell, R. H. *Perovskite: Modern and Ancient*; Almaz Press Inc.: Ontario, Canada, 2002.

(22) Fop, S.; McCombie, K. S.; Wildman, E. J.; Skakle, J. M. S.; Mclaughlin, A. C. *Chem. Commun.* **2019**, *55* (15), 2127–2137.

(23) Takeda, Y.; Kanamaru, F.; Shimada, M.; Koizumi, M. *Acta Cryst.* **1976**, *B32*, 2464.

(24) Zhao, J. G.; Yang, L. X.; Yu, Y.; Li, F. Y.; Yu, R. C.; Fang, Z.; Chen, L. C.; Jin, C. Q. *J. Solid State Chem.* **2007**, *180* (10), 2816–2823.

(25) Foo, M. L.; Huang, Q.; Lynn, J. W.; Lee, W. L.; Klimczuk, T.; Hagemann, I. S.; Ong, N. P.; Cava, R. J. *J. Solid State Chem.* **2006**, *179* (2), 563–572.

(26) Kanamori, J. *J. Phys. Chem. Solids* **1959**, *10* (2–3), 87–98.

(27) Goodenough, J. B. *Magnetism and the Chemical Bond*; Interscience Publishers, 1963.

(28) Vogt, T.; Buttrey, D. J. *Complex Oxides:An Introduction*; World Scientific Publishing Company, 2019.

(29) Coelho, A. A. *J. Appl. Crystallogr.* **2018**, *51* (1), 210–218.

(30) Lufaso, M. W.; Woodward, P. M. *Acta Crystallogr. Sect. B Struct. Sci.* **2001**, *57* (6), 725–738.

(31) Retuerto, M.; Martínez-Lope, M. J.; García-Hernández, M.; Fernández-Díaz, M. T.; Alonso, J. A.; Martínez-Lope, M. J.; García-Hernández, M.; Fernández-Díaz, M. T.; Alonso, J. A. *Eur. J. Inorg. Chem.* **2008**, *6* (4), 588–595.

(32) Kato, H.; Okuda, T.; Okimoto, Y.; Tomioka, Y.; Oikawa, K.; Kamiyama, T.; Tokura, Y. *Phys. Rev. B - Condens. Matter Mater. Phys.* **2004**, *69* (18).

(33) Choy, J. *Solid State Ionics* **1998**, *108* (1–4), 159–163.

(34) Feng, H. L.; Guo, Y.; Sathish, C. I.; Wang, X.; Yuan, Y.-H.; Yamaura, K. **2014**, *012002*, 2–5.

(35) Stitzer, K. E.; Smith, M. D.; Loye, H.; Zur Loye, H. C. *Solid State Sci.* **2002**, *4* (3), 311–316.

(36) Bain, G. A.; Berry, J. F. *J. Chem. Educ.* **2009**, *85* (4), 532.

(37) Shannon, R. D. *Acta Cryst.* **1976**, *A32*, 751.

(38) Marjerrison, C. A.; Thompson, C. M.; Sala, G.; Maharaj, D. D.; Kermarrec, E.; Cai, Y.; Hallas, A. M.; Wilson, M. N.; Munsie, T. J. S.; Granroth, G. E.; Flacau, R.; Greedan, J. E.; Gaulin, B. D.; Luke, G. M. *Inorg. Chem.* **2016**, *55* (20), 10701–10713.

(39) Greedan, J. E.; Derakhshan, S.; Ramezanipour, F.; Siewenie, J.; Proffen, T. H. *J. Phys. Condens. Matter* **2011**, *23* (16), 164213.

(40) Wiebe, R.; Greedan, E.; Kyriakou, P.; Luke, M.; Gardner, S.; Fukaya, A.; Gat-Malureanu, M.; Russo, L.; Savici, T.; Uemura, J. *Phys. Rev. B - Condens. Matter Mater. Phys.* **2003**, *68* (13), 1–10.

(41) Lu, L.; Song, M.; Liu, W.; Reyes, A. P.; Kuhns, P.; Lee, H. O.; Fisher, I. R.; Mitrović, V. F. *Nat. Commun.* **2017**, *8*.

(42) Liu, W.; Cong, R.; Reyes, A. P.; Fisher, I. R.; Mitrović, V. F. *Phys. Rev. B* **2018**, *97* (22), 224103.

(43) Svoboda, C.; Randeria, M.; Trivedi, N. **2017**.

(44) Steele, A. J.; Baker, P. J.; Lancaster, T.; Pratt, F. L.; Franke, I.; Ghannadzadeh, S.; Goddard, P. A.; Hayes, W.; Prabhakaran, D.; Blundell, S. J. *Phys. Rev. B - Condens. Matter Mater. Phys.* **2011**, *84* (14), 2–6.

(45) Xiong, J. Investigation of Structural and Magnetic Properties of Perovskite Type Oxides Containing 5d Ions, The Ohio State University, 2017.

(46) Yamamura, K.; Wakeshima, M.; Hinatsu, Y. *J. Solid State Chem.* **2006**, *179*, 605–612.

(47) Thompson, C. M.; Carlo, J. P.; Flacau, R.; Aharen, T.; Leahy, I. A.; Pollichemi, J. R.; Munsie, T. J. S.; Medina, T.; Luke, G. M.; Munevar, J.; Cheung, S.; Goko, T.;

Uemura, Y. J.; Greedan, J. E. *J. Phys. Condens. Matter* **2014**, *26* (30), 306003.

(48) Erickson, A. S.; Misra, S.; Miller, G. J.; Gupta, R. R.; Schlesinger, Z.; Harrison, W. A.; Kim, J. M.; Fisher, I. R. *Phys. Rev. Lett.* **2007**, *99* (1), 1–4.

(49) Goodenough, J. B. *Phys. Rev.* **1955**, *100* (2), 564–573.

(50) Morrow, R.; Samanta, K.; Saha Dasgupta, T.; Xiong, J.; Freeland, J. W.; Haskel, D.; Woodward, P. M. **2016**.

(51) Macquart, R.; Kim, S.-J.; Gemmill, W. R.; Stalick, J. K.; Lee, Y.; Vogt, T.; zur Loye, H.-C.; Loye, H. *Inorg. Chem.* **2005**, *44* (26), 9676–9683.

(52) Coelho, A. A.; Evans, J.; Evans, I.; Kern, A.; Parsons, S. *Powder Diffr.* **2011**, *26* (S1), S22–S25.

(53) Munter, A. Neutron scattering lengths and cross sections, http://webster.ncnr.nist.gov/resources/n-lengths/ http://webster.ncnr.nist.gov/resources/n-lengths/ (accessed Apr 30, 2019).

(54) Feng, H. L.; Adler, P.; Reehuis, M.; Schnelle, W.; Pattison, P.; Hoser, A.; Felser, C.; Jansen, M. *Chem. Mater.* **2016**, *29* (2), acs.chemmater.6b04983.

(55) Liu, H.; Gonzalez, S. *Mat. Res. Soc. Symp. Proc.* **2007**, *48* (1), 329–330.

(56) Mydosh, J. A. *Spin glasses : an experimental introduction*; Taylor & Francis, 1993.

(57) Campbell, B. J.; Stokes, H. T.; Tanner, D. E.; Hatch, D. M.; IUCr. *J. Appl. Crystallogr.* **2006**, *39* (4), 607–614.

(58) Morrow, R.; Taylor, A. E.; Singh, D. J.; Xiong, J.; Rodan, S.; Wolter, A. U. B.; Wurmehl, S.; Büchner, B.; Stone, M. B.; Kolesnikov, A. I.; Aczel, A. A.; Christianson, A. D.; Woodward, P. M. *Sci. Rep.* **2016**, *6* (1), 32462.

(59) Marjerrison, C. A.; Thompson, C. M.; Sharma, A. Z.; Hallas, A. M.; Wilson, M. N.; Munsie, T. J. S. S.; Flacau, R.; Wiebe, C. R.; Gaulin, B. D.; Luke, G. M.; Greedan, J. E. *Phys. Rev. B* **2016**, *94* (13), 134429.

(60) Martínez-Lope, M. J.; Alonso, J. A.; Casais, M. T. *Eur. J. Inorg. Chem.* **2003**, *6* (15), 2839–2844.

Appendix A

Supplementary Information for *Structure and Magnetic Properties of Solid Solution* $Ba_2Na_xCa_{1-x}OsO_6$

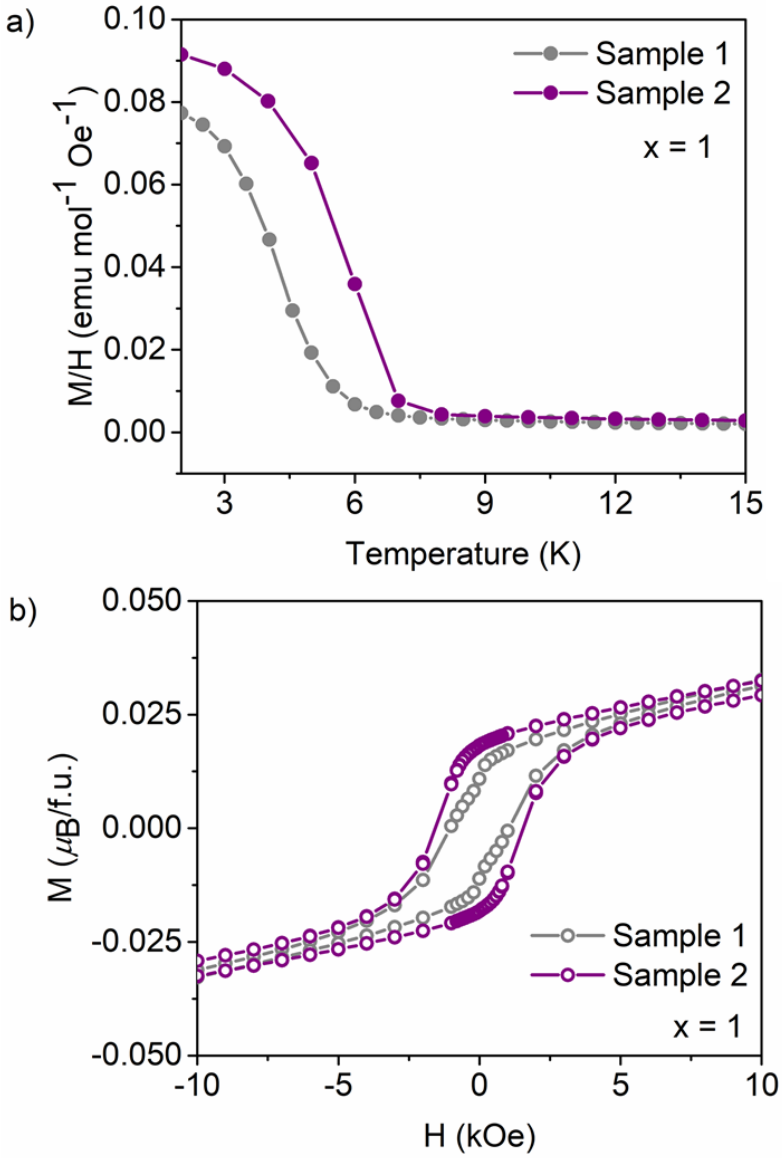

Figure A.1: a) Magnetic susceptibility as a function of temperature for two difference Ba_2NaOsO_6 samples, b) Isothermal magnetization at 2 K for two difference Ba_2NaOsO_6 samples.

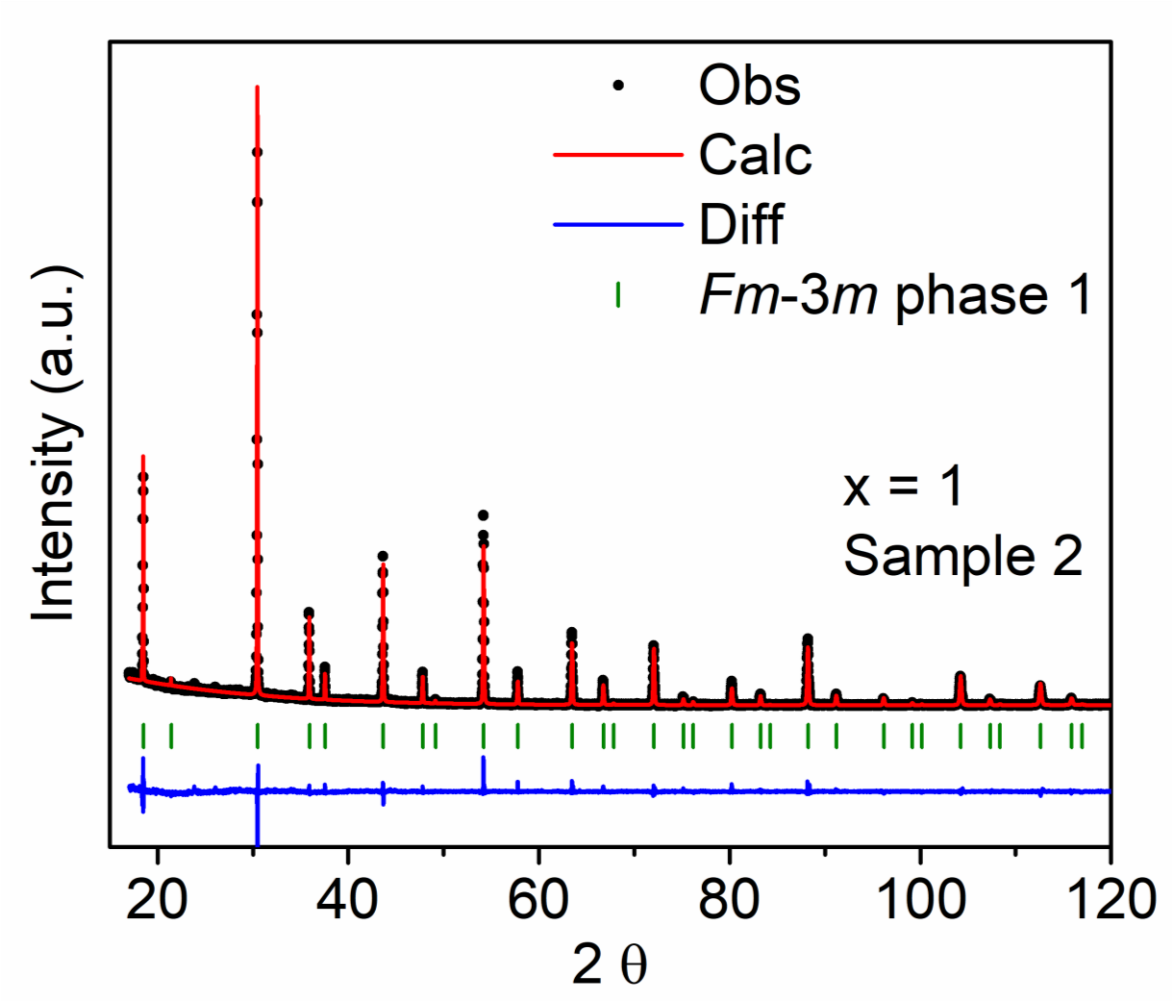

Figure A.2: Room temperature powder X-ray diffraction of the second Ba_2NaOsO_6 sample.